Spring 5-2016

Growth, Characterization and Simulation of Tungsten Selenide Thin Films for Photovoltaic Applications

Qinglei Ma
University of Nebraska-Lincoln, qingleima@gmail.com

Growth, Characterization and Simulation of Tungsten Selenide Thin Films for Photovoltaic Applications

by

Qinglei Ma

A DISSERTATION

Presented to the Faculty of

The Graduate College at the University of Nebraska

In Partial Fulfillment of Requirements

For the Degree of Doctor of Philosophy

Major: Electrical Engineering

Under the Supervision of Professor Natale Ianno

Lincoln, Nebraska

May, 2016

Growth, Characterization and Simulation of

Tungsten Selenide Thin Films for Photovoltaic Applications

Qinglei Ma, Ph.D.

University of Nebraska, 2016

Adviser: Natale J. Ianno

An excellent candidate for an earth abundant absorber material is tungsten selenide (WSe_2) which can be directly grown as a p-type semiconductor with a band gap value that matches well the solar spectrum. Although several fabrication methods were reported, further improvement is highly needed to make high quality WSe_2 films. In addition, the numerical modelling of WSe_2 solar devices is highly desired to assess the overall utility of the material. In this work, the growth and characterization of tungsten selenide thin films are investigated, as well simulations of homo- and hetero-junction devices. In the first part, the growth and characterization of WSe_2 films has been studied. By means of selenization of tungsten films in a closed tube in a single-zone furnace, highly c-axis orientated P-type WSe_2 thin films with a large carrier mobility have been grown. In the second part, multiple sets of simulations of the WSe_2 solar cell devices are carried out by using PC1D software. Both WSe_2 homo-junction devices and hetero-junction devices with an AZO window layer present high efficiency values, over 20%, at several tens of ns carrier lifetime of the absorber layer. This is in large part due to the very high absorption coefficient of WSe_2 thin films.

Acknowledgments

First of all, I would like to thank my advisor, Dr. Natale J. Ianno, for his valuable guidance, encouragement and support throughout my whole Ph.D. research. I have gained so much from him not only about the research itself but also about life in general. It has been an honor and unforgettable experience to me, which I will remember and cherish forever.

I also would like to show my appreciation to my committee members: Dr. Eva Franke-Schubert, Dr. Dennis Alexander, and Dr. Kees Uiterwaal for their critics, advice, and patience in guiding me to finish my dissertation.

I also want to thank my excellent and friendly lab mates that I worked with together in Prof. Ianno's group: Dr. Hrachya Kyureghian, Dr. Amitabha Sarkar, Dr. Jinya Pu, Dr. Fen Zhou, Dr. Zhe Ren, Dr. George Peterson, Chris Feris, David Allendorfer and Matt Hilfiker. I appreciate your help during the work and cherish the times we spent together.

I am particularly thankful to Dr. Yongfeng Lu from Department of Electrical Engineering for his support in the use of the Raman spectroscopy equipment and Hall Effect measurement facility. I am also thankful to Dr. Shah Vallopilly of the Nebraska Center for Materials and Nanoscience (NCMN) for his help on X-Ray diffraction and Dr. You Zhou at the Center for Biotechnology Core Research Facilities (CBCRF) for his instruction on the scanning electron microscopy.

Table of Contents

LIST OF FIGURES ..... **V**

LIST OF TABLES ..... **IX**

CHAPTER 1 INTRODUCTION **1**

1.1. Background 1

1.2. Conventional Energy 1
1.2.1 Global Warming 2
1.2.2 Air Pollution 3

1.3. Renewable Energy 5
1.3.1 Biomass Energy 6
1.3.2 Hydropower Energy 6
1.3.3 Wind Energy 7
1.3.4 Photovoltaic Energy 9

References 12

CHAPTER 2 PHOTOVOLTAIC CELL AND MATERIAL **13**

2.1 History 13

2.2 Photovoltaic Cell 13
2.2.1 Structure 13
2.2.2 Conversion Efficiency 14
2.2.3 Equivalent Circuit 15

2.3 Photovoltaic Material 17
2.3.1 Silicon 18
2.3.2 Polymer 19
2.3.3 Compound Semiconductor 20
2.3.4 Thin Film 21

References 24

CHAPTER 3 SYNTHESIS AND CHARACTERIZATION OF WSE_2 THIN FILMS USING ONE-ZONE FURNACE **35**

3.1 Introduction 35

3.2 Properties 36

3.3 Fabrication 37

3.4 Characterization 40
3.4.1 Raman Spectroscopy 40
3.4.2 XRD 42
3.4.3 Optical Microscopy 46
3.4.4 SEM 47
3.4.5 AFM 49
3.4.6 Ellipsometric Characterization 51
3.4.7 Transmission Optical Spectra 57
3.4.8 Absorption Coefficient 58
3.4.9 Bandgap 60
3.4.10 Hall Effect Test 62

3.5 Discussion 63

3.6 Conclusion 65

References 66

CHAPTER 4 SIMULATION OF WSE_2 SOLAR CELLS WITH PC1D **69**

4.1 Introduction 69

4.2 Analytical Model 69
4.2.1 Voltage and Current 69
4.2.2 Efficiency and Fill Factor 71

4.3 PC1D Software 73
4.3.1 Introduction of PC1D 73
4.3.2 Operating Interface 73
4.3.3 Advantages of PC1D 75

4.4 Simulation of Homo-junction 76
4.4.1 Input Parameter 76
4.4.2 Influence of the n-Layer Thickness 81
4.4.3 Influence of the n-Layer Doping 85
4.4.4 Influence of Minority Carrier Lifetime in the p-Layer 88
4.4.5 Summary 91

4.5 Simulation of Hetero-junction 92
4.5.1 Window Materials 92
4.5.2 Properties of AZO 93
4.5.3 Input Parameters of AZO 93
4.5.4 Simulation results of AZO-WSe_2 94
4.5.5 Summary 98

4.6 Discussion and Conclusion 99

Reference 100

CHAPTER 5 CONCLUSION AND FUTURE WORK **104**

APPENDIX: EXPERIMENTAL TECHNOLOGY **106**

A.1 Sputtering Deposition 106

A.2 Raman Spectroscopy 107

A.3 Spectroscopic Ellipsometry 109

A.4 X-ray Diffraction 110

A.5 Transmission Spectra 111

A.6 Hall Effect Test 113

A.7 Scanning Electron Microscope 115

A.8 Atomic Force Microscopy 116

A.9 Profilometry 118

Reference 119

List of Figures

Figure 1.1 The source, concentration and effect of greenhouse gas in earth temperature, sea level..... 3

Figure 1.2 Air pollution in a developing country..... 5

Figure 1.3 Global growth of wind power capacity 9

Figure 1.4 Growth of photovoltaics power (Megawatts)..... 10

Figure 1.5 Relationships between other renewable energy and solar radiation..... 11

Figure 2.1 A typical p-n junction solar cell (silicon)..... 14

Figure 2.2 Research solar cell efficiencies reported by NREL (2010). 15

Figure 2.3 Equivalent circuit of an ideal solar cell. 16

Figure 2.4 Equivalent circuit of an actual solar cell..... 17

Figure 2.5 Structure of multi-junction compound semiconductor solar cell..... 21

Figure 3.1 Structure of WSe_2 : (a) side view; (b) top view 37

Figure 3.2 XRD of W film (100 nm) 39

Figure 3.3 Sealed quartz tube..... 40

Figure 3.4 Raman Spectra of WSe_2 crystal and WSe_2 thin films fabricated under different temperatures: 825 ^oC, 850 ^oC, 875 ^oC, 900 ^oC..... 41

Figure 3.5 XRD patterns of WSe_2 crystal (a) and WSe_2 thin films under different synthesis temperatures: (b) 825 ^oC, (c) 850 ^oC, (d) 875 ^oC, (e) 900 ^oC..... 44

Figure 3.6 Grain sizes of WSe_2 thin films under different synthesis temperatures 45

Figure 3.7 Magnified images of WSe_2 film surfaces under different temperatures: (a) 825 ^oC, (b) 850 ^oC, (c) 875 ^oC, (d) 900 ^oC..... 47

Figure 3.8 SEM of WSe_2 films fabricated under different temperatures (a) 825 ^oC, planar surface; (b) 825 ^oC, cross section; (c) 850 ^oC, planar surface; (d) 850 ^oC, cross section; (e) 875 ^oC, planar surface; (f) 875 ^oC, cross section; (g) 900 ^oC, planar surface; (h) 900 ^oC, cross section. 49

Figure 3.9 AFM 2D and 3D images of WSe_2 films fabricated under different temperatures: (a) 2D @825 ^oC; (b) 2D @ 850 ^oC; (c) 2D @ 875 ^oC; (d) 2D @ 900 ^oC. (e) 3D @825 ^oC; (f) 3D @850 ^oC; (g) 3D @875 ^oC; (h) 3D @ 900 ^oC. 51

Figure 3.10 Spectroscopic ellipsometric data fitting curves of WSe_2 films under different temperatures: (a) 825 ^oC, (b) 850 ^oC, (c) 875 ^oC, (d) 900 ^oC..... 54

Figure 3.11 Dispersion of refractive index n of WSe_2 crystal and WSe_2 thin films: (a) crystal, 825 ^oC, and 850 ^oC; (b) crystal, 875 ^oC, 900 ^oC..... 55

Figure 3.12 Extinction coefficient k of WSe_2 crystal and WSe_2 thin films: (a) crystal, 825 ^oC, and 850 ^oC; (b) crystal, 875 ^oC, 900 ^oC. 56

Figure 3.13 Transmittance and reflection spectra of WSe_2 films under different temperatures: (a) 825 ^oC, (b) 850 ^oC, (c) 875 ^oC, (d) 900 ^oC..... 58

Figure 3.14 Absorption coefficient calculated from ellipsometry data for WSe_2 crystal and thin films under different temperatures: (a) crystal, 825 ^oC, and 850 ^oC; (b) crystal, 875 ^oC, 900 ^oC..... 59

Figure 3.15 Absorption coefficient calculated from transmission data for WSe_2 crystal

and thin films under different temperatures. 60

Figure 3.16 Tauc plots of a WSe_2 thin film from both transmittance and ellipsometry data. (a) Direct band gap, (b) Indirect band gap. The WSe_2 thin film is made at 875 ^oC..... 61

Figure 3.17 Mobility and carrier concentration (Log(C.C.)) of WSe_2 thin films as a function of selenization temperature. 63

Figure 4.1. Maximum output power of a solar cell 72

Figure 4.2 Operation interface of PC1D 75

Figure 4.3 Efficiency versus n-layer thickness 83

Figure 4.4 Isc and Voc versus n-layer thickness 84

Figure 4.5 Fill factor versus n-layer thickness 85

Figure 4.6 Efficiency versus n-layer doping 86

Figure 4.7 Isc and Voc versus n-layer doping 87

Figure 4.8 FF versus n-layer doping 88

Figure 4.9 Efficiency versus carrier lifetime 89

Figure 4.10 Isc and Voc versus carrier lifetime 90

Figure 4.11 Fill factor versus carrier lifetime 91

Figure 4.12 Equilibrium band structure of AZO-WSe_2 96

Figure 4.13. I-V characteristic of the hetero-junction cell. 97

Figure 4.14 Efficiency versus minority carrier lifetime of p type WSe_2 98

Figure A.1 Sputtering principle 106

Figure A.2 Three types of light scattering: Rayleigh scattering, Stokes scattering and

Anti-Stokes scattering 109

Figure A.3 Characerizations from spectroscopic ellipsometry 110

Figure A.4 The schematic of Bragg scattering 111

Figure A.5 The schematic of light going through a film. 112

Figure A.6 Resistivity measurement configuration (NIST, 2010) 113

Figure A.7 Hall-effect measurement schematic (NIST, 2010) 114

Figure A.8 Schematic of a SEM structure 116

Figure A.9 Block diagram of AFM 117

List of Tables

Table 2.1 Optical band gaps of MX_2 compounds..... 23

Table 3.1 Chemical and physical properties of WSe_2. 37

Table 3.2 Band gaps of WSe_2 obtained from ellipsometry spectra. 62

Table 4.1 WSe_2 parameters for PC1D simulation 78

Table 4.2 AZO parameters for PC1D simulation 94

Chapter 1 Introduction

1.1. Background

The global demand for energy has been growing rapidly and is causing an energy crisis for human beings which is one of the most crucial issues in the world. Currently, there are two main energy sources on the earth: one is called conventional energy, such as petroleum, coal, and natural gas while the other is called renewable energy which directly or indirectly comes from solar radiation, such as solar energy, biomass energy, wind energy and hydropower energy.

1.2. Conventional Energy

Conventional energy sources (petroleum, coal, and natural gas) have played an important role in the industrial revolution of human beings and still drive economic progress in modern society. The principle of conventional energy sources is that when fossil fuels burn, the component of the fuels which mainly contains carbon and hydrogen atoms will chemically react with the oxygen in the air at high temperature. The reaction is an exothermic process and releases a large amount of heat which may be used to produce electricity and power. Negative effects, such as global warming and air pollution, are a result of this process.

1.2.1 Global Warming

Carbon oxide and hydrogen oxide molecules are the primary two byproducts of fossil fuel combustion. Hydrogen oxide will become water, however carbon oxide which is a greenhouse gas prevents part of the IR radiation from escaping the earth's atmosphere. In the United States, it is reported that more than 90% of greenhouse gas (carbon oxide) emissions come from the combustion of fossil fuels [1]. Greenhouse gas is accumulating around the earth's surface, causing global warming. Fig.1.1 shows the effect of greenhouse gas on the earth's temperature, sea level, and carbon oxide concentration in recent decades [2]. Future predictions from scientists indicate that if action is not taken the earth's surface temperature may rise by between 1.4 ^{o}C and 5.8 ^{o}C, which will probably cause serious droughts, flood, rising sea levels, glacier melting, and serious disruptions to agriculture and natural ecosystems [3].

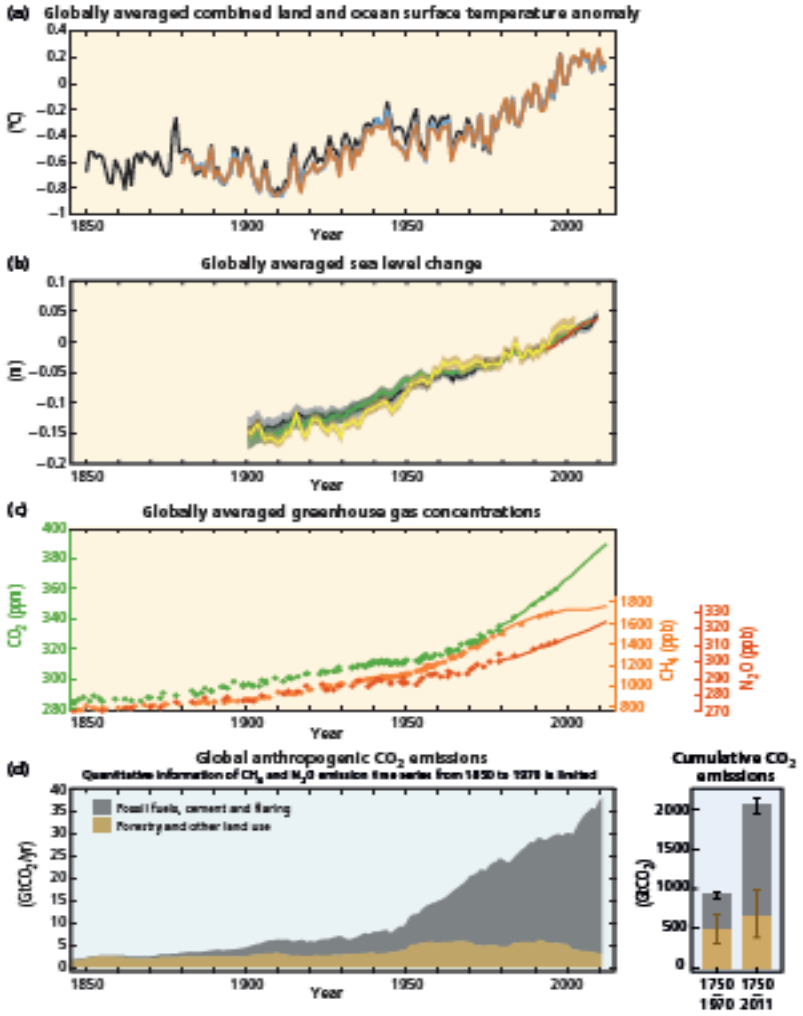

Figure 1.1 The source, concentration and effect of greenhouse gas in earth temperature, sea level.

1.2.2 Air Pollution

Additionally, impurities in the fossil fuel can pollute the earth's atmosphere. For example materials such as nitrogen oxides, sulfur dioxide, volatile organic compounds, heavy metals, and particulate matter can enter the atmosphere as a result of fossil fuel combustion. Some of them, such as nitrogen oxides and sulfur dioxides result in acid rain,

which can erode both natural areas and the man-made environment. Some of them such as particulate matter also known as ‘PM’ will permeate the air, saturate the air with fog, and become poisonous dust/smoke that threatens the health of human beings. Currently some cities in the developing countries are suffering from PM, such as PM 2.5, which is a particulate matter with diameter of 2.5 micrometers or less. According to the U.S. Environmental Protection Agency, such fine particles can cause asthma, bronchitis, and acute and chronic respiratory symptoms such as shortness of breath and painful breathing, and may also lead to premature death [4]. Fig. 1.2 shows the air pollution in a developing country due to the excessive combustion of fossil fuel. Furthermore, recent research also found that fossil fuels contain radioactive materials, mainly uranium and thorium, which are released into the atmosphere and it is reported that in 2000, about 12,000 tons of thorium and 5,000 tons of uranium were released worldwide from burning coal [5].

Figure 1.2 Air pollution in a developing country.

Currently conventional energy sources dominate energy production and supply about 90% of the energy demand in the world. However, fossil fuels cannot last forever, and after a few decades all these current sources on the earth may be exhausted. Based on all of these factors, people are seeking other energy sources, particularly renewable energy sources.

1.3. Renewable Energy

Renewable energy is defined as energy that comes from resources which are naturally replenished on a human timescale such as sunlight, wind, rain, tides, waves, and geothermal heat [6]. Renewable energy, which is clean, safe and infinite, would generate

significant economic benefits and also reduce current air pollution caused by combustion of fossil fuels and eventually improve public health, reduce premature mortalities and save associated health costs. Recently, the use of renewable energy sources such as photovoltaic energy, biomass energy, hydropower energy and wind energy is becoming more widespread.

1.3.1 Biomass Energy

Biomass is biological organic material that is the product, waste, and residue from agriculture, forestry, and related industries. Currently, wood remains the largest and most widespread biomass energy source in the world. Biomass energy refers to the renewable energy that is generated from a variety of biomass. Biomass can be directly burned and generate heat and electricity. Besides, biomass can also be converted into other usable forms of energy, such as biofuel, which is achieved by employing different methods which are broadly classified into: thermal, chemical, and biochemical methods. Rotting garbage, and agricultural and human waste can generate ‘biogas’ which is actually methane. This means that biomass can also be converted into methane gas or transportation fuels like ethanol and biodiesel.

1.3.2 Hydropower Energy

Hydropower harnesses the energy of falling water or running water for electricity generation. Early in the late 19th century, hydropower became a source for generating

electricity. Cragside in Northumberland was the first house powered by hydroelectricity in 1878 and the first commercial hydroelectric power plant was built at Niagara Falls in 1879 [7]. Currently hydroelectric power is recognized as a means for economic development without adding substantial amounts of carbon to the atmosphere and hydroelectric power systems are currently found in most places in the world [8]. Depending on the hydrology and topography of the watershed, hydropower plants vary from small to large in terms of scale. There are four main hydropower categories: run of stream, reservoir, dam, and pumped storage. The water flow in a stream can change greatly from season to season, and even year to year, which requires years' analysis of flow records to determine the possible annual power supply of the hydropower systems. Reservoirs and dams, compared with the stream, can provide a more dependable source of power by smoothing seasonal changes in water flow. However dams can impact the surrounding environment and cause significant social or environmental issues. Pumped-storage systems transfer water from the bottom of a reservoir to the upper reservoir during off-peak hours to be used later and during periods of high electrical demand. The stored water is released through turbines to produce electric power. Currently, pumped-storage systems are a practical approach to enhance the hydropower and accounts for 99% of on-grid electricity storage.

1.3.3 Wind Energy

Wind energy is renewable, clean and practically unlimited. Generally the wind

drives the turbines to rotate and generate electricity. Usually, a large amount of turbines are employed in wind farms. Wind turbines can be constructed where there is enough wind, such as in a valley, on a plain, or offshore. Wind sources in most places varies significantly from season to season. Offshore sites provide relatively stable and high wind sources throughout the whole year. However, the cost is very high. In most cases, wind power plants are usually integrated with other electric power sources in order to provide a reliable supply.

In recent years, wind power has grown quickly, as shown in Fig 1.3, and has reached around 4% of the electricity usage in the world by 2014 [9]. More than 83 countries in the world are using wind power in their electric grids and some countries in Europe have reported that the production of the wind power had achieved around 40% of the overall electricity [10].

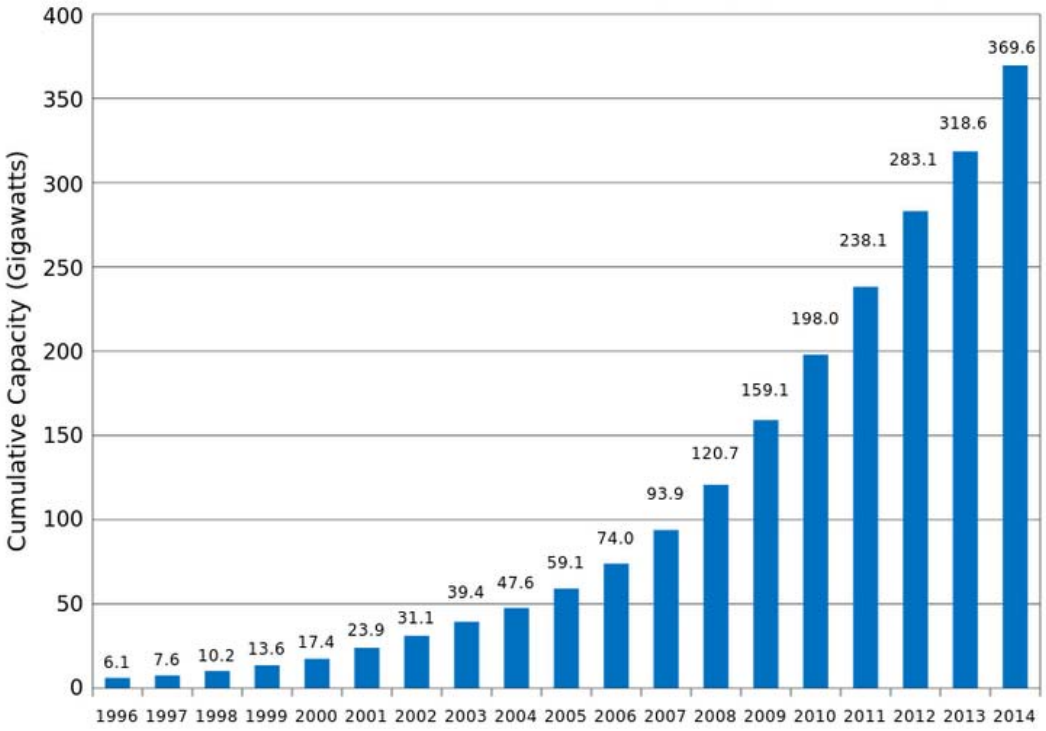

Figure 1.3 Global growth of wind power capacity.

1.3.4 Photovoltaic Energy

When light (usually sunlight) is incident on a semiconductor p-n junction, electrons in the valence band of the semiconductor material will absorb the photons which have higher energy than the bandgap, become excited, and jump to the conduction band. As a result, a large amount of free electron-hole pairs are generated. As a result of the built-in voltage or electric field in the p-n junction, electron-hole pairs are accelerated moving in the opposite directions yielding a net current. Thus some of the light energy is converted into electric energy. In recent years the growth of photovoltaics has been exponentially increasing throughout the world, as shown in Fig 1.4 [11]. By 2014,

cumulative photovoltaic capacity has reached about 200 gigawatts (GW), which accounts for 1 percent of supply of total electricity consumption in the world.

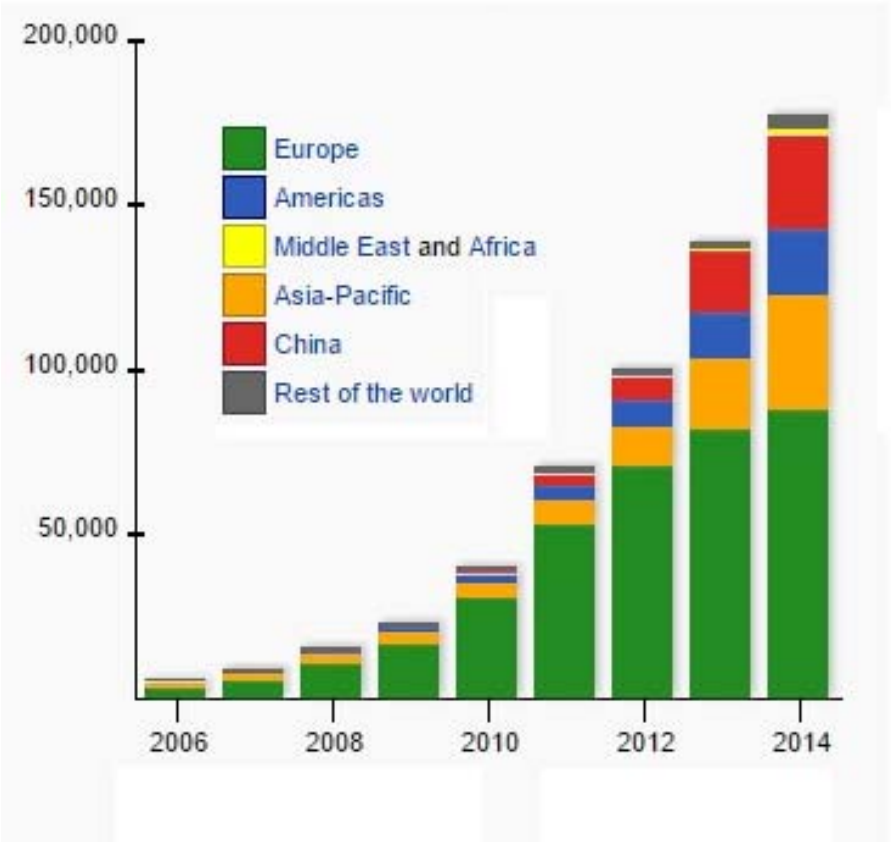

Figure 1.4 Growth of photovoltaics power (Megawatts).

Sunlight is the most abundant energy source available on the earth. Most of the renewable energy sources derive their energy from solar radiation, either directly or indirectly, employing various process and technologies. Figure 1.5 shows how the various forms of renewable energy are connected with solar radiation [12]. Among these renewable energy types, photovoltaic (PV) systems can directly convert solar energy into

electricity and is believed to be the simplest technology to design and install.

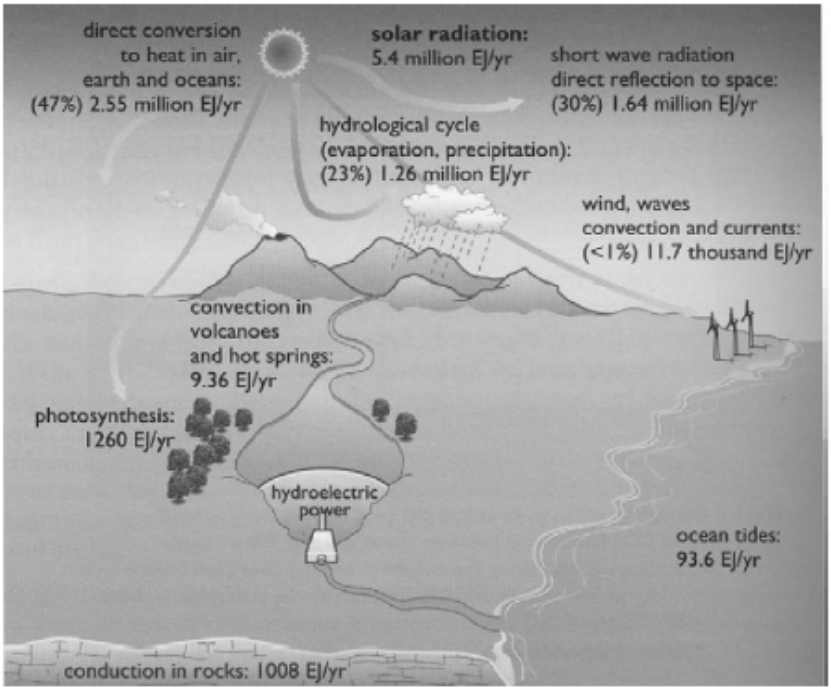

Figure 1.5 Relationships between other renewable energy and solar radiation.

References

[1] Inventory of U.S. Greenhouse Gas Emissions and Sinks: 1990–1998, Rep. EPA 236-R-00-01. US EPA, Washington, DC.

[2] Climate Change 2014 Synthesis Report Summary for Policymakers.

[3] L. EI Chaar, L.A. Lamont, N. El Zein, Review of photovoltaic technologies, Renewable and Sustainable Energy Reviews, 2011 (15) 2165–2175.

[4] 'PM2.5'.United States Environmental Protection Agency. Retrieved Oct.7th 2014.

[5] Alex Gabbard, Coal Combustion: Nuclear Resource or Danger.

[6] Ottmar Edenhofer, Ramon Pichs-Madruga, Youba Sokona, Special report on renewable energy sources and climate change mitigation, 2012, pp 1-10.

[7] "Cragside Visitor Information". The National Trust. Retrieved 16 July 2015.

[8] Howard Schneider. 'World Bank turns to hydropower to square development with climate change', The Washington Post. Retrieved 9 May 2013.

[9] The World Wind Energy Association. 2014 Half-year Report. pp 1–8.

[10] REN21 (2011). "Renewables 2011: Global Status Report". pp 1-11.

[11] "Global Market Outlook for Solar Power 2015-2019". http://www.solarpowereurope.org/

[12] Boyle Godfrey. Renewable energy power for a sustainable future. 2nd Edition Oxford University Press, 2004.

Chapter 2 Photovoltaic Cell and Material

2.1 History

The photovoltaic device has been experiencing steady theoretical and technological progress since French physicist Alexandre-Edmund Becquerel discovered that ‘electrical currents arose from certain light induced chemical reactions’ in the year of 1839 [1]. The first photovoltaic devices (solar cell) were created with crystalline silicon at Bell Laboratory in 1953, achieving an efficiency of 4.5%. Later in 1954, the scientists at Bell Laboratory improved the solar cells to 6% efficiency [2]. With the improvement of the conversion efficiency, solar cells could be used as electrical power sources for spacecraft, special terrestrial applications such as lighthouses, and consumer products such as electronic calculators.

2.2 Photovoltaic Cell

2.2.1 Structure

A solar cell usually consists of semiconductor materials in the form of a p-n junction. When light shines on the p-n junction, it will absorb the light and generate excess electron hole pairs. Due to the electric field in the depletion region, the excess holes in the n-region move towards the p-region and the excess electrons in the p-region move towards n-region, which produce both a current and a voltage. Figure 2.1 shows a

typical p-n junction solar cell. The operation of a solar cell entails the following four basic steps:

a) light-generation of carriers;

b) the collection of the light-generated carriers yielding a current;

c) the generation of a voltage across the solar cell;

d) the dissipation of power in the load and in parasitic resistances.

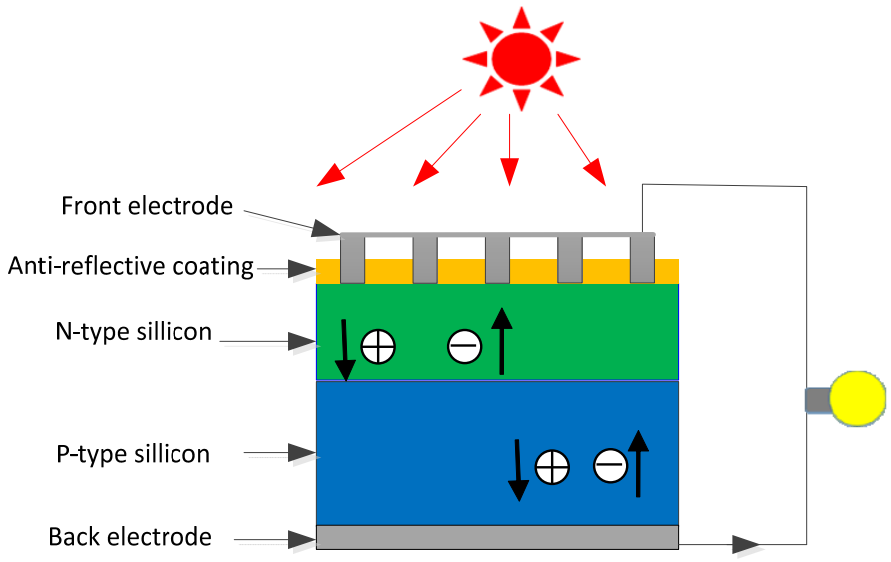

Figure 2.1 A typical p-n junction solar cell (silicon).

2.2.2 Conversion Efficiency

Besides silicon solar cells, various types of solar cells are currently studied, such as polymer organic cells, thin films cells, and compound semiconductor cells. Many of them are already industrially available. The efficiencies of various kinds of solar cells have significantly improved over the past 30 years, as is shown in Figure 2.2. Although

silicon solar cells do not have the highest efficiency among various types of solar cells, they are still dominant in the solar sell market because they currently provide a good compromise between efficiency and cost.

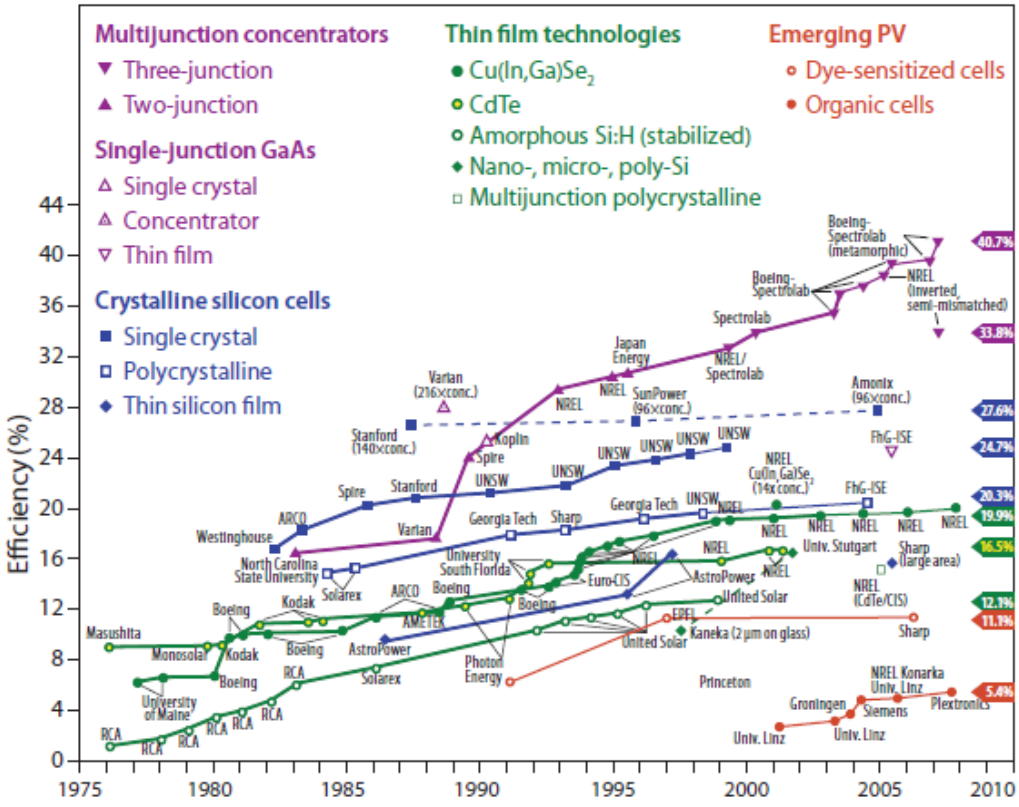

Figure 2.2 Research solar cell efficiencies reported by NREL (2010).

2.2.3 Equivalent Circuit

The solar cell can be ideally seen as a parallel connection of a current generator and a diode, as is shown in Figure 2.3. The current generator is producing a current I_L. The dark current I_D, which is caused by a potential applied to the diode, flows in the

opposite direction of the I_L. Hence the current through load R_L is ideally:

$$I = I_L - I_D \tag{2.1}$$

and the voltage applied on the load R_L is

$$V = (I_L - I_D)R_L \tag{2.2}$$

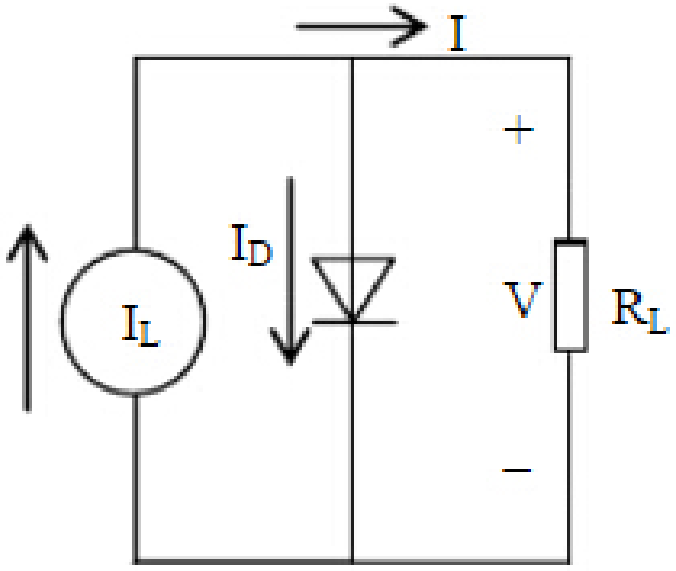

Figure 2.3 Equivalent circuit of an ideal solar cell.

In the actual case, the solar cell material is not a perfect conductor and there exists a resistance R_s. In addition, due to poor insulation or packaging in the fabrication process, leakage of current may occur from one terminal to the other, such as at the edges of the cell. Therefore, two more resistances called parasitic resistances should be inserted: one in series (R_s) and one in parallel (R_p), as is shown in Figure 2.4. In an ideal solar cell, $R_s = 0$ and $R_p = \infty$. When these so called parasitic resistances are included, the current

expression becomes:

$$I = \frac{R_P}{R_L + R_P}(I_L - I_D) \tag{2.3}$$

And the voltage on the load R_L is:

$$V = \frac{R_L R_P}{R_L + R_P}(I_L - I_D) \tag{2.4}$$

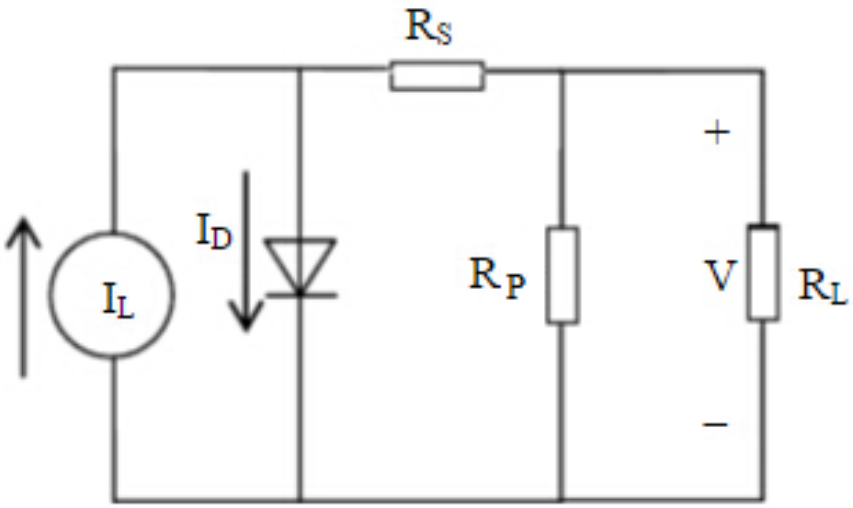

Figure 2.4 Equivalent circuit of an actual solar cell.

2.3 Photovoltaic Material

All solar cells require a light absorbing material to absorb photons and generate free electrons via the photovoltaic effect. The properties of photovoltaic material directly determine the performance of solar cell devices.

2.3.1 Silicon

The first solar cells were fabricated from silicon. Silicon is still the main material for photovoltaic devices. Silicon technology has been recognized as the dominant one for the supply of power modules into photovoltaic applications [3-11]. Monocrystalline silicon and polycrystalline silicon are expected to occupy an increasing proportion of photovoltaic devices with the development of silicon technology [12].

Monocrystalline silicon is the most widely used solar cell material, offering a high efficiency of 14-19% for commercial photovoltaic devices [13-19]. Due to the intrinsic properties of silicon material, currently attempts to enhance the efficiency are limited by the amount of photon energy since it decreases at longer wavelengths. Solar cell module efficiencies usually tend to be lower than the single solar cell device. Recently an efficiency of 20.4% for a full module panel was reported by National Renewable Energy Laboratory (NREL). Monocrystalline silicon solar cells own 80% of the market and will continue to be the leader until a more efficient and cost effective PV technology is developed.

Polycrystalline silicon is another very popular material with cell efficiencies of 10-15%, which is mainly due to much larger concentrations of defects and impurities in silicon crystal, partially offsetting the benefits of the lower cost material [20-28]. Although its efficiency is slightly less than that of monocrystalline, polycrystalline silicon is becoming attractive because its manufacturing cost is much lower and the efficiencies of polycrystalline cell modules are almost the same as those for monocrystalline cells

(14%) due to the higher packing factor of the square polycrystalline cells [29].

2.3.2 Polymer

Organic solar cells are fabricated with organic semiconductor thin films, such as polymers, pentacene, polyphenylene vinylene, and carbon fullerenes. Although the present dominant photovoltaic devices are based on inorganic materials, organic photovoltaic cells have attracted considerable attention in recent years. Currently reported conversion efficiency of polymer cells are less than 10% [30-47]. However, the polymer has several advantages over the traditional photovoltaic materials, such as a low-cost manufacturing process, mechanical flexibility, and disposability [48-51].

In 1979 Tang et al. introduced an organic PV cell based on the donor-acceptor bilayer planar heterojunction with a power-conversion efficiencies of around 1% [52][53]. Yang Y. et al. explained that the highest-efficiency polymer solar cells are those based on polymer-fullerene systems, and conversion efficiencies can reach 10%. Jorgensen et al. presented an understanding of stability/degradation in organic and polymer solar cell devices and discussed the methods for studying and elucidating degradation and enhancing the stability through the choice of better active materials, encapsulation, application of getter materials and UV filters [54]. Mozer et al. presented successful strategies towards improved photovoltaic performance using various novel materials, including double-cable polymers, regioregular polymers, and low bandgap polymers, demonstrating that the bulk heterojunction concept is a viable approach towards

developing photovoltaic systems by inexpensive solution-based fabrication technologies [55]. Due to its natural advantages, organic photovoltaic technology is recognized as one of the most promising PV technologies with lower cost and potentially high conversion efficiency.

2.3.3 Compound Semiconductor

Compound semiconductor solar cells are generally made of III-V semiconductor materials (e.g., GaAs, InP, GaN, AlAs, AlP, and InAs), specifically with multi-junction tandem, photonic up/down conversion, and plasmonic metallic structures. Although the material processing cost of conventional III-V semiconductor is relatively high, the superior performance (high energy conversion) makes it attractive among all different types of solar cell materials [56-75]. Energy conversion efficiencies of ~40%, which is the highest value of any photovoltaic technology to date, have been achieved in laboratories using III-V compound semiconductor material in the form of sophisticated epitaxial multi-junction device structures.

One of the major factors resulting in energy loss in a solar cell is the gap between the photon energy and the bandgap energy of the photovoltaic material. If the photon energy was smaller than the bandgap energy, no absorption would occur. The photovoltaic material can only absorb the photons whose energy is larger than the bandgap energy, leaving the other part of the sunlight wasted as heat. The multi-junction solar cell can solve this problem. Each type of semiconductor materials has a different

band gap energy which allows it to absorb certain range of the spectrum efficiently. A typical structure of a compound multi-junction semiconductor solar cell is shown in Figure 2.5 [76]. The multi-junction solar cell device consists of a germanium (0.7 eV) bottom junction and middle and top junctions of GaAs (1.4 eV) and GaInP (1.9 eV). As a result, solar cell devices made of multi-junctions of different bandgaps are tuned to utilize the whole sunlight spectrum from 300 nm to 1880 nm. Furthermore, compound semiconductor solar cells have higher resistance to high-energy rays in space, and higher tolerance of increased operating temperatures, which make them promising in space PV cells with applications in telecommunication satellites, military satellites, and scientific space probes.

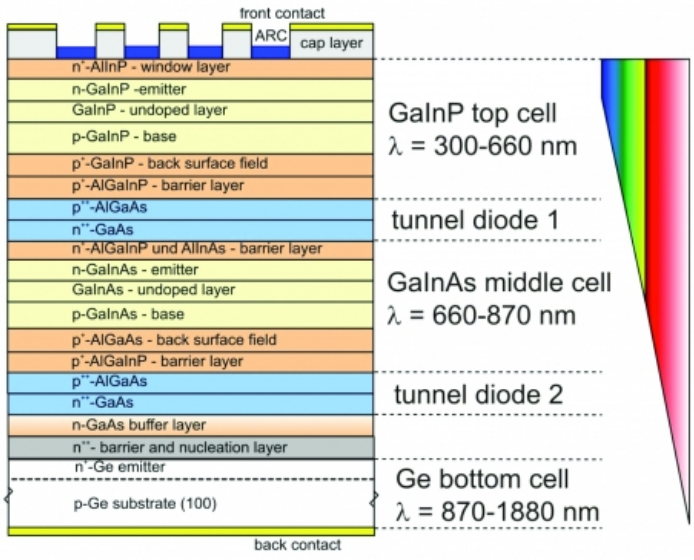

Figure 2.5 Structure of multi-junction compound semiconductor solar cell.

2.3.4 Thin Film

A thin film solar cell is made by depositing one or more thin photovoltaic material

layers on a substrate, such as glass, plastic or metal. The advantage of thin film technology is that the thickness of the deposited layers is barely a few microns (smaller than 10 μm) thick which is much smaller than the crystalline wafers which tend to be several hundred microns thick [77-81]. The resulting advantage for thin film solar cells is lower manufacturing cost due to the high throughput deposition process as well as less cost of materials. In comparison with crystalline silicon cells, thin film technology holds the promise of reducing the cost of PV array by lowering material and manufacturing without jeopardizing the cells' lifetime as well as any hazard to the environment.

Chalcogenides, such as cadmium telluride, cadmium sulphide, and cadmium selenide, are very important thin film solar cell materials [82-86]. Among the chalcogenide based solar cells, Cadmium telluride (CdTe) is recognized as a promising photovoltaic material due to its band-gap (1.5 eV) is close to the ideal value for photovoltaic conversion efficiency, as well as a high direct absorption coefficient. The energy conversion efficiency is larger than 15% for solar cells and 9% for modules. Cadmium telluride is currently predominant in thin film solar cell technology, and is very successful in commercial applications, which accounts for more than half of the thin film PV market. However, the disadvantage of CdTe modules results from the toxicity of cadmium, and a limited tellurium supply. Cadmium based modules are banned in some countries such as Netherlands.

Transition metal chalcogenide (TMC) semiconducting materials MX_2 (M=W Mo; X= S, Se) display potential for use as solar cells, because their optical bandgaps are well

matched to the solar spectrum, as is shown in table 2.1 [87]. Furthermore, due to their unique physical and electronic structure, the mono-layered di-chalcogenides, as two-dimensional materials, display a variety of interesting properties and phases, including highly anisotropic mechanical, optical, and electrical properties. In 2014, a large scale MoS_2 monolayer heterojunction photovoltaic device was reported to achieve a power conversion efficiency of 5.23%, which is the highest efficiency among all monolayer transition-metal di-chalcogenide-based solar cells [88].

Table 2.1 Optical band gaps of MX_2 compounds.

Material	Indirect Bandgap (eV)	Direct Bandgap (eV)
MoS_2	1.14 - 1.50	1.7 - 2.0
$MoSe_2$	1.05 - 1.12	1.35 - 1.40
WS_2	1.29 - 1.35	1.7 - 1.9
WSe_2	1.16 - 1.22	1.35 - 1.50

Among all chalcogenide (TMC) semiconducting materials, WSe_2 is promising because its bandgap is closest to the ideal bandgap value for solar cells. This research is mainly focused on the fabrication of WSe_2 thin films, as well as various physical, optical and metrology characterizations. In the end, the simulation of WSe_2 solar cell is carrier out with PC1D software.

References

[1] Becquerel A. E., Mémoire sur les effets électriques produits sous l'influence des rayons solaires. Comptes Rendus, 1839 (9) 561-567.

[2] Chapin D. M., Fuller C. S., Pearson G. L., A new silicon p-n junction photocell for converting solar radiation into electrical power, J. Appl. Phys. 1954 (25) 676.

[3] Braga A. F. B., Moreira S. P., Zampieri P. R., Bacchin J. M. G., Mei P. R. New processes for the production of solar-grade polycrystalline silicon: A review. Solar Energy Materials & Solar Cells, 2008 (92) 418–24.

[4] Goetzberger A., Hebling C. Photovoltaic materials, past, present, future. Solar Energy Materials & Solar Cells, 2000 (62) 1–19.

[5] Keogh W. M., Blakers A. W. Accurate measurement using natural sunlight, of silicon solar cells. Progress in Photovoltaics: Research and Applications, 2004 (12) 1–19.

[6] Hanoka J. I. An overview of silicon ribbon growth technology. Solar Energy Materials & Solar Cells 2001 (65) 231–237.

[7] Schlemm H., Mai A., Roth S., Roth D., Baumgartner K. M., Mueggeb H. Industrial large scale silicon nitride deposition on photovoltaic cells with linear microwave plasma sources. Surface and Coatings Technology, 2003 (174) 208–211.

[8] Zwaan B., Rabl A. Prospects for PV: a learning curve analysis. Solar Energy, 2003 (74) 19–31.

[9] Aouida S., Saadoun M., Boujmil M. F., Ben Rabha M., Bessais B. Effect of UV irradiations on the structural and optical features of porous silicon: application in

silicon solar cells. Applied Surface Science, 2004 (238) 193–198.

[10] Mccann M., Weber K., Blakers A. Surface passivation by rehydrogenation of silicon-nitride-coated silicon wafers. Progress in Photovoltaics: Research and Applications, 2005 (13) 195–200.

[11] Adamian Z. N., Hakhoyan A. P, Aroutiounian V. M, Barseghian R. S, Touryan K. Investigations of solar cells with porous silicon as antireflection layer. Solar Energy Materials & Solar Cells, 2000 (64) 347–351.

[12] Bruton T. M. General trends about photovoltaics based on crystalline silicon, Solar Energy Materials & Solar Cells, 2002 (72) 3–10.

[13] Aberle A. G. Overview on SiN surface passivation of crystalline silicon solar cells. Solar Energy Materials & Solar Cells, 2001 (65) 239–248.

[14] Vitanov P., Delibasheva M., Goranova E., Peneva M. The influence of porous silicon coating on silicon solar cells with different emitter thicknesses. Solar Energy Materials & Solar Cells, 2000 (61) 213–221.

[15] Schmich E., Kiefer F, Hörteis M., Alemán M., Glunz S., Reber S., Emitter epitaxy for crystalline silicon thin film solar cells with new contact methods, 24th European Photovoltaic Solar Energy Conference, Hamburg, Germany, 2009, 2570-2574.

[16] Fellmeth T., Fritz S., Menkoe M., Mingirulli N., Glatthaar M., Clement F., Biro D., Preu R., Development of crystalline silicon based metal wrap through (MWT) solar cells for low concentrator (2-30x) applications, 24th European Photovoltaic Solar Energy Conference, Hamburg, Germany, 2009, 711-716.

[17] Macdonald D., McLean K., Deenapanray P. N. K., De Wolf S., Schmidt J. Electronically-coupled up-conversion: an alternative approach to impurity photovoltaics in crystalline silicon. Semiconductor Science and Technology, 2008 (23) 015001.

[18] Green M. A., Basore P. A., Chang N., Clugston D., Egan R., Evans R., Hogg D., Jarnason S., Keevers M., Lasswell P., Sullivan J. O., Schubert U., Turner A., Wenham S. R., Young T. Crystalline silicon on glass (CSG) thin-film solar cell modules. Solar Energy, 2004 (77) 857–863.

[19] Riegel S., Raabe B., Petres R., Dixit S., Zhou L., Hahn G., Towards higher efficiencies for crystalline silicon solar cells using SiC layers, 23rd European Photovoltaic Solar Energy Conference and Exhibition, Valencia, Spain, 2008, 1604-1607.

[20] Lindmayer J., Semi-crystalline silicon solar cell, Proc. 12th IEEE Photovoltaic Specialists Conference, 1976, 82-85.

[21] Fischer H., Pschunder W., Low cost solar cells based on large area unconventional silicon, Proc. 12th IEEE Photovoltaic Specialists Conference, 1976, 86-92.

[22] Lipinski M., Panek P., Swiatek Z., Beltowska E., Ciach R. Double porous silicon layer on multi-crystalline Si for photovoltaic application. Solar Energy Materials & Solar Cells, 2002 (72) 271–276.

[23] Dobrzanski L. A, Drygała A. Laser processing of multicrystalline silicon for texturization of solar cells. Journal of Materials Processing Technology, 2007 (191)

228–231.

[24] Schubert M. C., Gundel P., The M., Warta W., Romero M. J., Ostapenko S., Arguirov T., Spatially resolved luminescence spectroscopy on multicrystalline Silicon, 23rd European Photovoltaic Solar Energy Conference and Exhibition, Valencia, Spain, 2008, 17-23.

[25] Goetzberger A. and Hebling C., Photovoltaic materials, past, present, future, Sol. Energy Mater. Sol. Cells, 2000 (62) 1–19.

[26] Kwapil W., Kasemann M., Giesecke J., Michl B., Warta W., Investigations on the pre-breakdown of multicrystalline silicon solar cells, 23rd European Photovoltaic Solar Energy Conference and Exhibition, Valencia, Spain, Valencia, Spain, 2008, 1797-1800.

[27] Choi H. J., Bertoni M. I., Hofstetter J., Fenning D. P., Powell D. M., Castellanos S., and Buonassisi T., Dislocation density reduction during impurity gettering in multicrystalline silicon, 38th Photovoltaic Specialists Conference, 2012, 1-10.

[28] Sopori B., Silicon solar-cell processing for minimizing the influence of impurities and defects, J. Electron. Mater., 2002 (31) 972–980.

[29] Manna T., Mahajan S. Nanotechnology in the development of photovoltaic cells. Proceedings of the international conference on clean electrical power. 2007, 379–86.

[30] Ross R. B. et al. Endohedral fullerenes for organic photovoltaic devices. Nature Mater. 2009 (8) 208–212.

[31] Laird D. W. et al. Organic photovoltaic devices comparising fullerenes and

derivatives thereof. US patent 20080319207A1 (2008).

[32] Lenes M. et al. Fullerene bisadducts for enhanced open-circuit voltages and efficiencies in polymer solar cells. Adv. Mater. 2008 (20) 2116–2119.

[33] He F. et al. Tetrathienoanthracene-based copolymers for efficient solar cells. J. Am. Chem. Soc. 2011 (133) 3284–3287.

[34] Zhang Y. et al. Indacenodithiophene and quinoxaline-based conjugated polymers for highly efficient polymer solar cells. Chem. Mater. 2011 (23) 2289–2291.

[35] Chen H. Y. et al. Silicon atom substitution enhances interchain packing in a thiophene-based polymer system. Adv. Mater. 2010 (22) 371–375.

[36] Zhang Q. T. & Tour J. M. Low optical bandgap polythiophenes by an alternating donor/acceptor repeat unit strategy. J. Am. Chem. Soc. 1997 (119) 5065–5066.

[37] Huang F. et al. Development of new conjugated polymers with donor–pi-bridge–acceptor side chains for high performance solar cells. J. Am. Chem. Soc. 2009 (131) 13886–13887.

[38] Havinga E. E., Tenhoeve W. & Wynberg H., Alternate donor–acceptor small-band-gap semiconducting polymers — polysquaraines and polycroconaines. Synth. Met. 1993 (55) 299–306.

[39] Liang Y. Y. and Yu L. P., A new class of semiconducting polymers for bulk heterojunction solar cells with exceptionally high performance. Acc. Chem. Res. 2010 (43) 1227–1236.

[40] Kim J. Y. et al. New architecture for high-efficiency polymer photovoltaic cells

using solution-based titanium oxide as an optical spacer. Adv. Mater. 2006 (18) 572–576.

[41] Jabbour G. E., Kippelen B., Armstrong N. R. and Peyghambarian N., Aluminum based cathode structure for enhanced electron injection in electroluminescent organic devices. Appl. Phys. Lett. 1998 (73) 1185–1187.

[42] Lee C. H. Enhanced efficiency and durability of organic electroluminescent devices by inserting a thin insulating layer at the Alq3/cathode interface. Synth. Met. 1997 (91) 125–127.

[43] Hung L. S., Tang C. W. and Mason M. G., Enhanced electron injection in organic electroluminescence devices using an Al/LiF electrode. Appl. Phys. Lett. 1997 (70) 152–154.

[44] Su M. S. et al. Improving device efficiency of polymer/fullerene bulk heterojunction solar cells through enhanced crystallinity and reduced grain boundaries induced by solvent additives. Adv. Mater. 2011 (23) 3315–3319.

[45] Zhou H. X. et al. Development of fluorinated benzothiadiazole as a structural unit for a polymer solar cell of 7% efficiency. Angew. Chem. Int. Ed. 2011 (50) 2995–2998.

[46] Chen H. Y. et al. Polymer solar cells with enhanced open-circuit voltage and efficiency. Nature Photon. 2009 (3) 649–653.

[47] Liang Y. Y. et al. Highly efficient solar cell polymers developed via finetuning of structural and electronic properties. J. Am. Chem. Soc. 2009 (131) 7792–7799.

[48] Chen C. P., Chen Y. D. and Chuang S. C. High-performance and highly durable inverted organic photovoltaics embedding solution-processable vanadium oxides as an interfacial hole-transporting layer. Adv. Mater. 2011 (23) 3859–3863.

[49] Liang Y. Y. and Yu L. P. Development of semiconducting polymers for solar energy harvesting. Polym. Rev. 2010 (50) 454–473.

[50] Cheng Y. J., Yang S. H. & Hsu C. S. Synthesis of conjugated polymers for organic solar cell applications. Chem. Rev. 2009 (109) 5868–5923.

[51] Sun Y. M. et al. Efficient of air-stable bulk heterojunction polymer solar cells using MoOx as the anode interfacial layer. Adv. Mater. 2011 (23) 2226–2230.

[52] Tang C. W. Multilayer organic photovoltaic elements. US patent 4, 164,431 (1979).

[53] Tang C. W. Two-layer organic photovoltaic cell. Appl. Phys. Lett. 1986 (48) 183–185.

[54] Jorgensen M., Norrman K., Krebs F. C. Stability/degradation of polymer solar cells. Solar Energy Materials & Solar Cells, 2008 (92) 686–714.

[55] Mozer A. J., Niyazi Serdar Sariciftci. Conjugated polymer photovoltaic devices and materials, C R Chimie, 2006 (9) 568–577.

[56] Bett A. W., Dimroth F., Stollwerck G.; Sulima, O.V. III-V compounds for solar cell applications. Appl. Phys. A 1999 (69) 119–129.

[57] Dupuis R. D. III-V semiconductor heterojunction devices grown by metalorganic chemical vapor deposition. IEEE J. Sel. Top. Quantum Electron. 2000 (6) 1040–1050.

[58] Olson J. M., Friedman D. J., Kurtz S. High-efficiency III-V multijunction solar cells. Handbook of Photovoltaic Science and Engineering, 1st edition. Wiley: New York, NY, USA, 2003; Chapter 9, pp 359–411.

[59] Shimizu Y., Okada Y., Growth of high-quality GaAs/Si films for use in solar cell applications. J. Cryst. Growth, 2004 (265) 99–106.

[60] Tiwari S., Frank D. J., Empirical fit to band discontinuities and barrier heights in III-V alloy systems. Appl. Phys. Lett. 1992 (60) 630–632.

[61] Takamoto T., Ikeda E., Kurita H., Ohmori M. Over 30% efficient InGaP/GaAs tandem solar cells. Appl. Phys. Lett. 1997 (70) 381–383.

[62] Guter W., Schone J., Philipps S. P., Steiner M., Siefer G., Wekkeli A., Welser E., Oliva E., Bett A. W., Dimroth F., Current-matched triple-junction solar cell reaching 41.1% conversion efficiency under concentrated sunlight. Appl. Phys. Lett. 2009 (94) 223504.

[63] Jani O., Ferguson I., Honsberg C., Kurtz S., Design and characterization of GaN/InGaN solar cells. Appl. Phys. Lett. 2007 (91) 132117.

[64] Yang C. B., Wang X. L., Xiao H. L., Ran J. X., Wang C. M., Hu G. X., Wang X. H., Zhang X. B., Li M. P., Li J. M. Photovoltaic effects in InGaN structures with p-n junctions. Phys. Status Solidi A, 2007 (204) 4288–4291.

[65] Wu J., Walukiewicz W., Yu K. M., Ager J. W., Li S. X., Haller E. E., Lu H., Schaff W. J., Universal bandgap bowing in group-III nitride alloys. Solid State Commun. 2003 (127) 411–414.

[66] Casey H. C., Sell D. D., Wecht K. W., Concentration-dependence of absorption coefficient for n type and p type GaAs between 1.3 and 1.6 eV., J. Appl. Phys. 1975 (46) 250–257.

[67] King R. R., Haddad M., Isshiki T., Colter P., Ermer J., Yoon H., Joslin D. E., Karam N. H. Next-generation, high-efficiency III-V multijunction solar cells. Proceedings of the 28th IEEE Photovoltaic Specialists Conference, Anchorage, AK, USA, 2000, 998–1001.

[68] Kurtz S. R., Allerman A. A., Jones E. D., Gee J. M., Banas J. J., Hammons B. E. InGaAsN solar cells with 1.0 eV band gap, lattice matched to GaAs. Appl. Phys. Lett. 1999 (74) 729–731.

[69] Jackrel D. B., Bank S. R., Yuen H. B., Wistey M. A., Harris J. S., Dilute nitride GaInNAs and GaInNAsSb solar cells by molecular beam epitaxy, J. Appl. Phys. 2007 (101) 114916.

[70] Tanabe K., Morral A. F. I., Atwater H. A., Aiken D. J., Wanlass M. W., Direct bonded GaAs/InGaAs tandem solar cell. Appl. Phys. Lett. 2006 (89) 102106.

[71] Archer M. J., Law D. C., Mesropian S., Haddad M., Fetzer C. M., Ackerman A. C., Ladous C., King R. R., Atwater H. A., GaInP/GaAs dual junction solar cells on Ge/Si epitaxial templates. Appl. Phys. Lett. 2008 (92) 103503.

[72] Zahler J. M., Tanabe K., Ladous C., Pinnington T., Newman F. D., Atwater H. A., High efficiency InGaAs solar cells on Si by InP layer transfer. Appl. Phys. Lett. 2007 (91) 012108.

[73] Geisz J. F., Kurtz S., Wanlass M. W., Ward J. S., Duda A., Friedman D. J., Olson J. M., McMahon W. E., Moriarty T. E., Kiehl J. T., High-efficiency GaInP/ GaAs/ InGaAs triplejunction solar cells grown inverted with a metamorphic bottom junction. Appl. Phys. Lett. 2007 (91) 023502.

[74] Friedman D. J., Geisz J. F., Kurtz S. R., Olson J. M., 1-eV solar cells with GaInNAs active layer, J. Cryst. Growth 1998 (195) 409–415.

[75] Geisz J. F., Friedman D. J., Olson J. M., Kurtz S. R., Keyes B. M., Photocurrent of 1 eV GaInNAs lattice-matched to GaAs. J. Cryst. Growth 1998 (195) 401–408.

[76] http://www.compoundsemiconductor.net/article/91481-wafer-bonding-creates-record-breaking-four-junction-cell.html.

[77] Powalla M. The R&D potential of CIS thin-film solar modules. In: Proceedings of the 21st European photovoltaic solar energy conference. 2006, 1789–1795.

[78] Eldada L., Adurodija F., Sang B., Taylor M., Lim A., Taylor J. et al. Development of hybrid copper indium selenide photovoltaic devices by the FASST printing process, Proceedings of the 23rd European photovoltaic solar energy conference. 2008, 2142.

[79] Basol B. M, Oinabasi M., Aksu S., Wang J., Matus T., Johnson T., et al. Electroplating based CiGS technology for roll-to-roll manufacturing, Proceedings of the 23rd European photovoltaic solar energy conference. 2008, 2137.

[80] Powalla M. and Dimmler B. CIGS solar cells on the way to mass production: process statistics of a 30cm x 30cm module line. Solar Energy Materials & Solar Cells 2001 (67) 337–344.

[81] Sagana P., Wisz G., Bester M., Rudyj I. O., Kurilo I. V., Lopatynskij I. E., Virt I. S., Kuzma M., Ciach R., Study of CdTe and HgCdTe thin films grown on Si by pulse laser deposition., Thin Solid Films, 2005 (480–481) 318–321.

[82] Richards B. S., McIntosh K. R. Overcoming the poor short wavelength spectral response of CdS/CdTe photovoltaic modules via luminescence down-shifting: ray-tracing simulations, Progress in Photovoltaics: Research and Applications, 2007 (15) 27.

[83] Pfisterer F.. The wet-topotaxial process of junction formation and surface treatments of Cu S–CdS 2 thin-film solar cells, Thin Solid Films, 2003 (431–432) 470–476.

[84] Ferekides C. S., Marinskiy D., Viswanathan V., Tetali B., Palekis V., Selvaraj P., Morel D. L. High efficiency CSS CdTe solar cells, Thin Solid Films, 2000 (361-362) 520-526.

[85] Britt J., Ferekides C., Thin film CdS/CdTe solar cell with 15.8% efficiency, Appl. Phys. Lett. 1993 (62) 2851-2852.

[86] Zweibel K., Ullal H., Roedern V. Progress and issues in polycrystalline thin film PV technologies, 25th IEEE photovoltaic specialists' conference. 1996. 745–50.

[87] Jäger-Waldau A., Lux-Steiner M. Ch., Bucher E., MoS_2, $MoSe_2$, WS_2 and WSe_2 thin films for photovoltaics, Solid State Phenomena, 1994 (479) 37-38.

[88] Tsai M. L., Su S. H., Chang J. K., Tsai D. S., Chen C. H., Wu C., Li L. J., Chen L. J. and He J. H., Monolayer MoS_2 heterojunction solar cells, ACS Nano, 2014, 8 (8) 8317–8322.

Chapter 3 Synthesis and Characterization of WSe_2 Thin Films Using One-zone Furnace

3.1 Introduction

The group VI transition metal chalcogenide (TMC) semiconducting material MX_2 (M= W, Mo; X= Se, S) crystallize with a layered structure consisting of hexagonal X-M-X sandwiches separated by van der Waals gaps. Transition metal chalcogenides can be grown in the form of large, flexible, hexagonal plates which may be repeatedly cleaved, using adhesive tape, to give very thin crystals having the optic c axis normal to the major (001) crystal surfaces [1]. Because of the weak bonding between the layers, it has been possible to exfoliate (separate into single molecular layers) a number of layered dichalcogenides [2]. Due to their unique physical and electronic structure, the layered dichalcogenides display a variety of interesting properties and phases primarily due to their ‘‘two dimensional (2-D)’’ nature, including highly anisotropic mechanical, optical, and electrical properties [3].

Furthermore, the layered structure transition metal dichalcogenides MX_2 have demonstrated their potential in photovoltaics as a long term, inexpensive, and reliable energy technology, especially for large scale thin films solar cells [4][5]. These semiconductors exhibit several advantages over conventional semiconductors; for example, they are made of relatively abundant materials and the band gaps are well matched to the solar spectrum.

WSe_2 is a transition metal chalcogenide (TMC) semiconducting material of group VI with a layered crystal structure consisting of hexagonal Se-W-Se sandwiches separated by van der Waals gaps [6-8]. Among the TMCs, WSe_2 owns a direct band gap of 1.2-1.5 eV, which matches well with the solar spectrum and it has been proposed as a promising material for photovoltaic applications [9-13]. Indeed, solar devices based on a WSe_2 single crystal have been reported to possess conversion efficiencies in excess of 8% [14]. In addition we have simulated homo-junction and heterojunction photovoltaic devices based on the material properties measured in this work where ideal efficiencies well in excess of 20% have been obtained [15].

3.2 Properties

Tungsten di-selenide adopts a hexagonal crystalline structure consisting of hexagonal Se-W-Se sandwiches separated by van der Waals gaps. Every tungsten atom is covalently bonded to six selenium ligands in a trigonal prismatic coordination sphere while each selenium atom is bonded to three tungsten atoms in a pyramidal geometry, as is shown in Fig 3.1. The tungsten–selenium bond has a length of 0.2526 nm, and the distance between selenium atoms is 0.328 nm. The chemical and physical properties are shown in table 3.1.

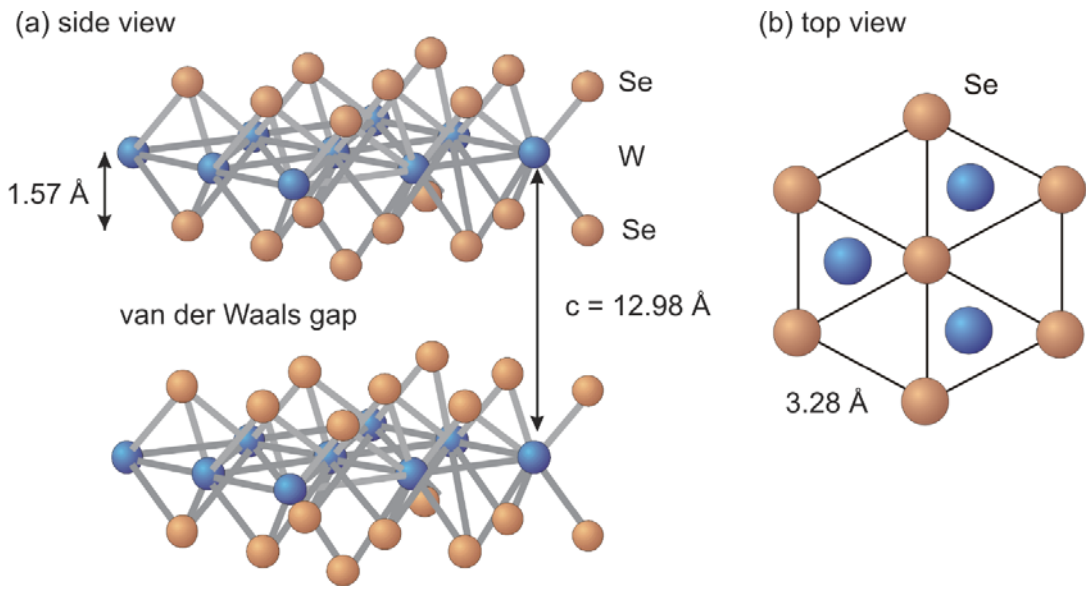

Figure 3.1 Structure of WSe_2 : (a) side view; (b) top view.

Table 3.1 Chemical and physical properties of WSe_2.

Molar mass	Color	State	Density
341.76 g/mol	grey to black	solid	9.32 g/cm^3
Melting point	Crystal structure	Lattice constant	Solubility in water
>1200 °C	Hexagonal	*a*=0.3297nm *c*=1.2982 nm	insoluble

3.3 Fabrication

Several methods have been employed to prepare WSe_2 thin films including electrodeposition, chemical bath deposition, and pulsed laser deposition [16-18]. In 2002,

tungsten diselenide thin films were electrodeposited by the galvanostatic route. In 2009, a chemical bath deposition method was used to prepare WSe_2 films. In 2012, WSe_2 thin films were obtained by pulsed laser deposition in vacuum and in a buffer gas atmosphere. The selenization in a selenium gas atmosphere was widely used to make WSe_2 thin films and has also been quite successful, however in the previously reported work either a two zone furnace was employed to directly grow the material or a single zone furnace process which necessitated post process removal of a selenium layer was used [19-21].

In our research, WSe_2 thin films were prepared by selenization of tungsten films under 1 atmosphere selenium pressure in a closed tube in a single-zone furnace without the need for removal of a selenium over layer after processing.

Tungsten films of about 100 nm thickness were DC-sputtered from a 50.8mm diameter 99.5% pure tungsten target onto 15 mm x 15 mm quartz substrates at room temperature. The substrates were thoroughly cleaned prior to insertion into the vacuum chamber with a base pressure of 1.33×10^{-4} Pa. Before the tungsten films were deposited onto the substrates the target itself was pre-sputtered for 5-10 minutes to clean away oxides on its surface. The operating pressure (with argon flow) was kept constant at 0.133 Pa during sputtering. The sputtering power was set to 40 watts and the deposition rate was about 3 nm/s. In order to obtain a uniform W film, the substrate was rotated at a speed of 20 revolutions per minute. Figure 3.2 shows the XRD of a tungsten thin film with a thickness of 100 nm.

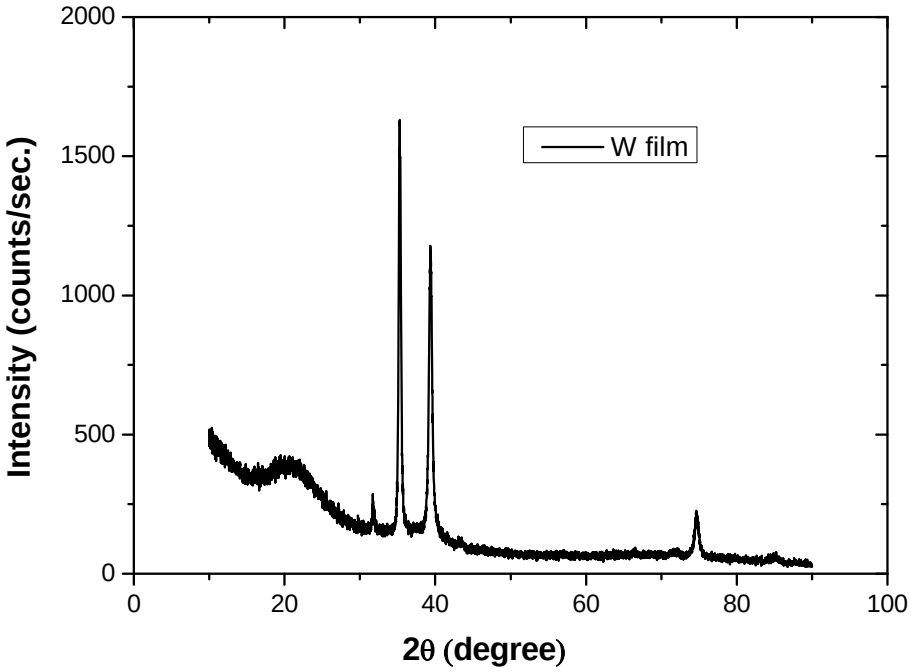

Figure 3. 2 XRD of W film (100 nm thickness).

A tungsten film and selenium powder (99.999%) were sealed into a quartz tube evacuated to 1.33×10^{-6} Pa, as is shown in Figure 3.3. The amount of selenium was controlled to yield 1 atmosphere of Se pressure at the process temperature. The sealed tubes were placed into a room temperature furnace and ramped to the process temperature at a rate less than 6 ^{o}C/min, baked for 18 hours and ramped down to room temperature at the same rate. Processing temperatures from 825 ^{o}C to 900 ^{o}C with a step of 25 ^{o}C were investigated.

Figure 3.3 Sealed quartz tube.

The results of these experiments clearly show that a single zone, single step process can produce high quality WSe_2 films. All WSe_2 thin films synthesized under different temperatures are highly oriented with the c axis predominantly perpendicular to the substrate. The mobility of WSe_2 thin films varied with process temperature and rises to 30 $cm^2V^{-1}s^{-1}$ at 875 ^oC, which is the largest thin film value reported. The preparation process, morphology, optical and electronic properties of the WSe_2 thin films are discussed in detail in the following.

3.4 Characterization

3.4.1 Raman Spectroscopy

In order to determine the lattice dynamics of WSe_2 thin films, a WSe_2 commercially purchased single crystal and the thin films grown here are investigated by

Raman spectroscopy employing a 633 nm excitation laser and 2400 mm^{-1} grating. Figure 3.4 shows the Raman spectra of the crystal and films prepared from 825 ^oC to 900 ^oC. At a processing temperature of 825 ^oC, the the E^1_{2g} and A_{1g} modes, which form a doublet, are obscured compared with the crystal [22]. The doublet becomes more pronounced with increasing growth temperature and at the 875 ^oC and 900 ^oC growth temperatures the Raman spectra of the WSe_2 films are very close to that of the crystal. It should be mentioned that if the Raman spectra is taken with a 1200 mm^{-1} grating only one peak at 252.5 cm^{-1} is observed for the crystal which was previously reported [23].

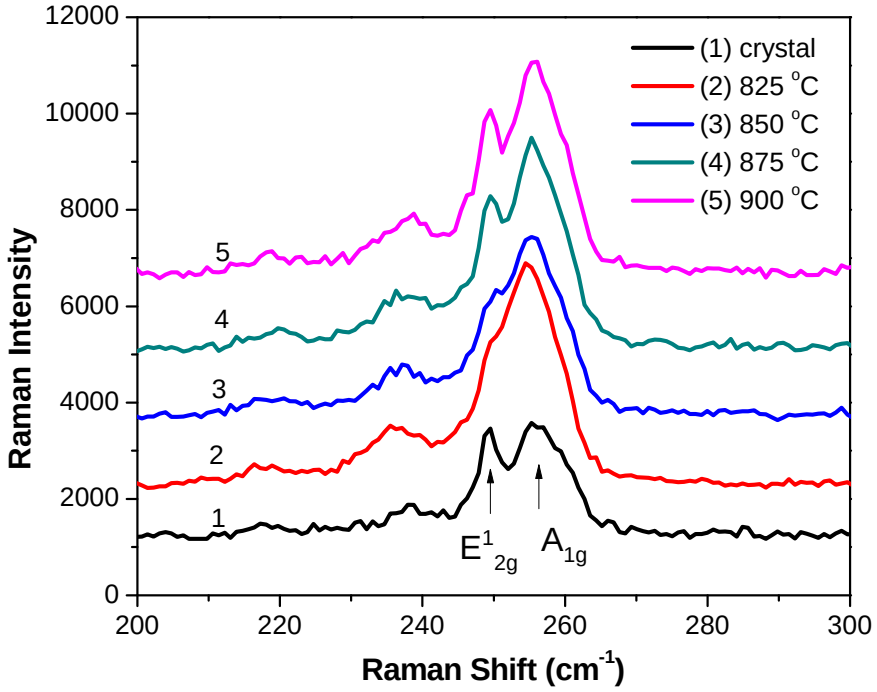

Figure 3.4 Raman Spectra of WSe_2 crystal and WSe_2 thin films fabricated under different temperatures: 825 ^oC, 850 ^oC, 875 ^oC, 900 ^oC.

3.4.2 XRD

The x-ray diffractograms (XRD) indicate that all the films exhibited the 2H-WSe_2 hexagonal structure. Figure 3.5 shows the x-ray diffractograms of WSe_2 thin films grown under different selenization temperatures, as well as the WSe_2 crystal which was bought from '2D Semiconductors'. The three primary peaks in the spectrum of the films correspond to the (002), (006), (008) peaks of WSe_2 which indicate that the c axis of the hexagonal structure is primarily perpendicular to the substrate.

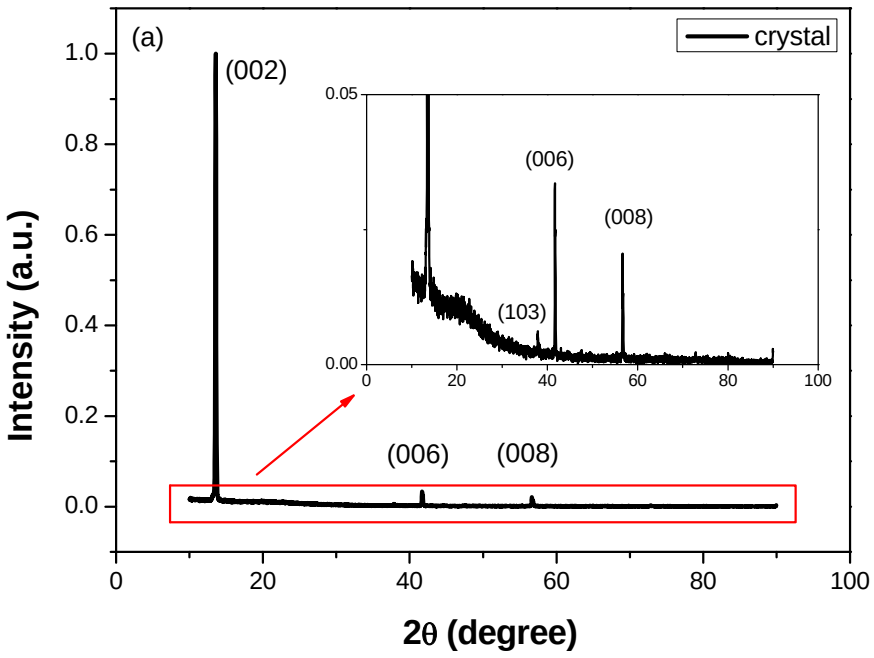

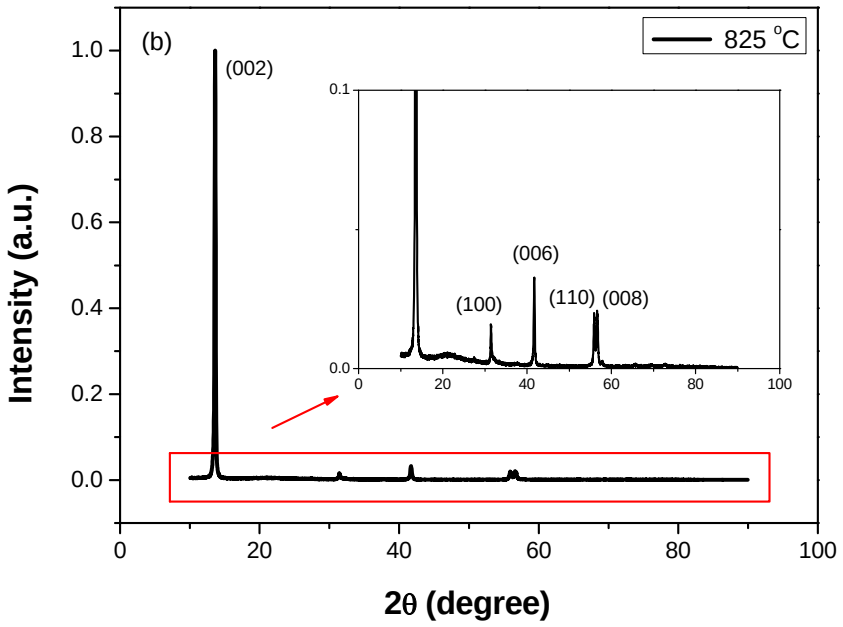
(b)
825 °C
(002)
(100)
(006)
(110)
(008)
Intensity (a.u.)
2θ (degree)

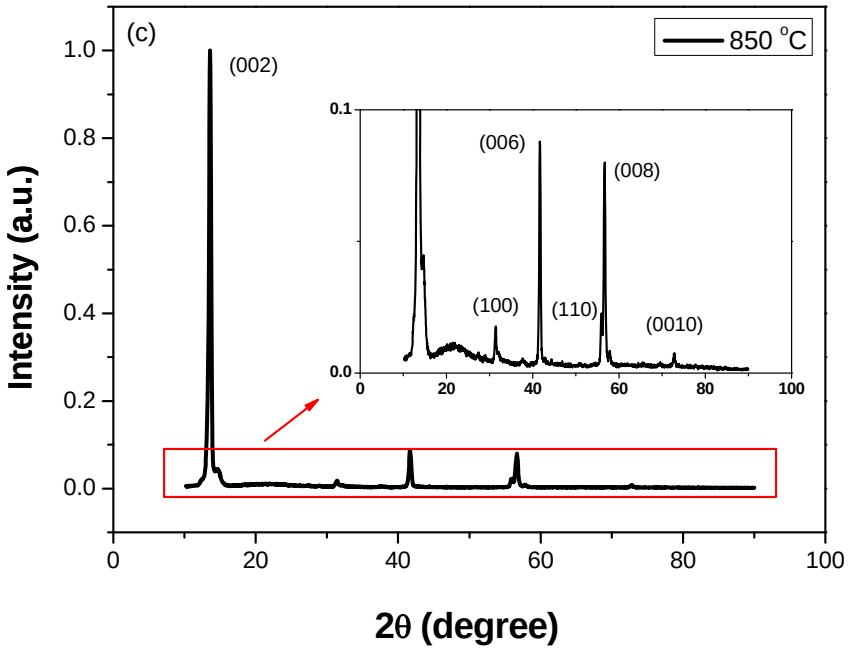
(c)
850 °C
(002)
(100)
(006)
(110)
(008)
(0010)
Intensity (a.u.)
2θ (degree)

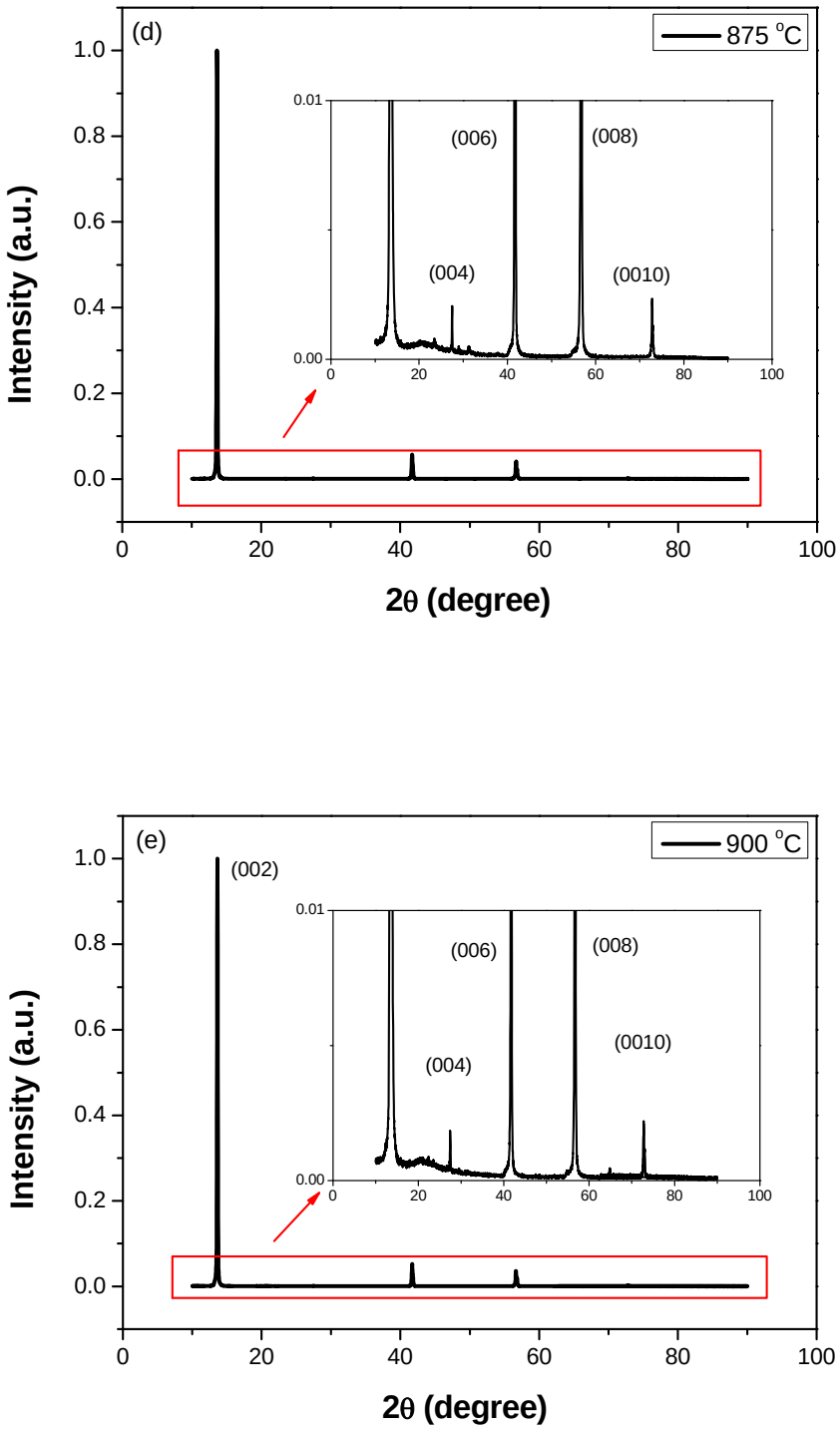

Figure 3.5 XRD patterns of WSe_2 crystal (a) and WSe_2 thin films under different synthesis temperatures: (b) 825 ºC, (c) 850 ºC, (d) 875 ºC, (e) 900 ºC.

The average grain size for different films, as seen in Fig. 3.6, was determined by the Debye-Scherrer formula:

$$L = (k\lambda)/(B\cos\theta)$$

where L is the crystallite size, k is a constant taken as 0.9, λ is the X-ray wavelength, B is the line width at half maximum height, and θ is the diffraction angle. The grain size increases with selenization temperature and ranges from 53.3 nm at 825 ^{o}C to 79.98 nm at 900 ^{o}C.

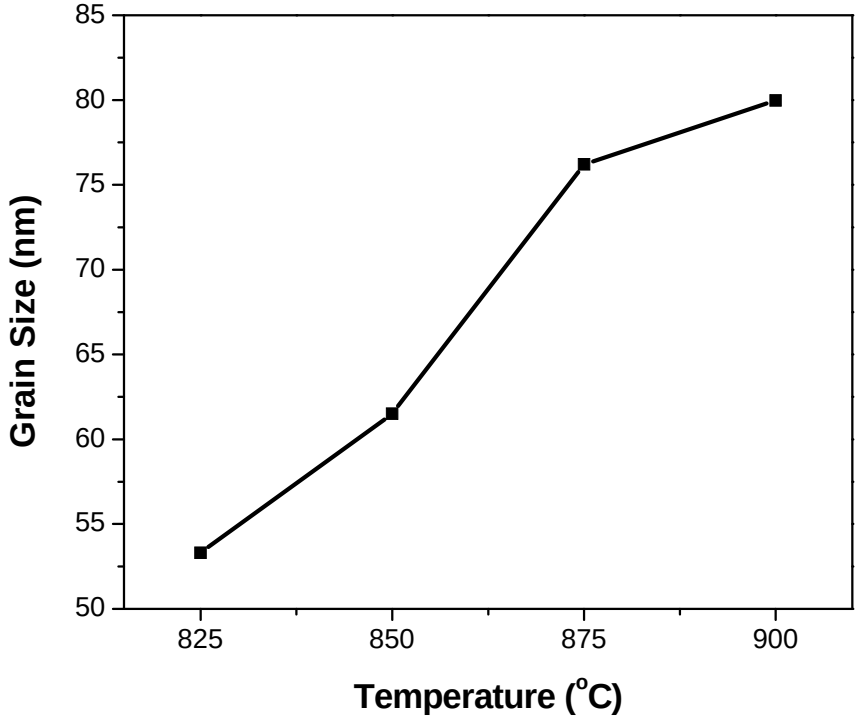

Figure 3.6 Grain sizes of WSe_2 thin films under different synthesis temperatures.

3.4.3 Optical Microscopy

The optical microscopy at 5x, 20x and 50x was employed to observe the surfaces of the samples, as is shown in Figure 3.7. From the images it is seen that films grown at 825 ^{o}C exhibit a smooth surface. Films grown at 900 ^{o}C appear to become rougher.

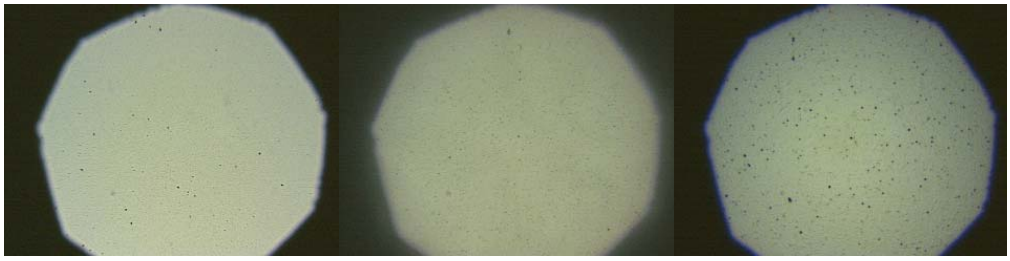

(a) WSe_2 film @ 825 ^{o}C Images (x5, x20, x50)

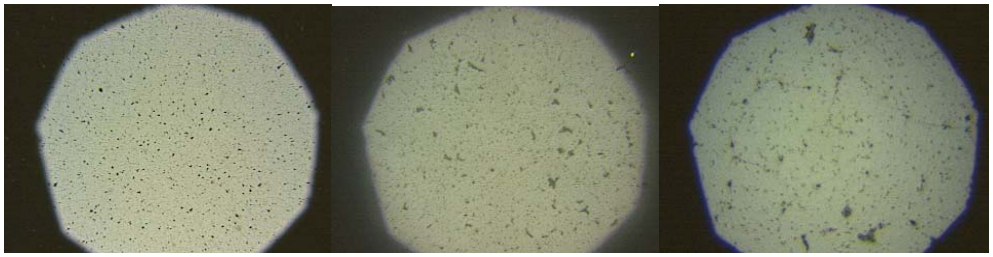

(b) WSe_2 film @ 850 ^{o}C Images (x5, x20, x50)

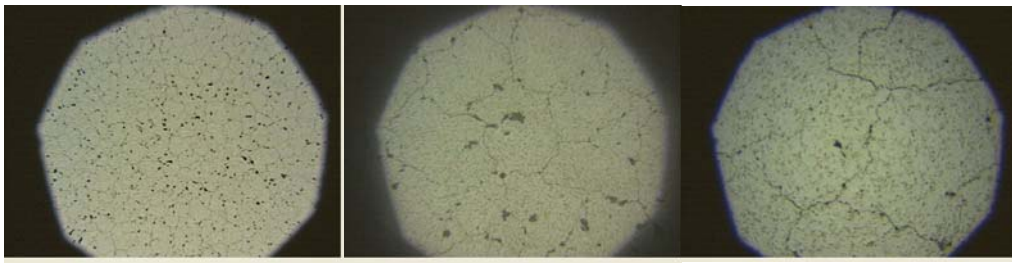

(c) WSe_2 film @ 875 ^{o}C Images (x5, x20, x50)

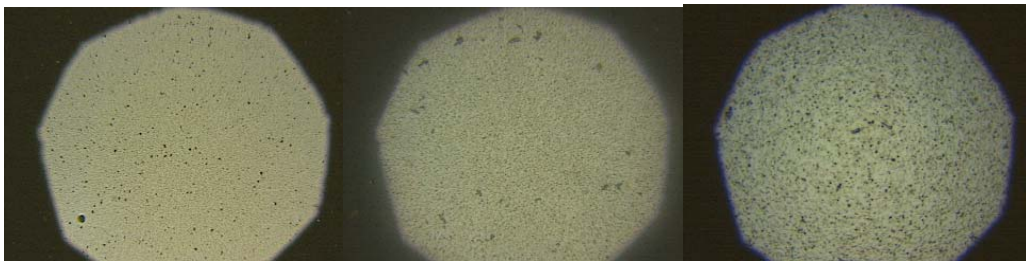

(d) WSe_2 film @ 900 ^oC Images (x5, x20, x50)

Figure 3.7 Magnified images of WSe_2 film surfaces under different temperatures: (a) 825 ^oC, (b) 850 ^oC, (c) 875 ^oC, (d) 900 ^oC.

3.4.4 SEM

The morphology of the films including both the planar surface and cross section were investigated by scanning electron microscopy (SEM). Figure 3.8 shows the SEM images of WSe_2 films under different synthesis temperatures. The surface structure of the film selenized at 825 ^oC, shown in Fig. 3.8(a), exhibits the hint of a hexagon, but it is not clearly formed. When the selenization temperature is 850 ^oC or greater, the grains on the surface are hexagonal as seen in Figs. 3.8(c), (e) and (g). In the cross section view of the film grown at 825 ^oC, shown in Fig. 3.8(b), it is seen that grains are columns that are perpendicular to the substrate. When the selenization temperature is increased to 850 ^oC, a bi-layer granular structure appears as seen in Fig. 3.8(d). In the top layer the grains are parallel to the substrate, and the bottom layer they are perpendicular. At selenization temperatures of 875 ^oC and 900 ^oC the grains are parallel to the substrate as seen in Figs. 3.8(f) and (h) respectively. It should be pointed out the x-ray diffraction data clearly indicates the crystalline orientation is independent of selenization temperature, while the

SEM data shows that the orientation of the largest dimension is a function of process temperature.

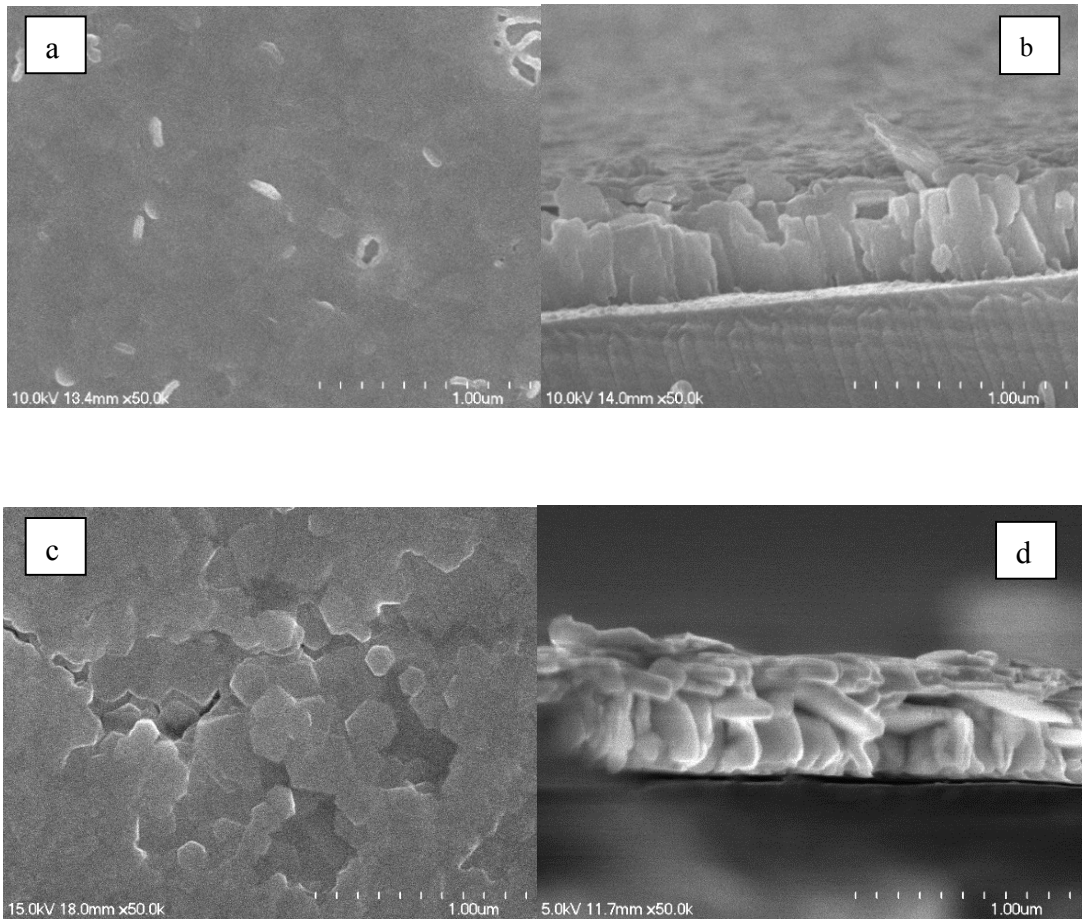

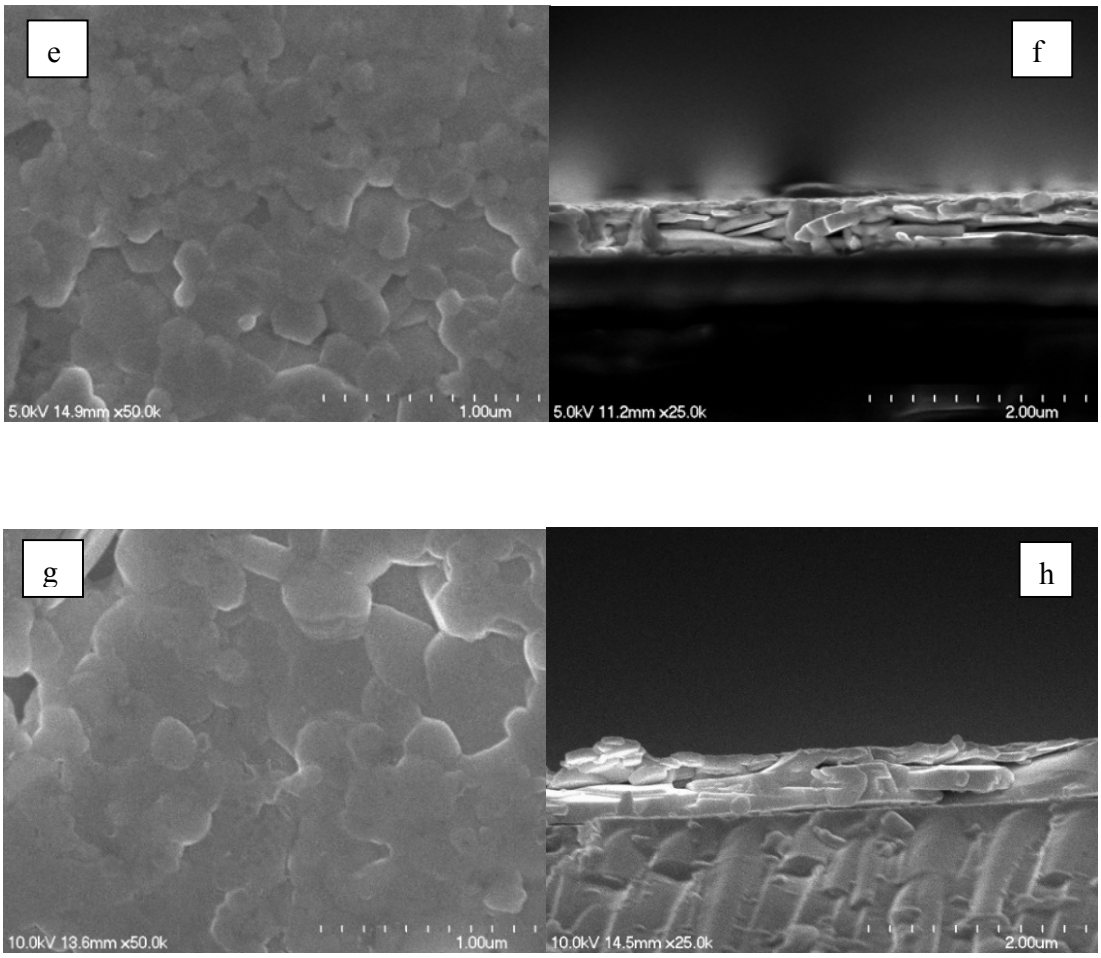

Figure 3.8 SEM of WSe_2 films fabricated under different temperatures (a) 825 ºC, planar surface; (b) 825 ºC, cross section; (c) 850 ºC, planar surface; (d) 850 ºC, cross section; (e) 875 ºC, planar surface; (f) 875 ºC, cross section; (g) 900 ºC, planar surface; (h) 900 ºC, cross section.

3.4.5 AFM

The morphology of the film surfaces was investigated by atomic force microscopy (AFM) in 2-D and 3-D presentation. Figure 3.9 shows the AFM planar surface images of the WSe_2 films. All AFM tests were carried out on a 5μm times 5μm area. With increasing selenization temperature, the granules become larger and clearer.

Meanwhile, the surface roughness also increases with the temperature. The roughness average (Ra) is 8 nm, 11 nm, 13 nm and 20 nm for films grown at 825, 850, 875 and 900 ^{o}C respectively.

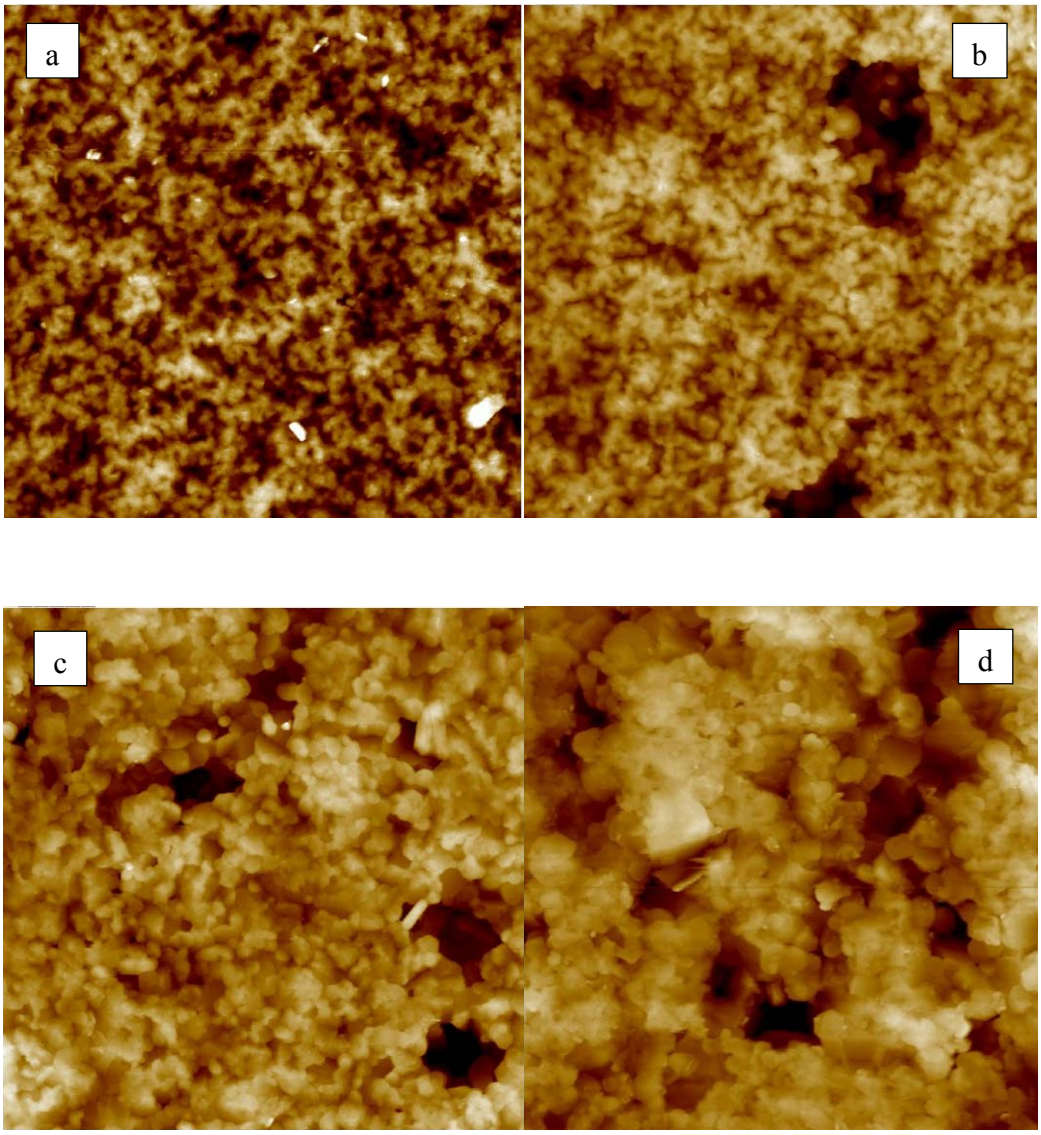

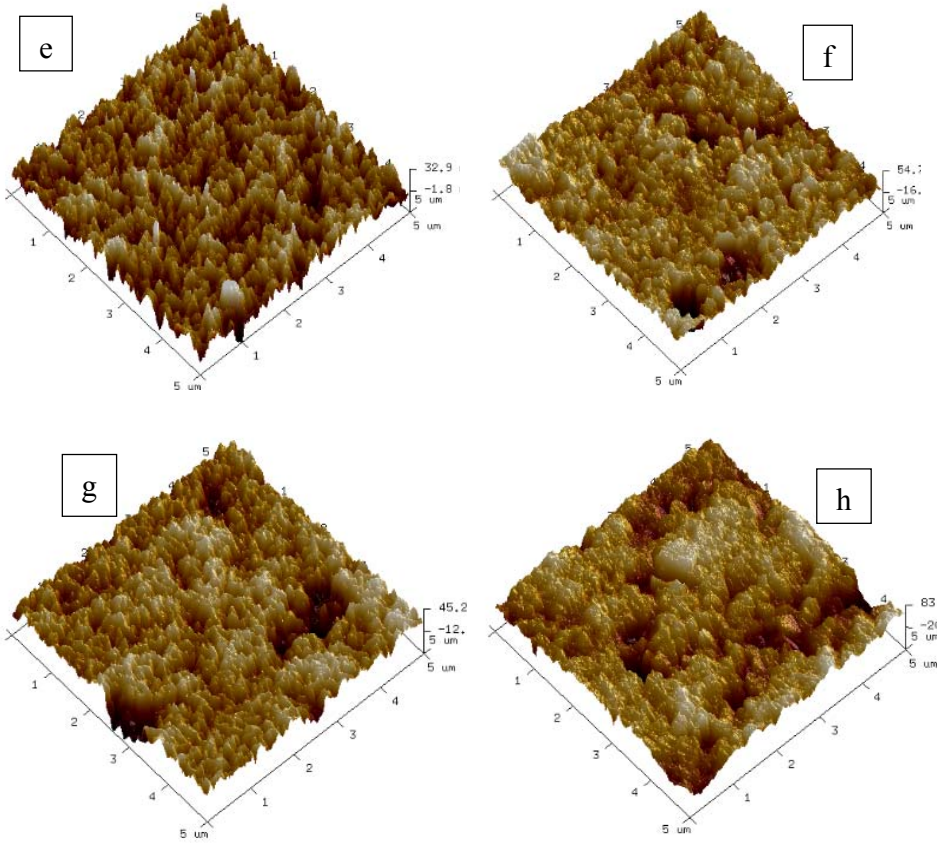

Figure 3.9 AFM 2D and 3D images of WSe_2 films fabricated under different temperatures: (a) 2D @825 ºC; (b) 2D @ 850 ºC; (c) 2D @ 875 ºC; (d) 2D @ 900 ºC. (e) 3D @825 ºC; (f) 3D @850 ºC; (g) 3D @875 ºC; (h) 3D @ 900 ºC.

3.4.6 Ellipsometric Characterization

Variable angle spectroscopic ellipsometry characterization of a WSe_2 single crystal sample and WSe_2 thin films at three angles (55º, 65º,75º) across the 350 nm-1200 nm wavelength was performed. The general oscillator model, employing 5 Lorentz oscillators and 1 Cody-Lorentz oscillator, was used to fit the data. The measured film thickness, as determined by profilometry, was employed in the ellipsometry analysis

where the final ellipsometrically determined film thickness was within 10% of the measured value. The spectroscopic ellipsometric fitting curves (Amplitude ratio Psi and phase difference Delta) are shown in Figure 3.10. The MSEs are between 12 and 17 for different WSe_2 thin films.

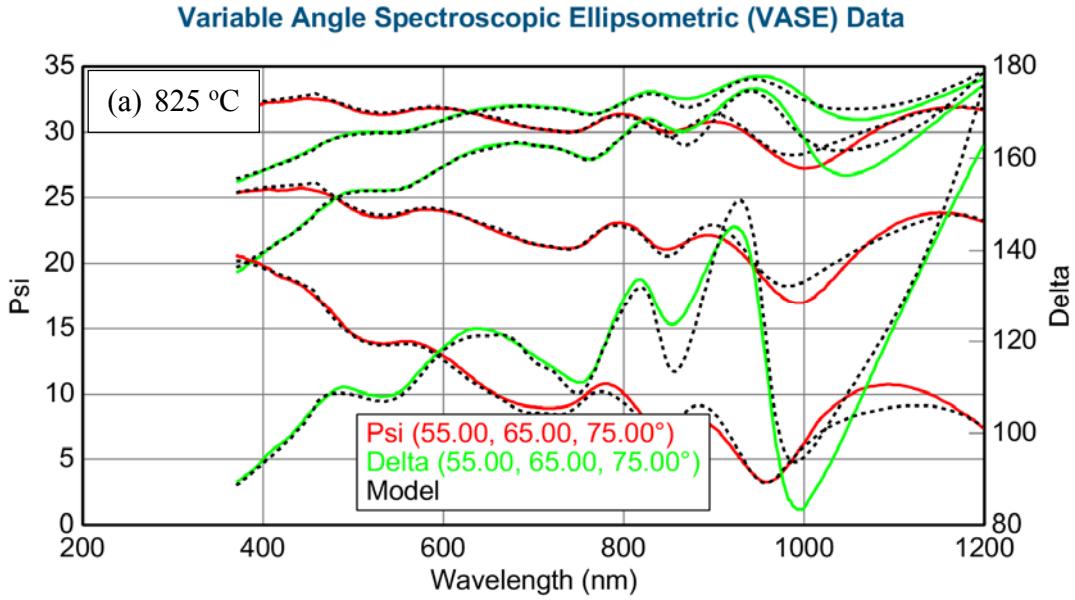

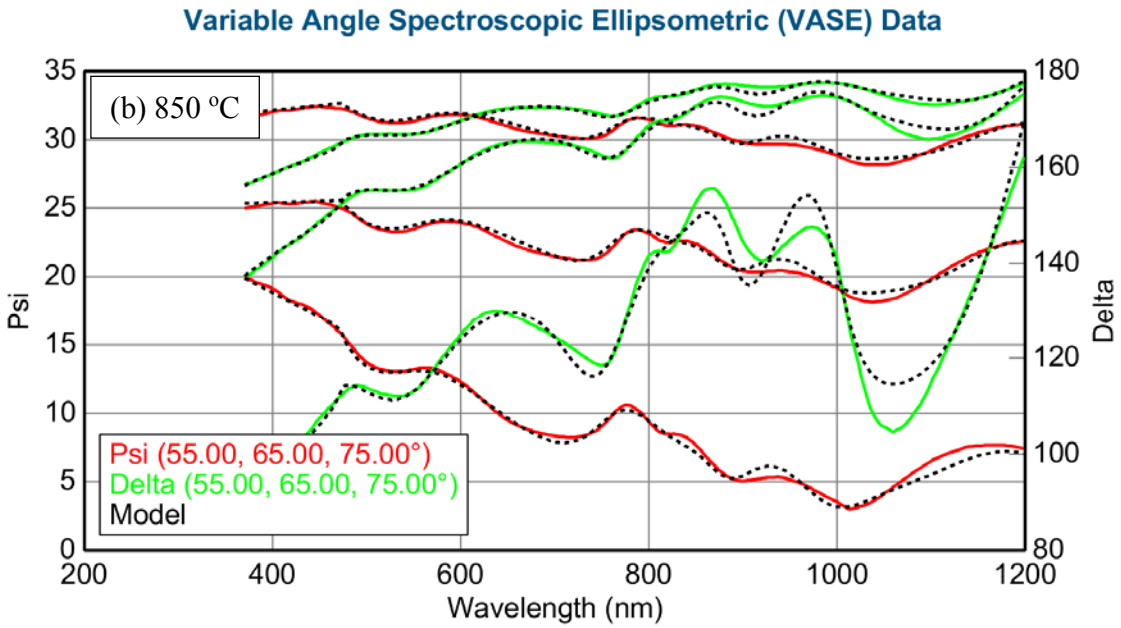
Variable Angle Spectroscopic Ellipsometric (VASE) Data
(b) 850 ºC
Psi (55.00, 65.00, 75.00°)
Delta (55.00, 65.00, 75.00°)
Model
Psi
Delta
Wavelength (nm)
0
5
10
15
20
25
30
35
80
100
120
140
160
180
200
400
600
800
1000
1200

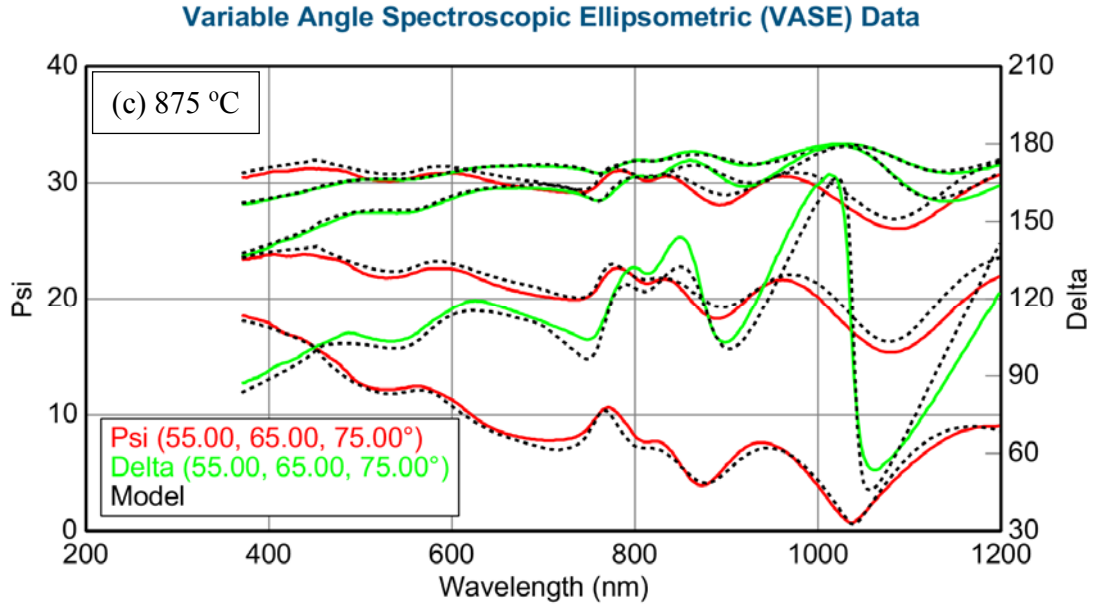
Variable Angle Spectroscopic Ellipsometric (VASE) Data
(c) 875 ºC
Psi (55.00, 65.00, 75.00°)
Delta (55.00, 65.00, 75.00°)
Model
Psi
Delta
Wavelength (nm)
0
10
20
30
40
30
60
90
120
150
180
210
200
400
600
800
1000
1200

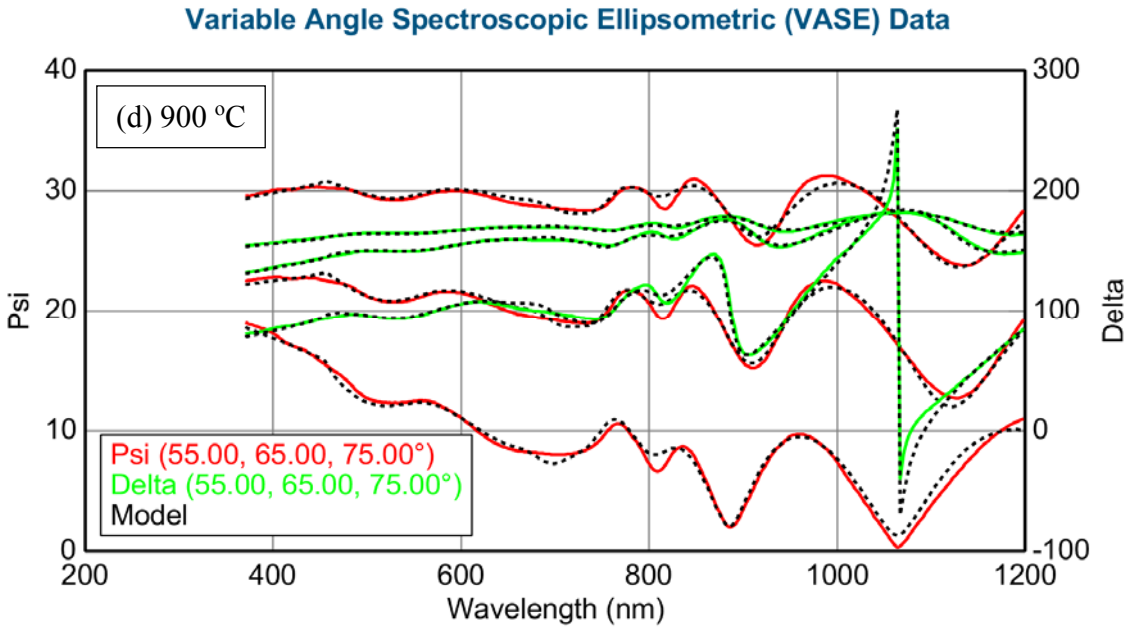

Figure 3.10 Spectroscopic ellipsometric data fitting curves of WSe_2 films under different temperatures: (a) 825 °C, (b) 850 °C, (c) 875 °C, (d) 900 °C.

The dispersion of the refractive index n and extinction coefficient k of the WSe_2 thin films, as well as the crystal, are shown in Fig. 3.11 and Fig. 3.12. The WSe_2 films fabricated at 875 °C are very similar to the crystal. There are two local maximums A and B at 580 nm and 770 nm in the dispersion curve of k, whereas n shows two local dips. The extinction coefficient k is in good agreement with previously reported results [24].

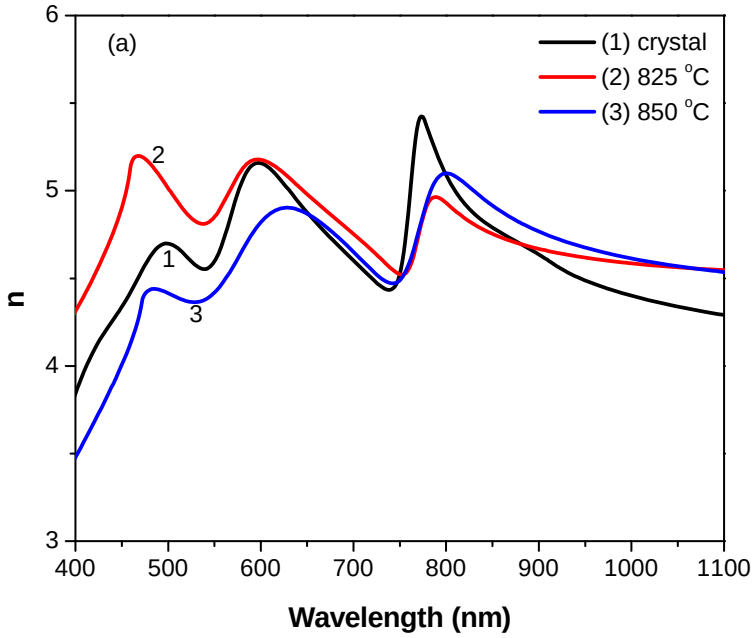

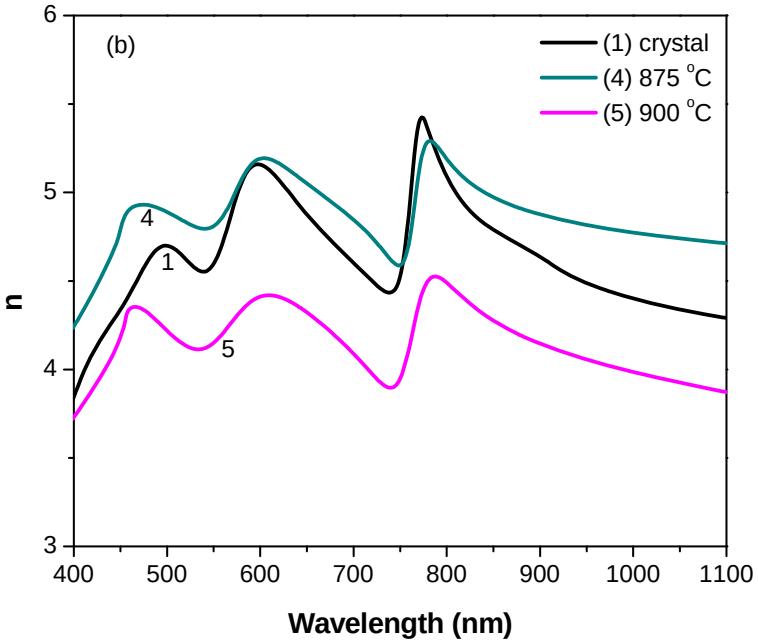

Figure 3.11 Dispersion of refractive index n of WSe_2 crystal and WSe_2 thin films: (a) crystal, 825 °C, and 850 °C; (b) crystal, 875 °C, 900 °C.

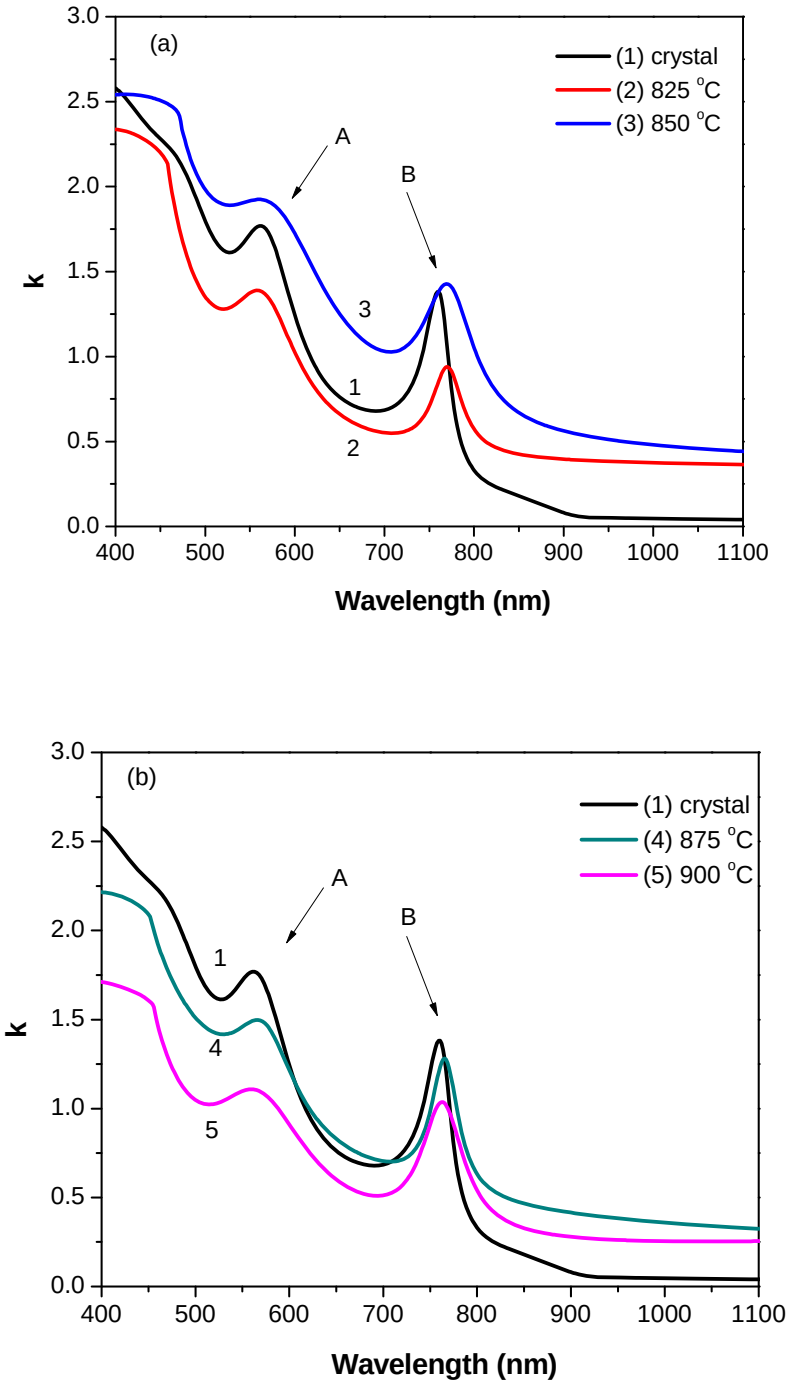

Figure 3.12 Extinction coefficient k of WSe_2 crystal and WSe_2 thin films: (a) crystal, 825 ºC, and 850 ºC; (b) crystal, 875 ºC, 900 ºC.

3.4.7 Transmission Optical Spectra

Both transmission spectra and reflection spectra were also acquired in a UV-Vis spectrophotometer for all the films under different temperatures, as seen in Fig. 3.13, from which we can calculate the absorption coefficient. The crystal was so thick that data could not be obtained.

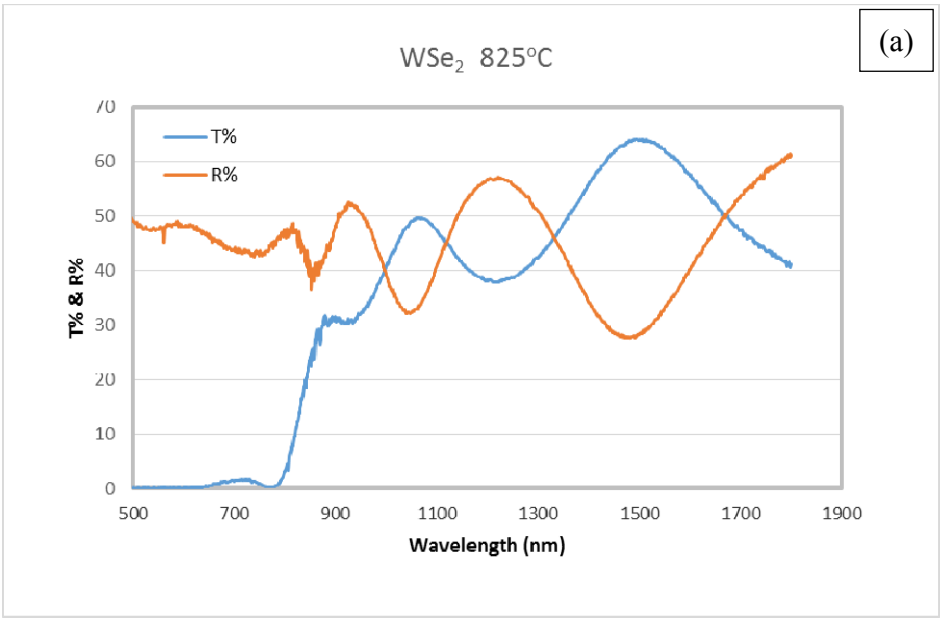

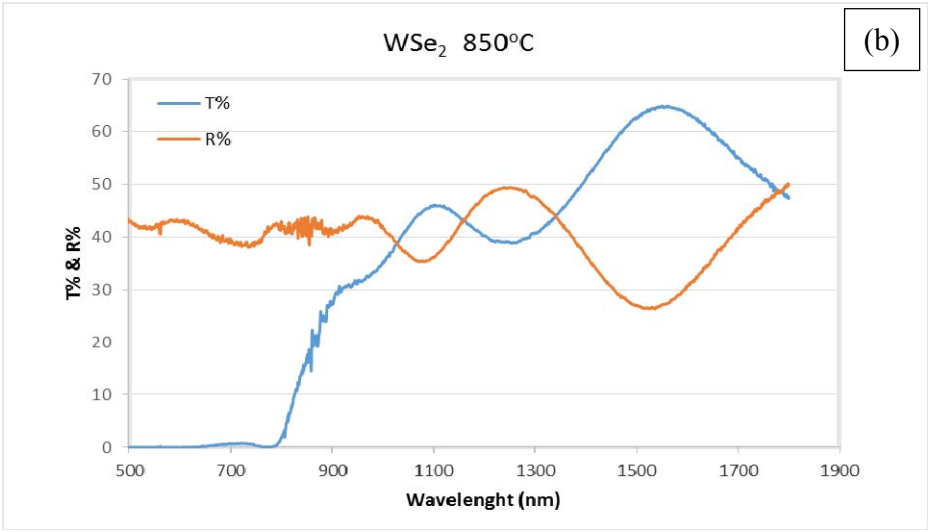

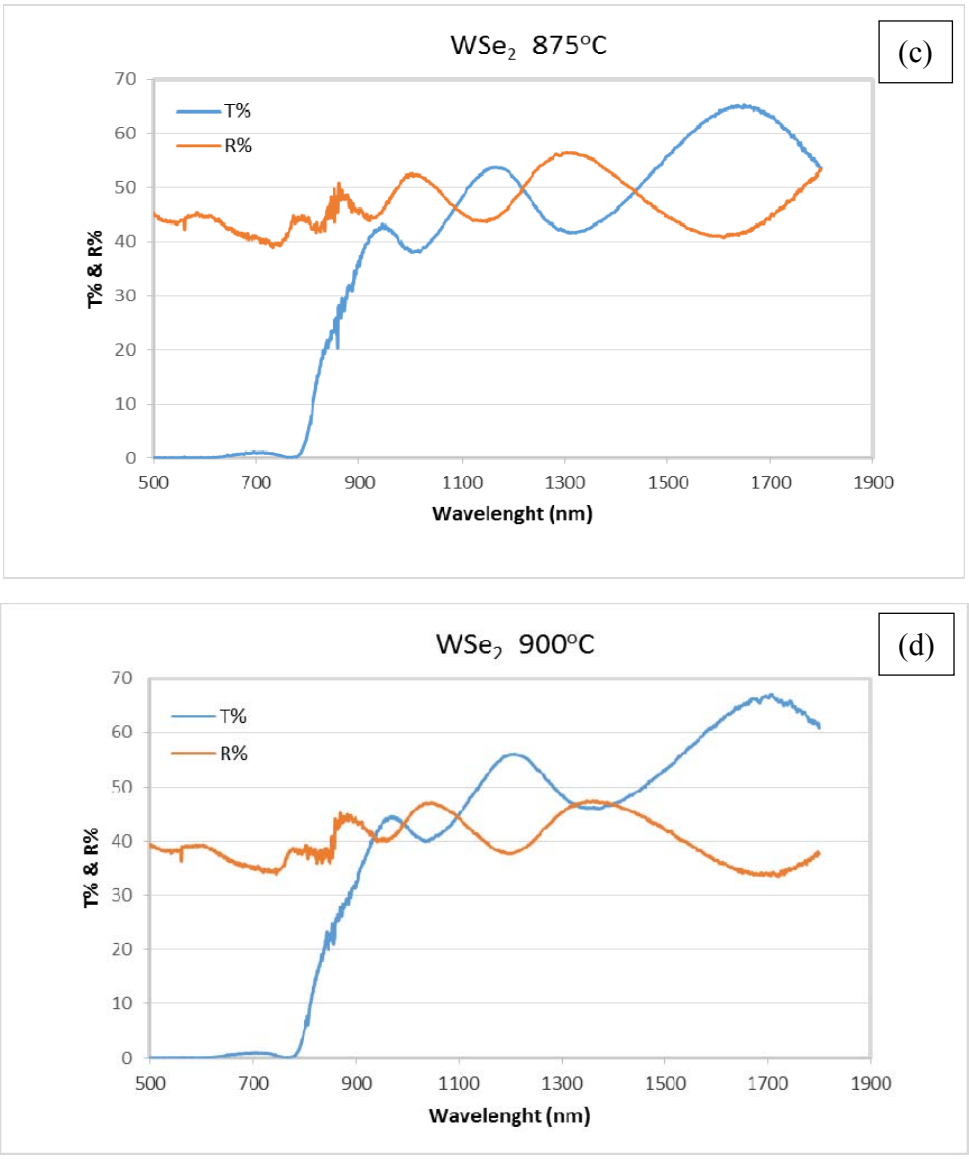

Figure 3.13 Transmittance and reflection spectra of WSe_2 films under different temperatures: (a) 825 ºC, (b) 850 ºC, (c) 875 ºC, (d) 900 ºC.

3.4.8 Absorption Coefficient

The transmission spectra as well as the extinction coefficient obtained from ellipsometry were employed to calculate the absorption coefficient. Figure 3.14 is the

absorption coefficient obtained from ellipsometry and includes the single crystal.

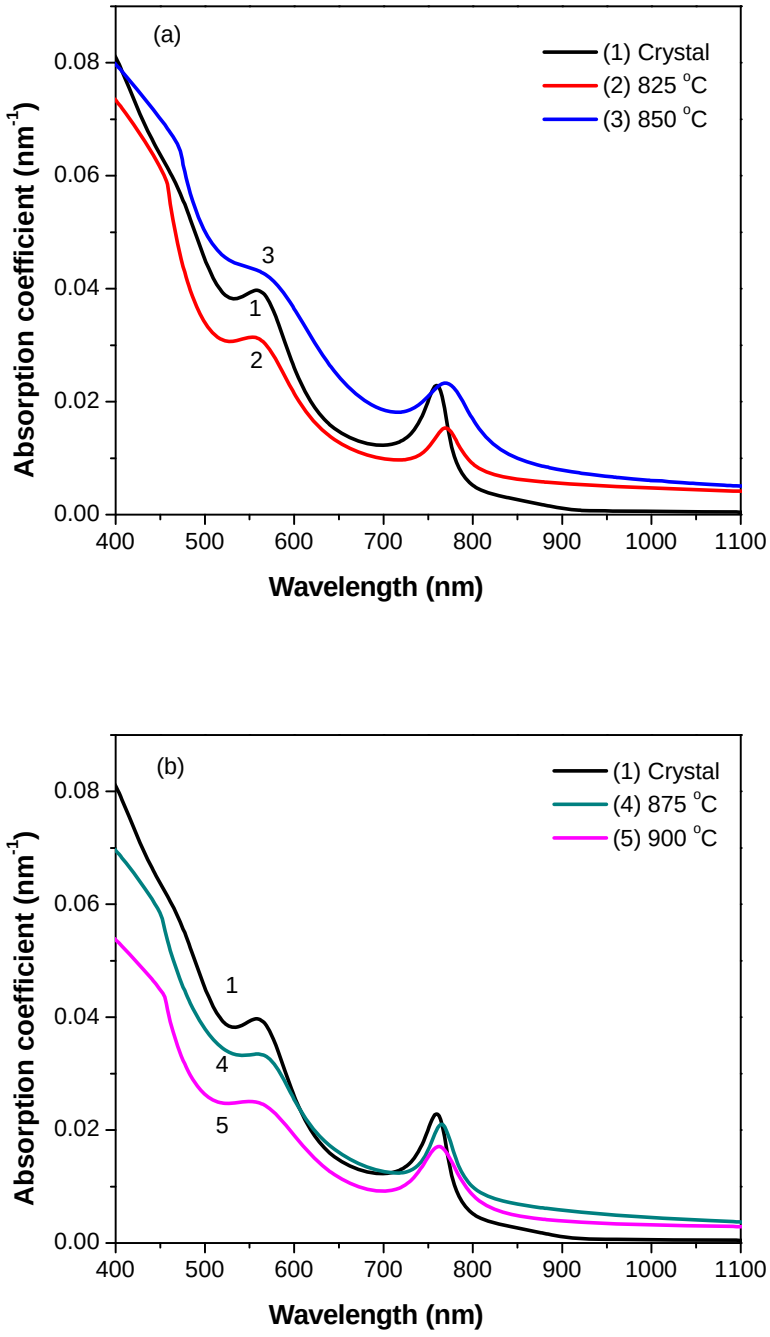

Figure 3.14 Absorption coefficient calculated from ellipsometry data for WSe_2 crystal and thin films under different temperatures: (a) crystal, 825 ºC, and 850 ºC; (b) crystal, 875 ºC, 900 ºC.

Figure 3.15 shows the absorption coefficient obtained from transmission data. It should be mentioned that reflection was taken into account for calculations based on data taken from the spectrophotometer. For wavelengths below about 600nm the transmission dropped to 0 so the absorption coefficient data obtained in that spectral region is an underestimate. The data agree well for the spectral region above 600nm.

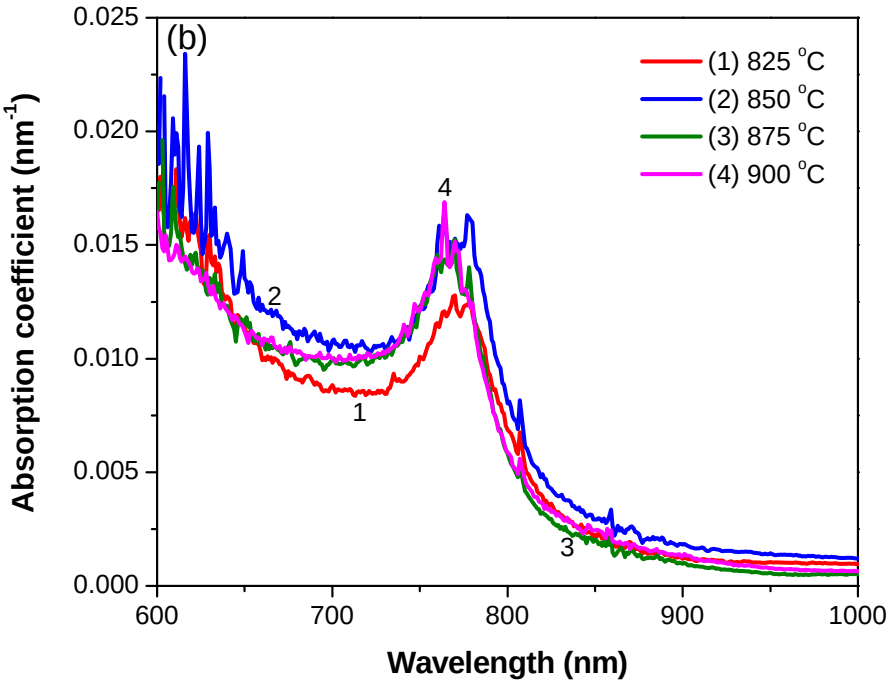

Figure 3.15 Absorption coefficient calculated from transmission data for WSe_2 crystal and thin films under different temperatures.

3.4.9 Bandgap

Tauc plots to determine the direct and indirect band gaps were generated from both sets of absorption coefficients. Typical results are seen in Fig.3.16 for a film selenized at 875 °C. Tauc plots from both sets of absorption coefficients yielded very

close direct and indirect band gap values, and the difference was smaller than 5% range in most cases.

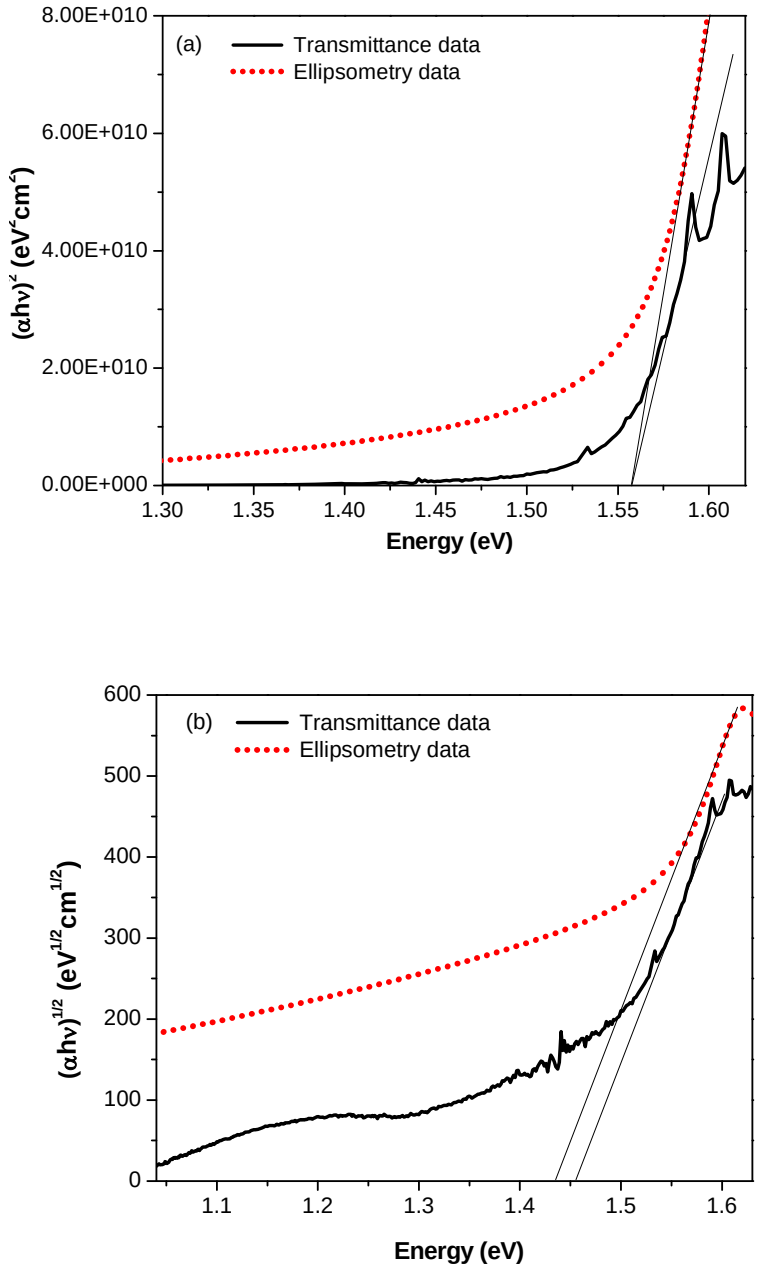

Figure 3.16 Tauc plots of a WSe_2 thin film from both transmittance and ellipsometry data. (a) Direct band gap, (b) Indirect band gap. The WSe_2 thin film is made at 875 ºC.

In view of the issues associated with the transmission data Table 3.1 shows the band gaps obtained only from ellipsometry. All the films selenized at different temperatures have similar direct band gap values from 1.50 eV to 1.56 eV. The WSe_2 crystal data yielded a 1.59 eV direct band gap and a 1.25 eV indirect band gap.

Table 3.2 Band gaps of WSe_2 obtained from ellipsometry spectra.

WSe_2	crystal	825 ^oC	850 ^oC	875 ^oC	900 ^oC
Dircet band gap (eV)	1.59	1.54	1.50	1.56	1.54
Indircet band gap (eV)	1.25	1.38	1.28	1.43	1.42

3.4.10 Hall Effect Test

Electrical transport properties, including the carrier type, mobility, and carrier concentration, were investigated by performing Hall Effect and van der Pauw measurements. All measurements were performed at room temperature and the Hall Effect measurements employed a magnetic field of 1.3 T. Electrical contact was made with silver paint. All films are clearly p-type as indicated by the Hall voltage. Figure 3.17 shows the carrier concentration and Hall mobility as a function of selenization temperature.

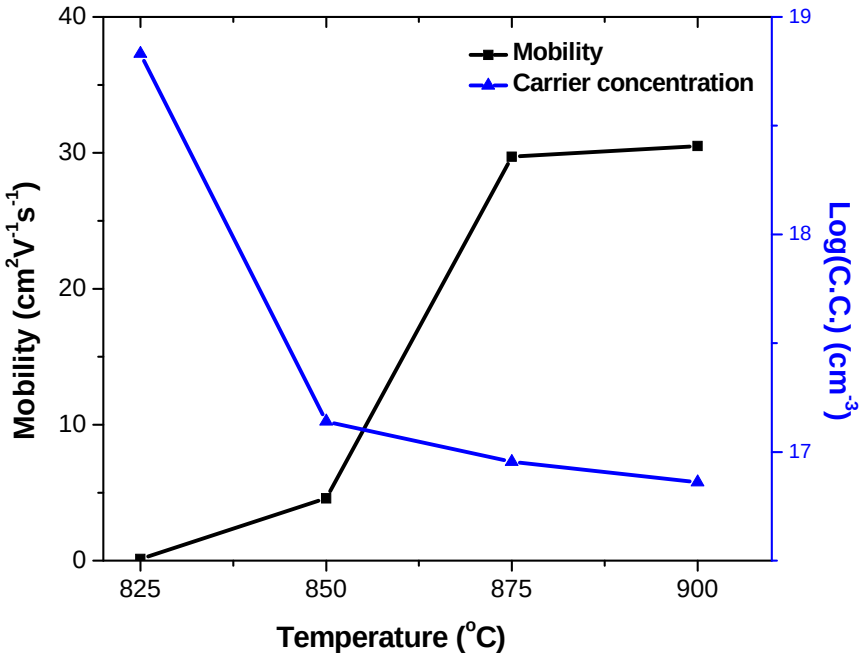

Figure 3.17 Mobility and carrier concentration (Log(C.C.)) of WSe_2 thin films as a function of selenization temperature.

The carrier concentration decreases by nearly 2 orders of magnitude for a 25 ºC increase in selenization temperature from 825 ºC to 850 ºC, while the mobility increases from 0.1 $cm^2V^{-1}s^{-1}$ to a value of about 5 $cm^2V^{-1}s^{-1}$, a 50 fold increase. The next 25 ºC increment drives the hall mobility to the highest value yet reported in thin films, approximately 30 $cm^2V^{-1}s^{-1}$ although the carrier concentration decreases just slightly. These properties are essentially the same at a processing temperature of 900 ºC.

3.5 Discussion

In relating all the results several useful conclusions can be drawn. The Raman

spectra is an excellent initial indicator of the film quality. At a processing of temperature of 825 ºC only a single Raman peak is observed and the film has poor mobility and high carrier concentration. As the processing temperature increases the E^1_{2g} peak begins to appear, and the more pronounce this peak the higher the mobility and lower the carrier concentration. In the crystal the E^1_{2g} and A^{1g} peaks are nearly the same magnitude.

The SEM and AFM micrographs and grain size data support the changes in film properties. As the processing temperature increases, the grain size increases, while the crystal orientation stays the same, as shown by x-ray diffraction. However, the micrographs show a distinct change in microstructure. At lower process temperatures the grains are mainly perpendicular to the substrate while at the higher temperatures the grains, while maintaining their crystal orientation, are now plate like and parallel to the substrate. This transition corresponds directly to the measured increase in carrier mobility. It should be pointed out that the mobility measurement is taken with current flowing parallel to the substrate thus the structure change may account for this. However, in a photovoltaic device current flows perpendicular to the substrate, thus it is not all clear if the maximum mobility material would be the best choice for a device. The material processed at 850 ºC has a low carrier concentration, like the high mobility samples but exhibits a low mobility. The micrograph (Figure 4d) shows grains perpendicular to the substrate topped with a layer parallel to the substrate. This structure may account for the low mobility parallel to the substrate.

3.6 Conclusion

In summary, a single zone furnace has been employed to grow highly c-axis oriented, single phase p-type WSe_2 thin films, without the need for post processing selenium film removal. The band gap, absorption coefficient and mobility indicate that this material could be an excellent photovoltaic absorber.

References

[1] S. H. El-Mahalawy and B. L. Evans, The thermal expansion of 2H-MoS_2, 2H-$MoSe_2$ and 2H-WSe_2 between 20 and 800°C, J. Appl. Cryst. 1976 (9) 403.

[2] R. A. Gordon, D. Yang, E. D. Crozier, D. T. Jiang, and R. F. Frindt, Structures of exfoliated single layers of WS_2 , MoS_2, and $MoSe_2$ in aqueous suspension, Physical Review B, 2002 (65) 125407.

[3] A. A. Balchin, Crystallography and Crystal Chemistry of Materials with Layered Structures, edited by F. Levy (Reidel, Dordrecht, 1976). Chap. 1.

[4] A. Jäger-Waldau, M. Ch. Lux-Steiner, E. Bucher, MoS_2, $MoSe_2$, WS_2 and WSe_2 thin films for photovoltaics, Solid State Phenomena, 1994 (479) 37-38.

[5] A. Aruchamy, Photoelectrochemistry and Photovoltaics of Layered Semiconductors, Kluver Academic Publ., Dordrecht, NL, 1992.

[6] Th. Straub, K. Fauth, Th. Finteis, M. Hengsberger, R. Claessen, P. Steiner, S. Hüfner, P. Blaha, Valence-band maximum in the layered semiconductor WSe_2: Application of constant energy contour mapping by photoemission, Physical Review B, 1996 (53) 152.

[7] O. Lang, Y. Tomm, R. Schalf, C. Pettenkofer, W. Jaegermann, Single crystalline GaSe/WSe_2 heterointerfaces grown by van der Waals epitaxy. II. Junction characterization, Journal of Applied Physics, 1994 (75) 7814.

[8] G. K. Solanki, D. N. Gujarathi, M. P. Deshoande, D. Lakshminarayana, M. K. Agarwal, Transport property measurements in tungsten sulphoselenide single crystals grown by a CVT technique, Crystal Research and Technology, 2008 (43) 179.

[9] W. H. Strehlow, E. L. Cook, Compilation of energy band gaps in elemental and binary compound semiconductors and insulators, Journal of Physical and Chemical Reference Data, 1973 (2) 163.

[10] T. Tsirlina, S. Cohen, H. Cohen, L. Sapir, M. Peisach, R. Tenne, A. Matthaeus, S.Tiefenbacher, W. Jaegermann, E. A. Ponomarev, C. Levy-Clement, Growth of crystalline WSe_2 and WS_2 films on amorphous substrate by reactive (Van der Waals) rheotaxy, Solar Energy Materials and Solar Cells, 1996 (44) 457.

[11] E. Lassner, W-D. Schubert, Tungsten: properties, chemistry, technology of the element, alloys, and chemical compounds, Kluwer Academic / Plenum Publishers, New York, 1999.

[12] B. Davey, B. L. Evans, The optical properties of $MoTe_2$ and WSe_2, Physica Status Solidi A, 1972 (13) 483.

[13] J. C. Bernede, J. Pouzet, E. Gourmelon, H. Hadouda, Recent studies on photoconductive thin films of binary compounds, Synthetic Metals, 1999 (99) 45.

[14] M. Vogt, M. Ch. Lux-Steiner, P. Dolatzoglou, E. Bucher, Comparison between the photovoltaic performance of WSe_2 heterojunctions prepared by ITO or ZnO magnetron sputtering, Photovoltaic Solar Energy Conference, Florence, Italy, 1988, 1112.

[15] Qinglei Ma, Hrachya Kyureghian, Joel D. Banninga, N. J. Ianno, Thin Film WSe_2 for use as a photovoltaic absorber material, MRS Proceedings, 2014, 1670, mrss14-1670-e01-02 doi:10.1557/opl.2014.739.

[16] J. Jebaraj Devadasan, C. Sanjeeviraja, M. Jayachandran, Electrosynthesis and characterization of n-WSe_2 thin films, Materials Chemistry and Physics, 2002 (77)

397.

[17] P. P. Hankare, A. H. Manikshete, D. J. Sathe, P. A. Chate, and K. C. Rathod, Novel chemical synthetic route and characterization of tungsten diselenide thin films, Materials Chemistry and Physics, 2009 (113) 183.

[18] S. N. Grigoriev, V. Yu. Fominski, A. G. Gnedovets, and R. I. Romanov, Experimental and numerical study of the chemical composition of WSe_x thin films obtained by pulsed laser deposition in vacuum and in a buffer gas atmosphere, Applied Surface Science, 2012 (258) 7000.

[19] A. Jager-Waldau, E. Bucher, WSe_2 thin films prepared by soft selenization, Thin Solid Films, 1991 (200) 157.

[20] J. Pouzet, J. C. Bernede, A. Khellil, H. Essaidi, S. Benhida, Preparation and characterization of tungsten diselenide thin films, Thin Solid Films, 1992 (208) 259.

[21] A Khelil, H Essaidi, J C Bernede, A Bouacheria, J Pouzet, WSe_2 thin-film realization by synthesis and by tarnishing, J. Phys.: Condens. Matter, 1994 (6) 8527.

[22] P. Tonndorf, R. Schmidt, P. Böttger, X. Zhang, J. Börner, A. Liebig, M. Albrecht, C. Kloc, O. Gordan, D. R. T. Zahn, S. Michaelis de Vasconcellos, R. Bratschitsch, Photoluminescence emission and Raman response of monolayer MoS_2, $MoSe_2$, and WSe_2, Optics Express, 2013 (21) 4908.

[23] H. Sahin, S. Tongay, S. Horzum, W. Fan, J. Zhou, J. Li, J. Wu, F. M. Peeters, Anomalous Raman spectra and thickness-dependent electronic properties of WSe_2, Physical Review B, 2013 (87) 165409.

[24] G. Salitra, G. Hodes, E. Klein, R. Tenne, Highly oriented WSe_2 thin films prepared by selenization of evaporated WO_3, Thin Solid Films, 1994 (245) 180.

Chapter 4 Simulation of WSe_2 Solar Cells with PC1D

4.1 Introduction

The software package PC1D (Personal Computer One Dimensional) is one of the most commonly used modelling programs for semiconductor device simulation, with an emphasis on solar cells [1-5]. It is widely used for both research and industrial purposes, not only helping users to understand the fundamental mechanisms and operation of solar cells, but also efficiently giving reliable and predictable results [6].

Based on the analysis in Chapter 3, WSe_2 has the potential to be an absorber material. In this work, simulation of WSe_2 solar cells are carried out with PC1D software. The performance of homo-junction and hetero-junction devices is investigated and the simulation results will show that WSe_2 solar cell devices can achieve an efficiency of over 20% for lifetimes in the tens of ns regime.

4.2 Analytical Model

4.2.1 Voltage and Current

The short circuit current I_{sc} (the current when the terminals are connected to each other or zero load resistance) and open circuit voltage V_{oc} (the voltage between the terminals when no current is drawn or infinite load resistance) are two of the most important solar cell device parameters.

A solar cell device consists of a p-n junction which is a diode. When a voltage is applied across the diode a current flows through it, which is called dark current since there is no light shining on the diode. It is expressed as:

$$I_{dark} = I_0\left(\exp(\frac{qV}{kT}) - 1\right) \tag{4.1}$$

where I_0 is the dark saturation current (the diode leakage current in the absence of light), V is the applied voltage, q is the charge on an electron, k is Boltzmann constant and T is absolute temperature.

Under photon illumination, the p-n junction device yields a light-generated current I_L, which is proportional to the light intensity. The current I_L produces a voltage drop across the resistive load that forward biases the p-n junction. The forward-bias voltage produces a dark current which flows opposite to the direction of I_L. Hence, the resulting current can be approximated as a superposition of the light-generated current and the dark current:

$$I = I_L - I_0\left(\exp(\frac{qV}{kT}) - 1\right) \tag{4.2}$$

In order to obtain the short current I_{sc}, V = 0, which means that there is no voltage and the circuit is shorted, yielding

$$I_{sc} = I_L \tag{4.3}$$

It is noted that the short current is equal to the light-generated current I_L.

To find an expression for the open circuit voltage V_{oc}, I = 0. This means that the two currents cancel out so that no current flows, which is exactly the case in an open

circuit. The resulting expression is

$$V_{oc} = \frac{kT}{q} \ln(\frac{I_{sc}}{I_0} + 1) \tag{4.4}$$

4.2.2 Efficiency and Fill Factor

The product of the current and voltage on each point of the I-V curve represents the power output at that operating condition. The maximum power occurs somewhere between V = 0 (short circuit) and V = V_{oc} (open circuit) at a voltage V_m, with the corresponding current I_m, and thus the maximum power is $P_m = I_m V_m$, which is shown in Figure 4.1. The value of V_m can be calculated by

$$\frac{d(IV)}{V} = 0 \tag{4.5}$$

Yielding,

$$V_m = V_{oc} - \frac{kT}{q} \ln(\frac{V_m}{kT/q} + 1) \tag{4.6}$$

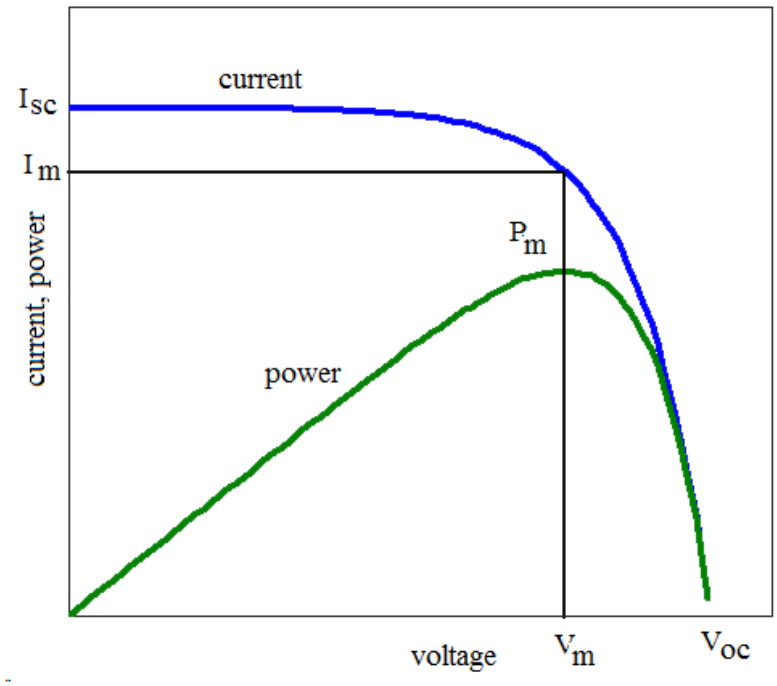

Figure 4.1. Maximum output power of a solar cell.

The conversion efficiency of a solar cell is defined as the ratio of output power to incident power. If the incoming light has a power of P_s, the efficiency for the maximum power output will be

$$\eta = \frac{I_m V_m}{P_s} \tag{4.7}$$

The fill factor (FF) is another measure of the solar cell quality, which is calculated by comparing the maximum power to the theoretical power. It is defined as

$$FF = \frac{I_m V_m}{I_{sc} V_{oc}} \tag{4.8}$$

The fill factor shows how much of the open circuit voltage and short circuit current is "utilized" at maximum power. Obviously, the nearer the fill factor is to unity, the higher the quality of the cell.

The four quantities I_{sc}, V_{oc}, η and FF are frequently used to characterize the performance of a solar cell. All of them are normally measured under standard lighting conditions, which implies Air Mass of 1.5 spectrum, light flux of 1000W/m^2 and room temperature of 300 K.

4.3 PC1D Software

4.3.1 Introduction of PC1D

The PC1D software was developed in Australia at the University South Wales of Sydney. It uses a finite-element numerical method to solve the coupled nonlinear equations for carrier generation, recombination and transport in the devices, which will eventually provide a simulation of solar cell performance [7].

By inputting the parameter values of the semiconductor materials, PC1D can calculate most of the parameters that describe solar cell output performance, such as current-voltage characteristics, short circuit current, open circuit voltage, maximum output power, and conversion efficiency.

4.3.2 Operating Interface

The software used in this research is PC1D 5.9 version. A typical operation interface is shown in Fig. 4.2. There are four parts besides the device schematic on the right side. The ‘Device’ section contains basic information about the device such as the

device area and surface reflection. The ‘Region 1’ section contains the detailed parameters of the semiconductor material that is used in the device. All these values essentially determine the output performance of the solar cell. In addition, more regions can be added so as to make a hetero-junction or multi-junction. The ‘Excitation’ section contains the illumination conditions such as the irradiation strength and working temperature. The ‘Results’ section shows the output parameters of the solar cell.

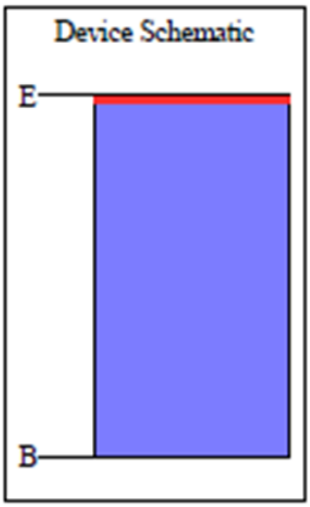

DEVICE
Device area: 100 cm^2
No surface texturing
No surface charge
Exterior Front Reflectance: 10%
No Exterior Rear Reflectance
Internal optical reflectance enabled
Front surface optically rough
Emitter contact enabled
Base contact enabled
No internal shunt elements
REGION 1
Thickness: 300 μm
Material from si.mat
Carrier mobilities from internal model
Dielectric constant: 11.9
Band gap: 1.124 eV
Intrinsic conc. at 300 K: 1×10^{10} cm^{-3}
Refractive index from si.inr
Absorption coeff. from si300.abs
Free carrier absorption enabled
P-type background doping: 1.513×10^{16} cm^{-3}
1st front diff.: N-type, 2.87×10^{20} cm^{-3} peak
No 2nd front diffusion
No rear diffusion
Bulk recombination: $\tau_n = \tau_t = 7.208$ μs
Front-surface recom.: S model, $S_n = S_t = 1\times10^{6}$ cm/s
Rear-surface recom.: S model, $S_n = S_p = 1\times10^{5}$ cm/s
EXCITATION
Excitation modified from one-sun.exc
Excitation mode: Transient, 16 timesteps
Temperature: 300 K
Base circuit: Sweep from -0.8 to 0.8 V
Collector circuit: Zero
Primary light source enabled
Constant intensity: 0.1 W cm^{-2}
Spectrum from am15g.spc
Secondary light source disabled
RESULTS
Short-circuit Ib: -3.123 amps
Max base power out: 1.535 watts
Open-circuit Vb: 0.5946 volts

Figure 4.2 Operation interface of PC1D.

4.3.3 Advantages of PC1D

The PC1D software contains library files with the optical and physical parameters

of the common semiconductor materials that are widely used in photovoltaic technology such as the GaAS, a-Si, AlGaAs, Si, InP, and Ge. High calculation speeds and intuitive user interfaces are other advantages of PC1D [8].

In the following simulation work, the four output performance quantities (η, FF, I_{sc}, and V_{oc}) for both homo-junction and hetero-junction solar cell devices are investigated. The device area is set to be 100 cm^2 and the excitation lighting condition is AM1.5 G spectrum and 0.1W/cm^2 at room temperature of 300 K.

4.4 Simulation of Homo-junction

4.4.1 Input Parameter

(a) Physical and optical parameters for WSe_2

The physical and optical properties of WSe_2 used in the PC1D were obtained through a combination of existing literature values and direct measurements performed on the thin films grown as part of this work.

The absorption spectrum, refractive index and band gap are from the direct measurements of in-house grown WSe_2 thin films [9]. Data are taken from the film fabricated at 900 ^oC. The refractive index value of 4.1 is used. The corresponding direct band gap and indirect band gap are 1.54 eV and 1.42 eV. For simulation purposes the indirect gap value of 1.42 eV is used.

The electron affinity (4.0 eV) and the dielectric constant (20.5) for WSe_2 come

from [10] and [11]. Electron and hole effective masses are very important parameters, which can determine the effective density of states (N_C, N_V) and the intrinsic carrier concentration (n_i). The Electron effective mass, $m^*_n = 0.79\ m_o$, and hole effective mass, $m^*_h = 0.58\ m_o$, are taken from [12], where m_o is the electron mass. N_C/N_V is calculated to be 1.59 and n_i is $1.67 \times 10^7\ cm^{-3}$ at 300 K by using the following equations:

$$N_C = 2\left(\frac{2\pi m_n^* kT}{h^2}\right)^{3/2} \tag{4.9}$$

$$N_V = 2\left(\frac{2\pi m_h^* kT}{h^2}\right)^{3/2} \tag{4.10}$$

$$n_i = \sqrt{N_C N_V}\ \exp\left(\frac{-E_g}{2kT}\right) \tag{4.11}$$

where k is Boltzmann constant, T is absolute temperature and E_g is the band gap.

The model for the carrier mobility as a function of doping concentration (N) is part of the software. A simplified version is shown as:

$$\mu = \mu_{low} + \frac{\mu_{high} - \mu_{low}}{1 + \left(\frac{N}{N_{ref}}\right)^{\alpha}} \tag{4.12}$$

The four quantities μ_{low}, μ_{high}, N_{ref} and α are fit parameters. Both the majority carrier mobility model and electron mobility model for p-type WSe_2 thin films were investigated in [12]. All the parameters are summarized in Table 4.1.

Table 4.1 WSe_2 parameters for PC1D simulation.

Band gap	1.42 eV
Electron affinity	4.0 eV
Dielectric constant	20.5
Refractive index	4.1
Electron effective mass	0.79 m_o
Hole effective mass	0.58 m_o
Intrinsic carrier density	$1.67x10^7$ cm^{-3}
N_C/N_V	1.59
Mobility model parameters	
$\mu_{high,p}$	32.16 cm^2/Vs
$\mu_{high,n}$	23.68 cm^2/Vs
$\mu_{low,p}$	0.127 cm^2/Vs
$\mu_{low,n}$	0.094 cm^2/Vs
N_{ref}	$1.15x10^{17}cm^{-3}$
α	10

(b) Model parameters

There are five main model parameters of the cell structure that are considered in this simulation: thickness of the P-type WSe_2 absorber, doping of the P-type WSe_2 layer,

thickness of the n-type layer, doping of the n-type layer, and minority carrier lifetime in the p-type absorber layer. The effect of these parameters on the cell output are studied one by one in order to determine a reasonable solar cell structure. Based on this analysis, two parameters are fixed (thickness of the P-type WSe_2 absorber and doping of the P-type WSe_2 layer) and the remaining three model parameters (n-type thickness, n-type doping and carrier lifetime) will be studied separately in the following sections to show how they influence the cell performance. The model parameters are determined as follows:

(1) Thickness of the P-type WSe_2 absorber

The selection of the WSe_2 thickness is based on the desire to minimize the absorber layer thickness while still collecting the incident photons. Calculations show that a 400-500 nm absorber layer achieves more than 95% absorption by using the approximate formula:

$$\frac{I}{I_o} = 1 - \exp(-\alpha d) \tag{4.13}$$

where I is the absorbed intensity, I_o is the initial light intensity, d is the thickness of the absorber layer, α is the absorption coefficient. A relatively small value of α near the edge of absorption (close to bandgap energy) was employed, where it was assumed that the absorption coefficient and incident light intensity throughout the relevant incident light energy range (about 1.4 eV-3.4 eV) are constant. Therefore, in this research, thicknesses of 400-500 nm are selected for the WSe_2 absorber layer throughout the following homo-junction and hetero-junction simulations.

(2) Doping of the P-type WSe_2 layer

The carrier concentration of the p-type layer is taken from the experimental film growth at 900 ^oC in Chapter 3. The lowest carrier concentration 7 x 10^{16} cm^{-3} from our experimental results is employed since yields the highest carrier mobility of 30 $cm^2V^{-1}s^{-1}$.

(3) Thickness of the n-type layer

The thickness of the n-type layer is the first model parameter to be optimized in section 4.4.2. The n layer thickness is swept from 0.05 μm to 0.25 μm. The minimum layer thickness, 0.05 μm, is selected based on the fact that the measured roughness of the p-type layer is 0.02 μm according to the AFM measurement in Chapter 3. Therefore the n layer must be thicker than this in order to provide complete coverage.

(4) Doping of the n-type layer

The n-type doping is another model parameter to be optimized which is swept from 3 x 10^{18} cm^{-3} to 1 x 10^{19} cm^{-3}, based on the following considerations. The main function of the n-type layer is to form the p-n junction. In addition it is necessary for the depletion region to lie almost exclusively in the p-region to obtain a high efficiency. This is an n+-p junction requiring the doping level in the n-type region to be much higher than that of the p layer. In this simulation we use the n doping level of 10^{18} cm^{-3}. The other consideration is the n region depletion width which depends on the n layer doping should be smaller than the n layer thickness. With

the doping value of 3 x 10^{18} cm^{-3}, the electric field value at the outside edge of n layer is smaller than 0.01 V/cm based on the PC1D simulation results, which can effectively assume that it is not fully depleted since the peak value of electric field is in the order of 10^5 V/cm. It is well known that a higher doping concentration results in a narrower depletion width [13], where it can be shown that the n depletion region is thinner than the n layer when the doping is greater than 3 x 10^{18} cm^{-3}. Meanwhile, the p region depletion width is also checked and it is less than the p layer. Therefore, sweeping the n-type doping from 3 x 10^{18} cm^{-3} to 1 x 10^{19} cm^{-3} is reasonable, where more details with respect to the influence of the n-type doping will be discussed in the section 4.4.3.

(5) Minority carrier lifetime in the p-type absorber layer

The minority carrier lifetime of the WSe_2 films discussed in Chapter 3 has not been quantified. A value of 0.03 μs is reported from the literature for single crystals [14]. More details with respect to the influence of carrier lifetime will be discussed in the section 4.4.4.

4.4.2 Influence of the n-Layer Thickness

First, a study of how n layer thickness influences the output performance is carried out. The parameters are set:

(1) The total thickness of device is set to be 0.5 μm based on the analysis in Section 4.4.1. The p-type layer thickness is automatically adjusted when sweeping the

n-type layer thickness.

(2) The carrier concentration of the p-type layer is set to be 7 x 10^{16} cm^{-3} based on the analysis in Section 4.4.1.

(3) A few values between 3 x 10^{18} cm^{-3} to 1 x 10^{19} cm^{-3} n-type doping are investigated, where it will be shown that the n-type doping has little effect on the solar cell performance.

(4) The carrier lifetime of the WSe_2 thin film has not been quantified. A value of 0.03 μs was reported for WSe_2 crystal from literature [14]. It is reasonable to employ this value for WSe_2 thin film in the simulation for the demonstration purpose.

(5) Sweep the n layer thickness from 0.05 μm to 0.25 μm. A carrier concentration of 3 x 10^{18} cm^{-3} is employed to demonstrate how the n-type thickness influences the output performance.

The performance simulation outputs four quantities: η, I_{sc}, V_{oc}, and the FF. Figure 4.3 shows that how the efficiency changes as a function of n-type thickness. The efficiency decreases from 21.6% to 5.1% when the thickness increases from 0.05 μm to 0.25 μm.

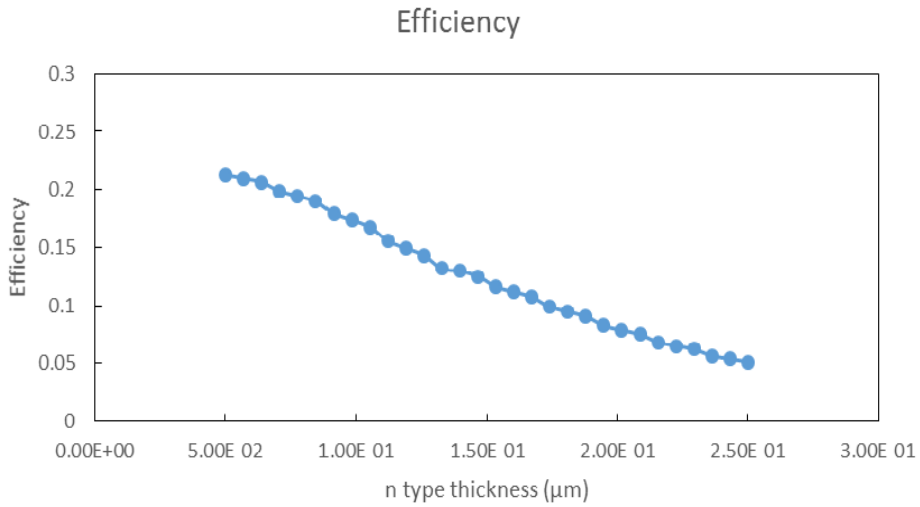

Figure 4.3 Efficiency versus n-layer thickness.

Figure 4.4 shows the dependence of I_{sc} and V_{oc} on n-type thickness. Clearly the short circuit current decreases with increasing n layer thickness. The open circuit voltage decreases slowly compared with the short circuit current because V_{oc} is dependent on the $\ln(I_{sc})$ according to equation (4.4).

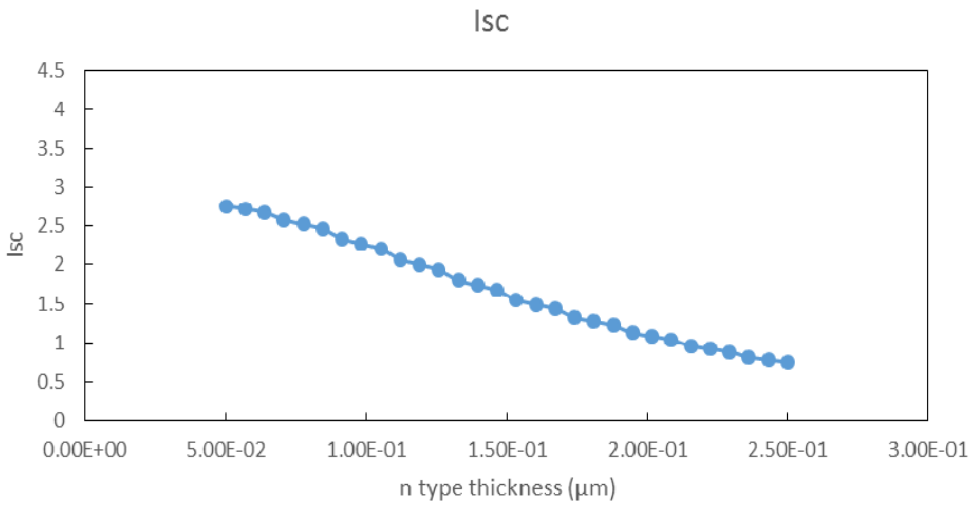

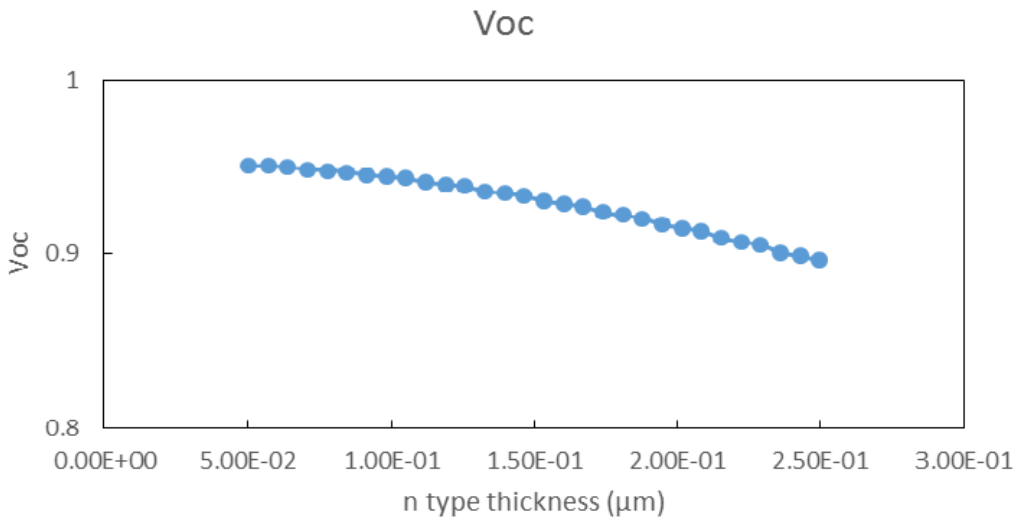

Figure 4.4 I_{sc} and V_{oc} versus n-layer thickness.

The high carrier concentration in the n-type layer results in a low carrier motility according to the Figure 3.17 in Chapter 3. When the n layer becomes thicker, the low carrier mobility in the n layer decreases the carrier collection in the device, resulting in the decrease of I_{sc}. Though the efficiency decreases quickly with the n-type layer thickness, the fill factor remains nearly constant at 0.8, as is shown in Figure 4.5. This is because the maximum output power decreases with the product of I_{sc} and V_{oc}, according to equation (4.8).

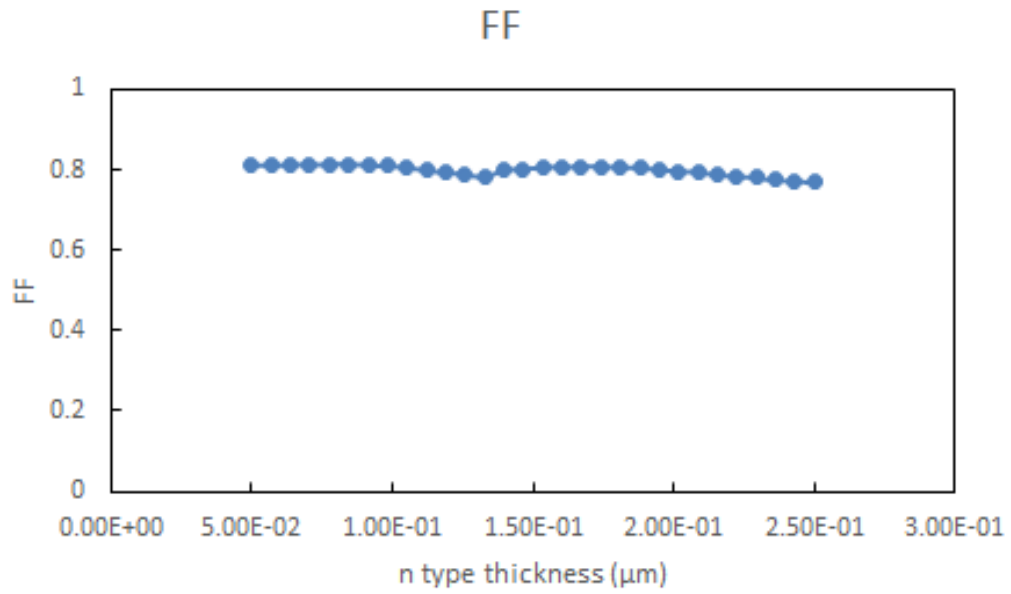

Figure 4.5 Fill factor versus n-layer thickness.

4.4.3 Influence of the n-Layer Doping

The effect of n-type layer doping on the solar cell output performance is investigated. The parameters are set as:

(1) Total thickness of device: 0.5 μm.

(2) The thickness of n-type part: 0.05 μm, based on the analysis of section 4.4.2.

(3) The carrier concentration of the p-type layer is set to be 7 x 10^{16} cm^{-3}.

(4) Carrier lifetime in each layer is set to be 0.03 μs,

(5) Sweep the carrier concentration in the n-type layer from 3 x 10^{18} cm^{-3} to 1 x 10^{19} cm^{-3}

The simulation results of efficiency as a function of n-type carrier concentration is seen in Figure 4.6. It shows that the efficiency remains almost constant at 21% regardless of the n-type doping. That is because for an n+-p junction the p layer absorbs most of the light and plays a decisive role in the cell performance. Meanwhile, it indicates that there is a range of doping values that can be utilized to design a cell with very close to optimum parameters.

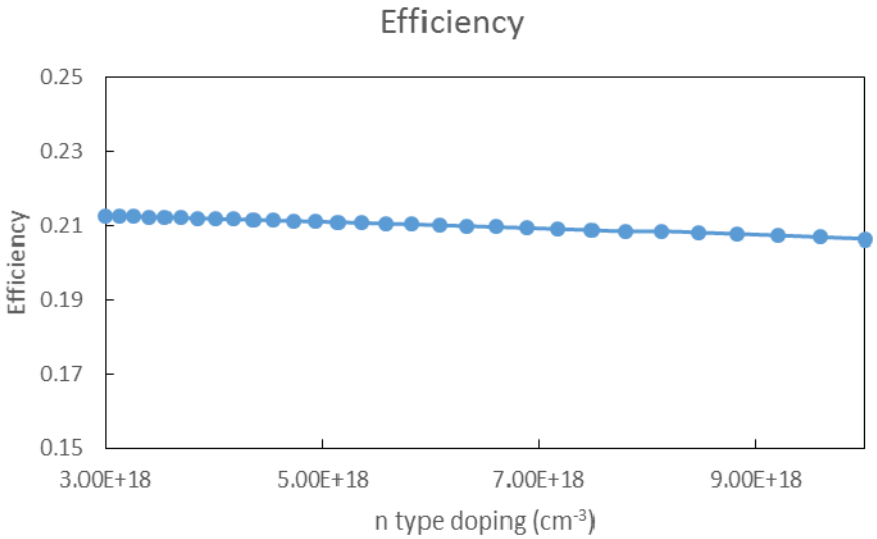

Figure 4.6 Efficiency versus n-layer doping.

Figure 4.7 shows that I_{sc} and V_{oc} remain nearly constant at 2.7 A and 0.95 V respectively. The Fill Factor, as is shown in Figure 4.8, remains around 0.8.

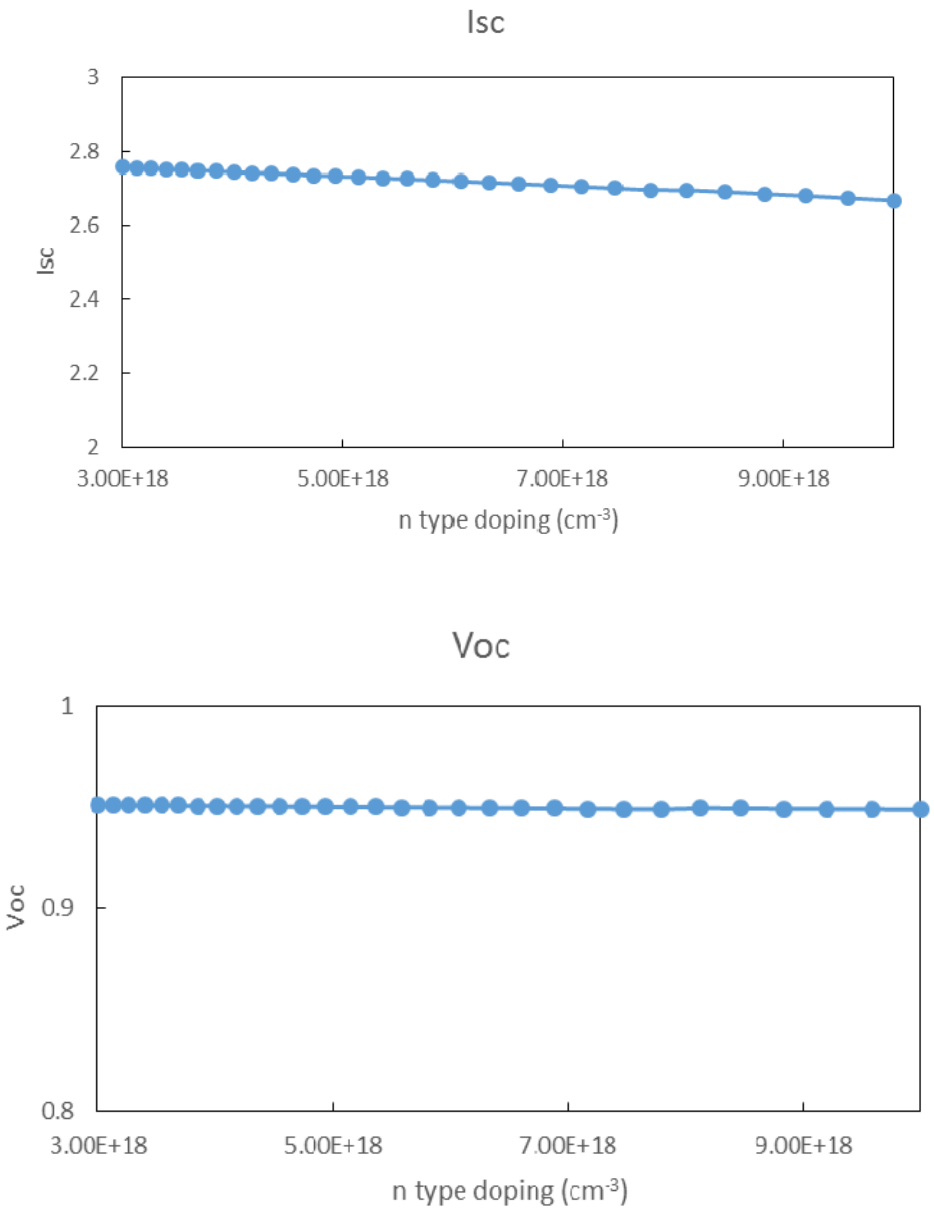

Figure 4.7 I_{sc} and V_{oc} versus n-layer doping.

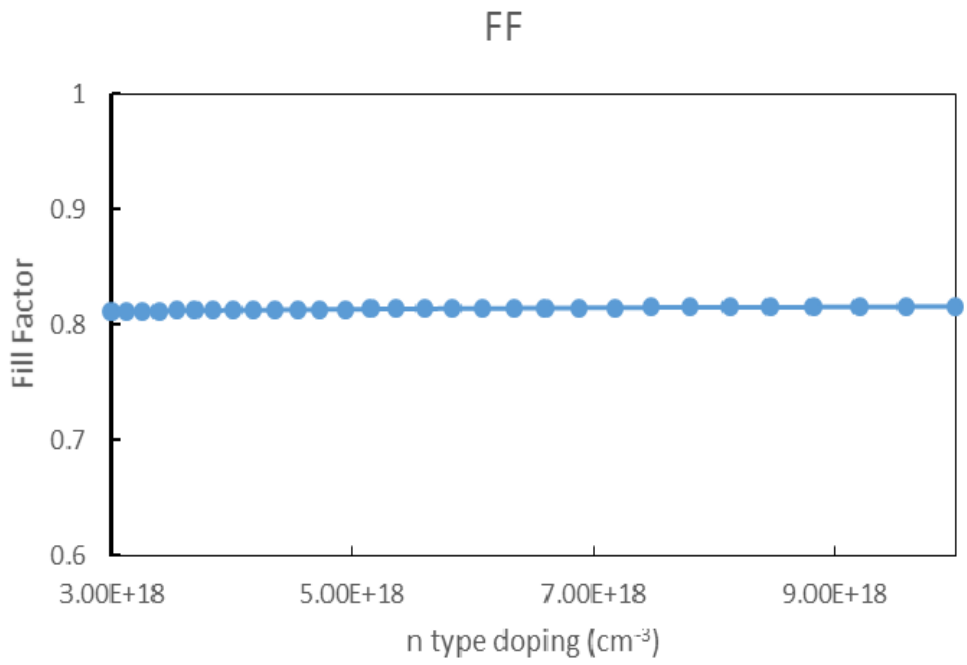

Figure 4.8 FF versus n-layer doping.

4.4.4 Influence of Minority Carrier Lifetime in the p-Layer

The effect of the minority carrier lifetime in the p-layer on the device output is investigated in this section. The parameters are set at:

(1) Total thickness of device: 0.5 μm.

(2) The thickness of the n-type layer: 0.05 μm.

(3) The carrier concentration of the p-type layer: 7 x 10^{16} cm^{-3}.

(4) Carrier concentration of 3 x 10^{18} cm^{-3} in the n-layer is used for this simulation.

(5) Sweep carrier lifetime from 10^{-4} μs to 1 μs.

The simulation results show that η, I_{sc}, V_{oc}, and FF have a similar increasing trend with the lifetime, as is shown in Figure 4.9, Figure 4.10, and Figure 4.11. It should be

noted that the quantities η, I_{sc}, V_{oc}, and FF increase rapidly with the lifetime from 10^{-4} μs to 0.02 μs, and then increase slightly after that. It should be mentioned that at the lifetime of 0.03μs (the value is from reference [14]) the efficiency reaches 21.3%, very close to the maximum value of 25.9% at 1 μs. The diffusion length is proportional to the square root of lifetime. The very high absorption coefficient of WSe_2 films make the device very thin. As a result, a relatively short diffusion length (or lifetime) can make the device to reach a high efficiency.

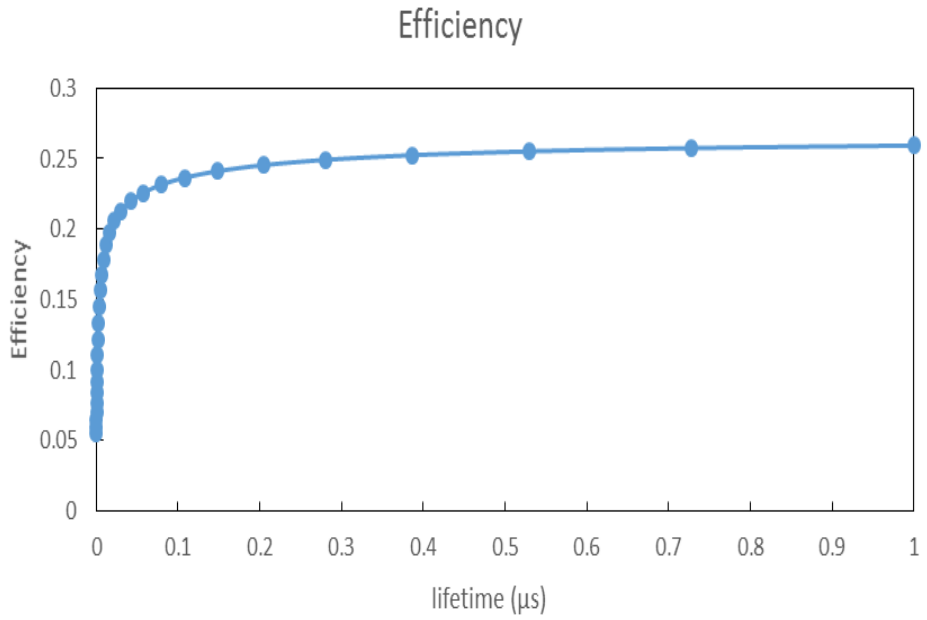

Figure 4.9 Efficiency versus carrier lifetime.

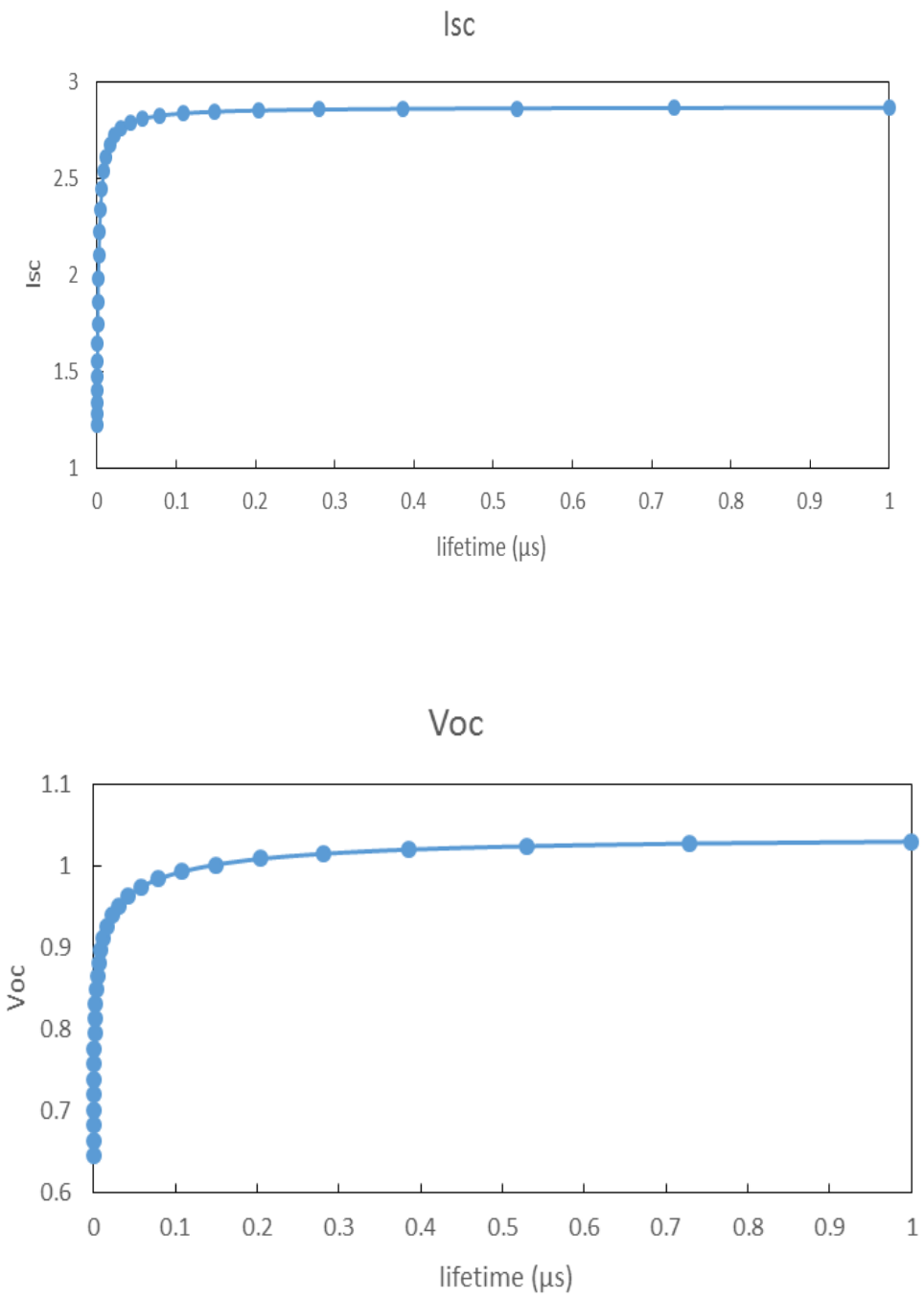

Figure 4.10 I_{sc} and V_{oc} versus carrier lifetime.

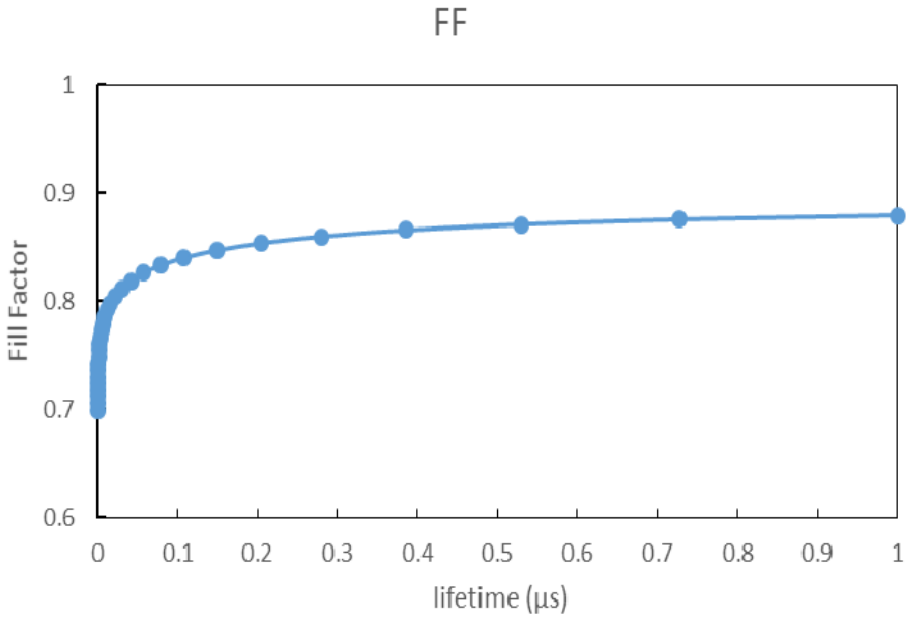

Figure 4.11 Fill factor versus carrier lifetime.

4.4.5 Summary

Multiple sets of simulations performed on WSe_2 homo-junctions indicate the promise of WSe_2 as a photovoltaic material. The efficiency of WSe_2 homo-junction can reach over 25% for high lifetime values around 1µs and over 20% efficiency is obtained for lifetimes in the tens of ns regime. Of course this device requires an n-type WSe_2 layer. It has been reported that tungsten di-selenide single crystals doped with copper are n-type in nature [15]. In addition, a chemical method was reported to intercalate copper atoms into two dimensional layered materials [16]. This method may also be employed to make n-type WSe_2 thin films since it is a two dimensional layered material. The fact that the n type WSe_2 requires complicated fabrication process makes it challenging to synthesize a

homo-junction device. However, for the homo-junction, the n layer and p layer are of the same material. Both layers have a matched lattice structure and energy band structure. As a result, unlike the hetero-junctions, there are no interface problems for the homo-junction, e.g. interface recombination, or band edge discontinuities. This makes the WSe_2 homo-junction device very attractive in PV technology.

4.5 Simulation of Hetero-junction

4.5.1 Window Materials

A hetero-junction consists of a window layer and an absorber layer. Since most window materials are able to be directly deposited by sputtering technology, a WSe_2 hetero-junction is much easier to fabricate than a homo-junction. In view of this hetero-junction device performance is also investigated.

Several window materials are considered. Typical window materials used in solar cells are transparent conductive oxide (TCO) layers such as tin oxide doped with fluorine (FTO), indium oxide doped with tin (ITO), zinc oxide doped with aluminum (AZO), and cadmium stannate Cd_2SnO_4 (CTO). In addition CdS is also used in CdS-CdTe and CdS-CIGS solar cells. However, ITO is of high cost due to the scarcity of Indium and FTO is unstable in hydrogen plasma environments [17][18]. Cadmium toxicity is an issue with respect to CTO and CdS. Therefore AZO is employed as the window material in this simulation.

4.5.2 Properties of AZO

Zinc oxide doped with aluminum is currently under intense investigation and development as a transparent conductive coating [19]. The thin films of AZO exhibit a wide band gap, are non-toxic, are as-grown n type, have a relatively low resistivity, the constituent materials are abundant, are environmentally inert, have high chemical and thermal stability, and are cost effective to manufacture [20]. Various deposition techniques have been applied to deposit AZO films, such as magnetron sputtering, pulsed laser deposition (PLD), chemical vapor deposition, atomic layer deposition (ALD), spray pyrolysis, and metal organic chemical vapor deposition (MOCVD) [21].

Recently, AZO thin films have been used as windows and contact layers for thin film solar cells with various absorber materials, such as amorphous silicon, $CuIn_{1-x}Ga_xSe_2$ (CIGS), and CdTe [22-24].

4.5.3 Input Parameters of AZO

Physical and optical properties of the AZO material used in the simulation shown in Table 4.2 are mostly from the existing literature. The band gap, 3.3 eV, and the refractive index, 1.2, for AZO thin films are taken from [25]. The AZO electron affinity of 4.5 eV is reported in [26] and the dielectric constant of 8.8 is used from [27]. The Electron effective mass, $m^*_n = 0.28\ m_o$, and hole effective mass, $m^*_h = 0.59\ m_o$, are taken from [28], where m_o is the electron mass. N_C/N_V is calculated to be 0.327 and the intrinsic carrier density is 1.27×10^{-9} cm^{-3} at 300 K by using the equations (4.9)-(4.11). An

electron mobility value of 0.4 cm^2/V with 1 x 10^{19} cm^{-3} carrier concentration is reported in [29]. The lifetime value of 3.8 ns is taken from [30]. The absorption spectra is from the direct measurement of our in-house grown AZO films.

Table 4.2 AZO parameters for PC1D simulation.

Band gap	3.3 eV
Electron affinity	4.5 eV
Dielectric constant	8.8
Refractive index	1.2
Electron effective mass	0.28 m_o
Hole effective mass	0.59 m_o
Intrinsic carrier density	1.27 x 10^{-9} cm^{-3}
N_C/N_V	0.327
Carrier lifetime	3.8 ns
Carrier mobility	0.4 cm^2/Vs
Carrier concentration	1 x 10^{19} cm^{-3}

4.5.4 Simulation results of AZO-WSe_2

The simulation results for the hetero-junction device are similar to the homo-junction device. Therefore, I_{sc}, V_{oc}, η and the FF as a function of the various input

parameters for the hetero-junction device are not presented. Instead a characteristic current-voltage curve is used to present the basic performance of the hetero-junction solar cell. The parameters of the hetero-junction are set at:

(1) Total device thickness: 0.5 μm.

(2) The thickness of WSe_2: 0.45 μm.

(3) The thickness of AZO: 0.05 μm.

(4) Carrier lifetime of p type WSe_2: 0.03 μs.

(5) Carrier concentration of p type WSe_2: 7×10^{16} cm^{-3}.

(1) Equilibrium band structure

The behavior of the hetero-junction depends crucially on the alignment of the energy bands at the interface of the two semiconductor materials. In the hetero-junction band structure, the layer on the right side is the p-type WSe_2 absorber layer, and the n-type AZO layer is on left side. The equilibrium band structure is shown in Figure 4.12. The electron affinity of AZO is 4.5 eV, which is larger than WSe_2 of 4 eV. Hence, it forms a Type II hetero-junction [31].

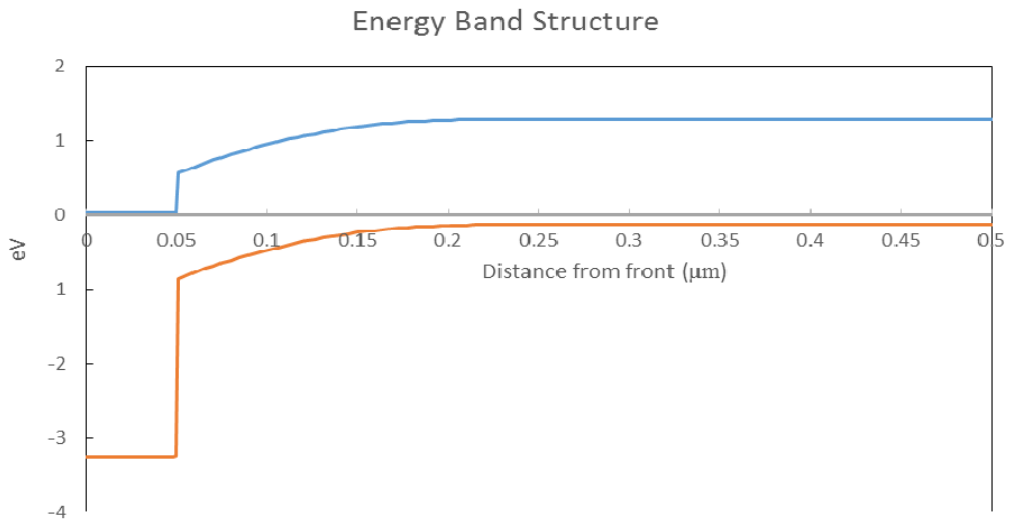

Figure 4.12 Equilibrium band structure of AZO-WSe_2.

(2) The output performance and I-V curve are shown in Figure 4.13

Short circuit current I_{sc} = 2.87 amps

Open circuit voltage V_{oc} = 0.982 volts

Maximum conversion efficiency η = 23.7%

Fill factor FF = 0.843

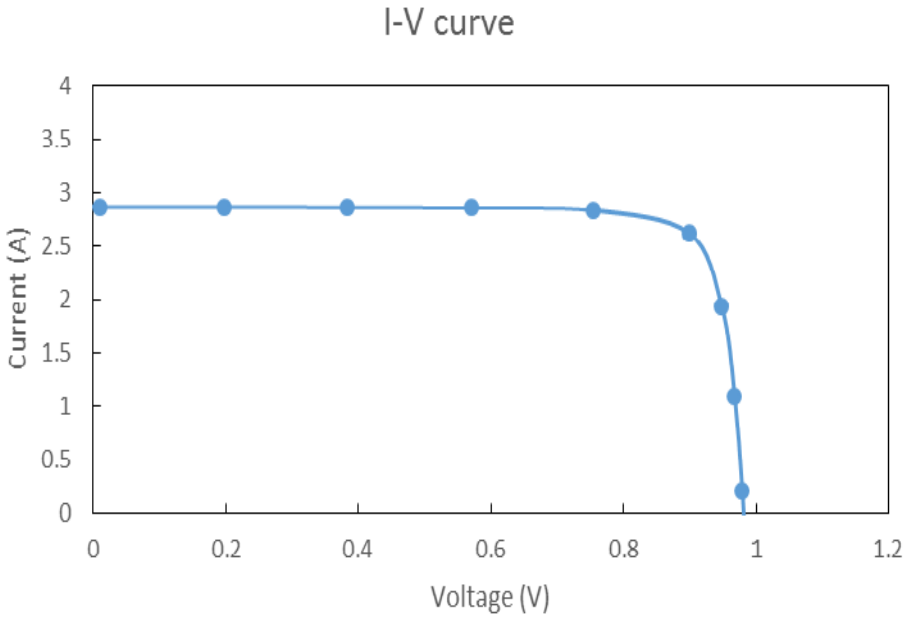

Figure 4.13. I-V characteristic of the hetero-junction cell.

(3) Efficiency versus minority carrier lifetime in p type WSe_2

The carrier lifetime of p type WSe_2 is a very important parameter. The efficiency versus minority carrier lifetime of WSe_2 is presented in Figure 4.14. It shows a similar trend to homo-junction. At low carrier lifetime 10^{-4} μs, the efficiency is as low as 12.8%. However, the efficiency rapidly increases to 23.7% at 0.03 μs, and then grows slowly after that, achieving 26.9% at 1 μs.

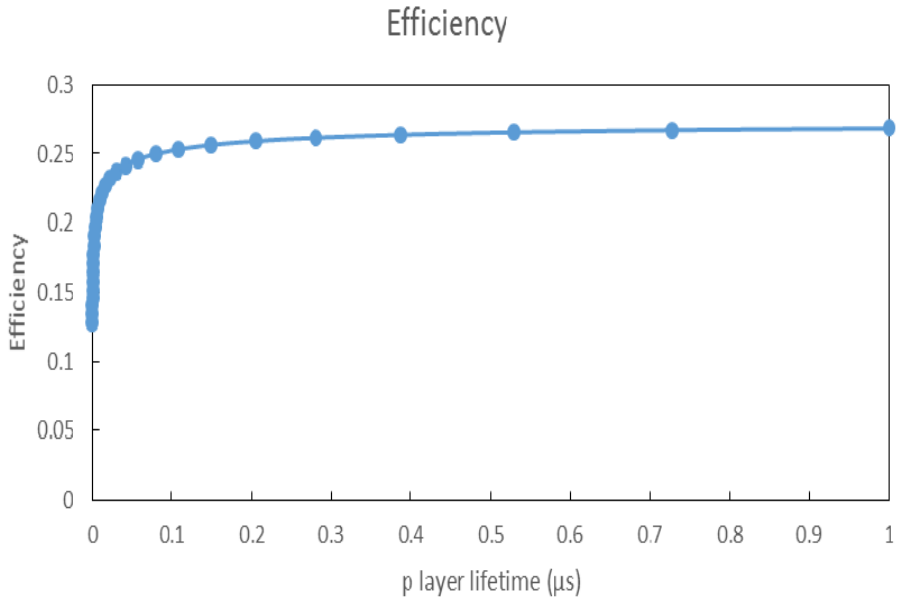

Figure 4.14 Efficiency versus minority carrier lifetime of p type WSe_2.

4.5.5 Summary

AZO-WSe_2 forms a Type II hetero-junction. Based on the simulation results for an AZO-WSe_2 hetero-junction, this solar cell device can achieve an efficiency of 23.7%. Compared with the WSe_2 homo-junction, AZO can be RF sputter deposited, allowing preliminary hetero-junction devices to be rapidly achieved. Moreover, AZO is of relatively high conductivity. As a result, light-generated electrons can easily flow laterally in the window layer to reach an electrical contact. In addition, the wide band gap of AZO allows most of the light absorption to occur in the WSe_2 absorber layer, maximizing the efficiency.

4.6 Discussion and Conclusion

Multiple sets of simulations for WSe_2 homo-junction and hetero-junction devices were performed using PC1D software. It appears that WSe_2 has a high potential for photovoltaic applications. The very high absorption coefficient of WSe_2 thin films results in simulations reaching near saturation in efficiency at around only 400-500 nm of absorber layer thickness, indicating a good economic prospect for large-scale production. According to the simulation results, both homo-junction and hetero-junction devices can achieve an efficiency of over 25%, corresponding to 1 μs carrier lifetime in the p type WSe_2 layer. Values at or smaller than 1 ns would lead to poor performance. However, values at or over several tens of ns would indicate a promising performance. For example, if we use a carrier lifetime of 30 ns taken from a WSe_2 single crystal [14], both homo-junction and hetero-junction devices yield an efficiency over 20%.

In summary, based on the simulation analysis, WSe_2 homo-junctions as well as hetero-junction devices with an AZO window layer yield high efficiency values, over 20% at several tens of ns carrier lifetime and over 25% around 1 μs lifetime in the absorber layer. The simulation results indicate that the semiconductor material WSe_2 is a very promising thin film solar cell candidate. In addition to the attractive high efficiency, the device materials are of low cost and non-toxicity.

Reference

[1] Jiang C., Li T. Z., Zhang X., Hou L., Simulation of silicon solar cell using PC1D, Advanced Materials Research, 2011 (383-390) 7032-1036.

[2] Gran, J., Kübarsepp, T., Sildoja, M., Manoocheri, F., Ikonen, E., Müller, I. Simulations of a predictable quantum efficient detector with PC1D, Metrologia, 2012 (49) S130-S134.

[3] Sepeai, S., Zaidi, S. H., Desa, M. K. M., Sulaiman, M. Y., Ludin, N. A., Adib Ibrahim, M., Sopian, K. Design optimization of bificial solar cell by PC1D simulation, Journal of Eneryg Technologies and Policy, 2013 (3) 1-11.

[4] P.A. Basore, Numerical modeling of textured silicon solar cells using PC1D, IEEE Trans. on Electron Devices, 1990 (37) 337-343.

[5] H. Haug, A.Kimmerle, J.Greulich, A.Wolf, E.StensrudMarstein, Im- plementation of Fermi–Dirac statistics and advanced models inPC1D for precise simulations of silicon solar cells, Sol. Energy Mater. Sol. Cells, 2014 (131) 30-36.

[6] Kai Wang and Ivan Perez-Wurfl, A method to overcome the time step limitation of PC1D in transient excitation mode, Energy Procedia, 2014 (55) 155-160.

[7] D. A. Clugston and P. A. Basore, PC1D version 5: 32-bit solar cell modeling on personal computers Conference Record of the 26th IEEE Photovoltaic Specialists Conference, 1997, 207-210.

[8] Halvard Haug, Birger R. Olaisen, Ørnulf Nordseth, Erik S. Marstein, A graphical user interface for multivariable analysis of silicon solar cells using scripted PC1D simulations, Energy Procedia, 2013 (38) 72-79.

[9] Qinglei Ma, Hrachya Kyureghian, Joel D. Banninga and N. J. Ianno, ‘Thin Film

WSe2 for Use as a Photovoltaic Absorber Material', MRS Proceedings, 2014, 1670.

[10] O. Lang, Y. Tomm, R. Schlaf, C. Pettenkofer, W. Jaegermann, Single crystalline GaSe/WSe2 heterointerfaces grown by van der waals epitaxy. II. junction characterization, Journal of Applied Physics, 1994 (75) 7814–7820.

[11] B. Davey, B. L. Evans, The optical properties of MoTe2 and WSe2, Physica Status Solidi A, 1972 (13) 483–491.

[12] Hrachya Kyureghian, Qinglei Ma, Natale Ianno, "Numerical Modeling of WSe2 Solar Cells", submitted to Solar Energy Materials and Solar Cells.

[13] Robert Pierret, Semiconductor device fundamentals, 2nd edition, Addison Wesley, 1996, pp 200-230.

[14] A. Jakubowicz, D. Mahalu, M. Wolf, A. Wold, R. Tenne, WSe2:Optical and electrical properties as related to surface passivation of recombination centers, Physical Review B, 1989 (40) 2992-3000.

[15] M.P. Deshpande, M.N. Parmar, Nilesh N. Pandya, Sunil Chaki, Sandip V. Bhatt, Studies on transport properties of copper doped tungsten diselenide single crystals, Physica B: Physics of Condensed Matter, 2012 (407) 808-812.

[16] Janina P. Motter, Kristie J. Koski, and Yi Cui, General Strategy for Zero-Valent Intercalation into Two-Dimensional Layered Nanomaterials, Chem. Mater., 2014 (26) 2313–2317.

[17] Chaoying Liu, Zhiwei Xu, Yanfang Zhang, Jing Fu, Shuguang Zang, Yan Zuo, Effect of annealing temperature on properties of ZnO:Al thin films prepared by pulsed DC reactive magnetron sputtering, Materials Letters, 2015 (139) 279–283.

[18] Hong-lie SHEN, Hui ZHANG, Lin-feng LU, Feng JIANG, Chao YANG, Preparation

and properties of AZO thin films on different substrates, Progress in Natural Science: Materials International, 2010 (20) 44−48.

[19] T. Minami, S. Suzuki, and T. Miyata, Transparent conducting impurity-co-doped ZnO:Al thin films prepared by magnetron sputtering, Thin Solid Films, 2001 (53) 398–399.

[20] Jaehyeong Lee, Dongjin Lee , Donggun Lim, Keajoon Yang, Structural, electrical and optical properties of ZnO:Al films deposited on flexible organic substrates for solar cell applications, Thin Solid Films, 2007 (515) 6094–6098.

[21] Qiong Nian, Martin Y. Zhang, Bradley D. Schwartz, and Gary J. Cheng, Ultraviolet laser crystallized ZnO:Al films on sapphire with high Hall mobility for simultaneous enhancement of conductivity and transparency, Applied Physics Letters, 2014 (104) 201907.

[22] Shuoshuo Xu, Zongcun Liang, Hui Shen, The preparation of AZO/a-Si/c-Si heterojunction structure on p-type silicon substrate for solar cell application, Materials Letters, 2014 (137) 428–431.

[23] Yu Sup Jung, Hyung Wook Choi and Kyung Hwan Kim, Properties of AZO Thin Films for Solar Cells Deposited on Polycarbonate Substrates, Journal of the Korean Physical Society, 2009 (55) 1945–1949.

[24] J. Perrenoud, L. Kranz, S. Buecheler, F. Pianezzi, A.N. Tiwari, The use of aluminium doped ZnO as transparent conductive oxide for CdS/CdTe solar cells, Thin Solid Films, 2011 (519) 7444-7448.

[25] Min Su Kim, Kwang Gug Yim, Jeong-Sik Son, and Jae-Young Leem, Effects of Al concentration on structural and optical properties of Al-doped ZnO thin films, Chem.

Soc. 2012 (33) 1235-1241.

[26] Seung Jae Baik and Koeng Su Lim, High-efficiency Pin-type Amorphous Si Solar Cells Fabricated with a Low-electron-affinity Buffer Layer on the Front Electrode, Journal of the Korean Physical Society, 2011 (59) 443-447.

[27] W.H. Kim, W. J. Maen, M.K. Kim, H. Kima, Low pressure chemical vapor deposition of aluminum-doped zinc oxide for transparent conducting electrodes, Journal of The Electro- chemical Society, 2011 (158) D495–D499.

[28] O. Madelung, Semiconductors: Data Handbook, 3rd Edition, Springer, 2014.

[29] Abdalla A. Alnajjar, ZnO:Al grown by sputtering from two different target sources: A comparison study, Advances in Condensed Matter Physics, 2012 (2012) 1-8.

[30] Yongchun Zhong, Aleksandra B. Djurisic, Yuk Fan Hsu, Kam Sing Wong, Gerhard Brauer, Chi Chung Ling, and Wai Kin Chan, Exceptionally long exciton photoluminescence lifetime in ZnO tetrapods, J. Phys. Chem. C, 2008 (112) 16286–16295.

[31] Mark Lundstrom, Heterostructure fundamentals, 1997, T3-7.

Chapter 5 Conclusion and Future Work

In this work, the growth and characterization of WSe_2 film has been studied. By using soft selenization approach in a single-zone furnace, highly c-axis orientated P-type WSe_2 films have been grown. The WSe_2 thin films were characterized by Raman spectroscopy, x-ray diffraction, scanning electron microscopy, atomic force microscopy, near UV-VIS spectrophotometry, spectroscopic ellipsometry and hall effect measurement. Raman spectroscopy is a good indicator for film quality. It shows that WSe_2 films of higher quality present more pronounced doublet Raman peaks. By optimizing the film growth conditions, an optimal processing temperature is found where high quality WSe_2 thin films are achieved with a large mobility value. The scanning electron microscopy clearly shows that the direction of grains is parallel to the substrate at that temperature. The characterization results, such as band gap and absorption coefficient, show that WSe_2 has a good potential for photovoltaic applications.

Then with the aid of PC1D software, multiple sets of simulations for WSe_2 homo-junction and hetero-junction devices were performed. The very high absorption coefficient of WSe_2 thin films results in a thin absorber layer (about 0.5 μm) reaching near saturation in efficiency, indicating a good economic prospect for large-scale production. Based on our simulation results, both WSe_2 homo-junction devices and hetero-junction devices with AZO window layer present high efficiency values, over 20% at several tens of ns carrier lifetime of absorber layer. The simulation results indicate that

WSe_2 is a very promising thin film solar cell candidate.

Although the results obtained in the simulations are good, it should be pointed out that the carrier lifetime of the p type WSe_2 layer has not been quantified. Lifetime of several tens of ns results in very promising efficiency and values at or less than 1 ns result in poor performance. Therefore, measurement of the carrier lifetime is of most importance. In addition, a homo-junction device requires an n-type WSe_2 layer. However, there is no high quality n type WSe_2 thin films reported in the literature. Several methods, such as copper doping and copper intercalation, may be able to make n type WSe_2 thin films. Future study should be performed on the preparation of high quality n type WSe_2 thin films. For hetero-junction devices, the relatively simpler fabrication process make it very attractive. However, due to the unmatched lattice structure and energy band structures for n layer and p layer, the interface problem may become a significant issue for hetero-junction devices. Clearly, further research should be carried out with respect to the interface problems, such as interface recombination and band edge discontinuities.

Appendix: Experimental Technology

A.1 Sputtering Deposition

Sputtering deposition is based on the theory of momentum exchange due to collisions between the ions and atoms in the target materials. In this technique, ions are accelerated to the negatively charged target and bombard the target surface [1]. These ions derived from a plasma. Ions with an energy greater than the surface binding energy of the target dislodge target atoms and other ions, as is shown in Fig A.1. Part of ejected atoms attach themselves to the substrate, and a thin film of the target material is produced. Sputtering sources often employ magnetrons that utilize strong electric and magnetic fields to confine charged plasma particles close to the surface of the target in order to generate more ionizing collisions near the target surface and lead to a higher deposition rate.

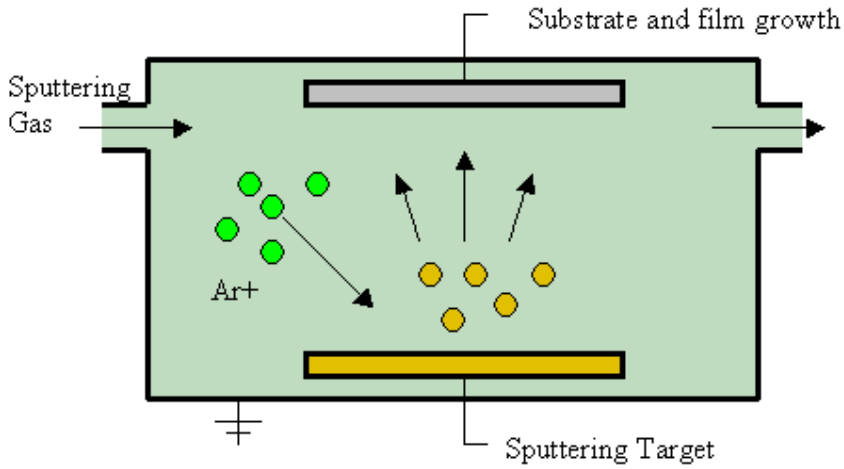

Figure A.1 Sputtering principle.

Sputtering can be categorized into direct current (DC) and the radio frequency (RF) sputtering based on the type of power source. The DC sputtering utilizes a constant voltage to accelerate the ions to the desired bombarding velocity. It is normally adopted when the target materials are conductors because charges can move freely about the conductors to prevent any charge buildup. However, if the material is an insulator, charges will remain localized and accumulate on the target surface, preventing further ion bombardment. RF sputtering utilizes an alternating voltage at radio frequency (typically about 13.5 MHz) to prevent the buildup of charges on the insulator targets.

A.2 Raman Spectroscopy

Raman spectroscopy utilizes the inelastic scattering of photons, usually from a monochromatic laser source, to determine the energy of vibrational or rotational modes in a material. It can be very useful in semiconducting applications for identifying the presence of different crystallographic phases.

When photons are scattered from an atom or molecule, most photons are elastically scattered (also called Rayleigh scattering), such that the scattered photons have the same energy as the incident photons [2]. A small fraction of the scattered photons are from the inelastic scattering. Inelastic scattering means that the energy of photons in monochromatic light changes upon interaction with a sample. When shining a monochromatic light source on a sample, photons of the light are absorbed by the sample and then reemitted. The incident photons interact with molecular vibrations, phonons or

other excitations in the sample, resulting in the energy of the reemitted photons being shifted up or down in comparison with original incoming photon energy. This energy shift, which is called Raman shift, provides information about vibrational, rotational and other low frequency transitions in molecules. Raman shifts are typically reported in wavenumbers, expressed as:

$$\Delta\omega = \frac{1}{\lambda_0} - \frac{1}{\lambda_1} \tag{6.1}$$

where $\Delta\omega$ is the Raman shift expressed in wavenumber, λ_0 is the excitation wavelength, and λ_1 is the Raman spectrum wavelength.

The Raman interaction leads to two possible outcomes. If the photon lost energy after exciting a vibrational mode, then the material absorbs energy and the scattered photon has a lower energy than the incident photon. This is called Stokes scattering. If the vibrational mode contributes to the scattered photon, leading to a higher energy of scattering photon compared with the incoming light, it is referred to as Anti-Stokes scattering. The difference in energy between the incoming and scattered light is called the Raman shift, and it corresponds to the energy difference between two resonant states of the material and is independent of the absolute energy of the photon. Figure A.2 shows the difference of three light scattering types: Rayleigh scattering, Stokes scattering and Anti-Stokes scattering.

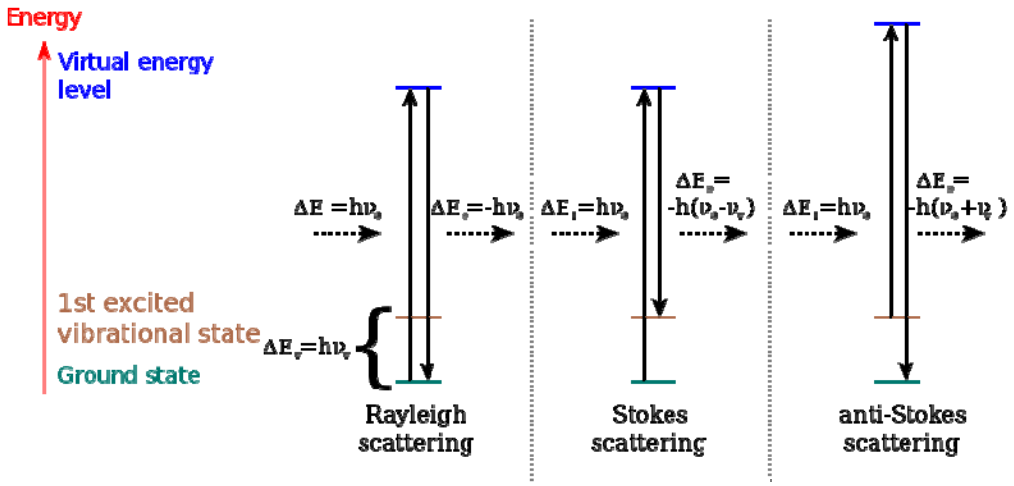

Figure A.2 Three types of light scattering: Rayleigh scattering, Stokes scattering and Anti-Stokes scattering.

A.3 Spectroscopic Ellipsometry

Spectroscopic ellipsometry is an optical measurement technique that characterizes light reflection or transmission from samples. Its key feature is to measure the change in polarized light upon light reflection off a sample. The name "ellipsometry" stems from the fact that polarized light often becomes ‘elliptical’ upon reflection. The term "spectroscopic" relates to the fact that the information gained is a function of the light wavelength (spectra).

Ellipsometry is an indirect method, and does not directly measure the optical information of films. Instead, it measures two values: the amplitude ratio Psi and the phase difference Delta between light waves known as p- and s-polarized light waves. In spectroscopic ellipsometry, spectra are measured by changing the light wavelength from the ultraviolet to the visible region [3].

A model analysis based on the measured data must be performed. By the construction of an optical model, the measured Psi and Delta can be converted into optical information of the sample. Upon the analysis of the change of polarization of light, ellipsometry can yield a wealth of information about a thin film, such as thickness, roughness, index of refraction, and extinction coefficient, as is shown in Figure A.3.

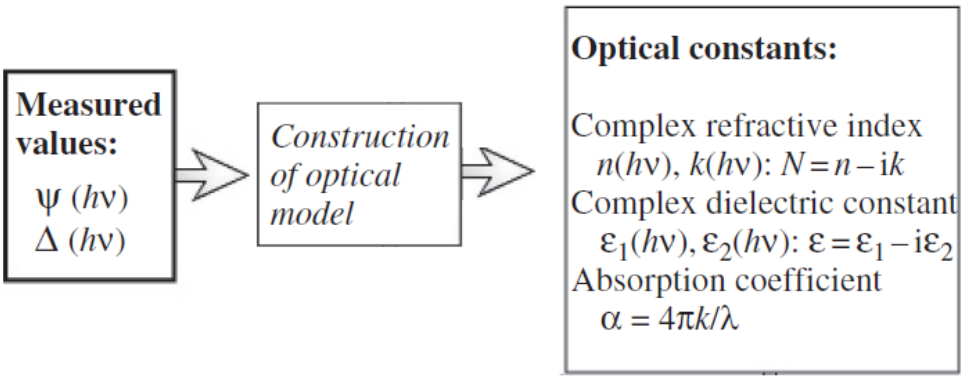

Figure A.3 Characerizations from spectroscopic ellipsometry.

A.4 X-ray Diffraction

X-ray diffraction is a powerful non-destructive tool primarily used for identifying the phase composition and structural properties of thin films and single crystals by analyzing the interference patterns of scattered x-rays. This analytical technique is based on the Bragg Law, shown in Figure A.4:

$$n\lambda = 2d\sin(\theta) \tag{6.2}$$

where n is a positive integer, λ is the wavelength of incident wave, θ is the incident angle, d is atomic lattice plane spacing.

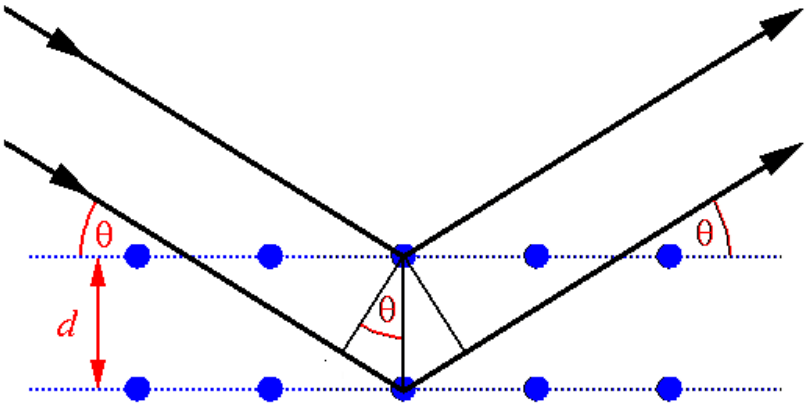

Figure A.4 The schematic of Bragg scattering.

X-rays with wavelengths at the same order of magnitude as the spacing d between planes in the crystal can elastically interact with the lattice, which is normally called Thompson scattering. When the Bragg law is satisfied, X-rays scattered from parallel lattice planes can constructively interfere, resulting in Bragg peaks [4]. By analyzing the peak positions and shapes, information of the thin film or single crystal can be achieved, such as lattice structure, orientation, and small crystallite region size.

A.5 Transmission Spectra

A Perkin Elmer lambda 900 spectrometer was used to measure the transmission and reflectivity of samples. This data was used to determine the absorption coefficient and the bandgap via the Tauc plot.

When a beam of light is incident on the film, part of the light is reflected on the front surface, part is absorbed by the material and the rest goes out of the film, as is

shown in Figure A.5.

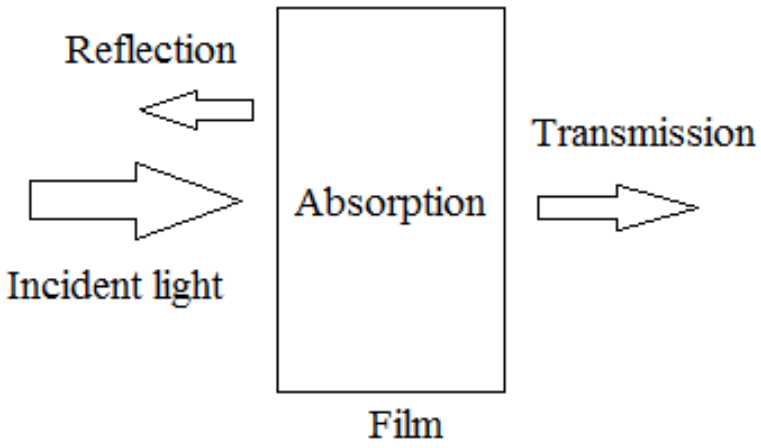

Figure A.5 The schematic of light going through a film.

The absorption coefficient of the film is calculated by using equation:

$$\alpha = \frac{1}{t}\ln((1-R)/T) \tag{6.3}$$

where α is the absorption coefficient, R is reflectivity, T is the transmission and t is the thickness of film. The optical band gap energy and the absorption coefficient has a relation expressed as [5]:

$$(\alpha h\nu)^i = c(h\nu - E_g) \tag{6.4}$$

where hv is the photon energy, c is a constant, E_g is direct band gap or indirect band gap, i is a number equivalent to 2 for direct band gap and 1/2 for indirect band gap. Both direct and indirect band gap energy can be determined by plotting $(\alpha hv)^i$ as a function of photon energy (hv).

A.6 Hall Effect Test

The van der pauw technique can be used to determine the resistivity of a uniform and pinhole free thin film, provided its thickness is known. This is achieved by the measurement of resistances along predetermined configuration (Fig. A.6). Silver paint is used to make contacts onto the samples in order to make measurements.

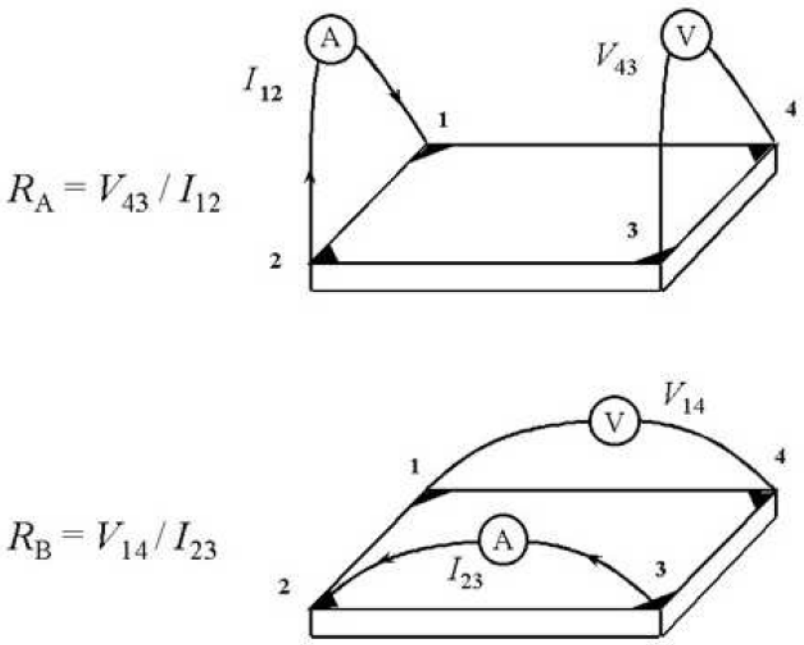

Figure A.6 Resistivity measurement configuration (NIST, 2010).

The carrier type and sheet carrier density can be determined by the Hall measurement in the van der pauw technique. The sheet carrier density is given by

$$n_s = \frac{IB}{qV_H} \tag{6.5}$$

where I is the current forced through diagonally opposite pair of contacts, V_H is the voltage measured across remaining diagonally opposite contacts, B is the magnetic field perpendicular to sample, q is the charge of an electron.

The carrier mobility μ can be determined from the carrier density n_s and sheet resistance R_s by the equation:

$$\mu = 1/(q\ n_s\ R_s) \tag{6.6}$$

A schematic for making a Hall-effect measurement using the Van der Pauw technique is shown in Fig A.7 [6]. Current is sent through the diagonally opposite contacts 1 and 3 whilst the Hall voltage is measured across diagonally opposite contacts 2 and 4. The magnetic field is normal to the plane in which measurement is being made.

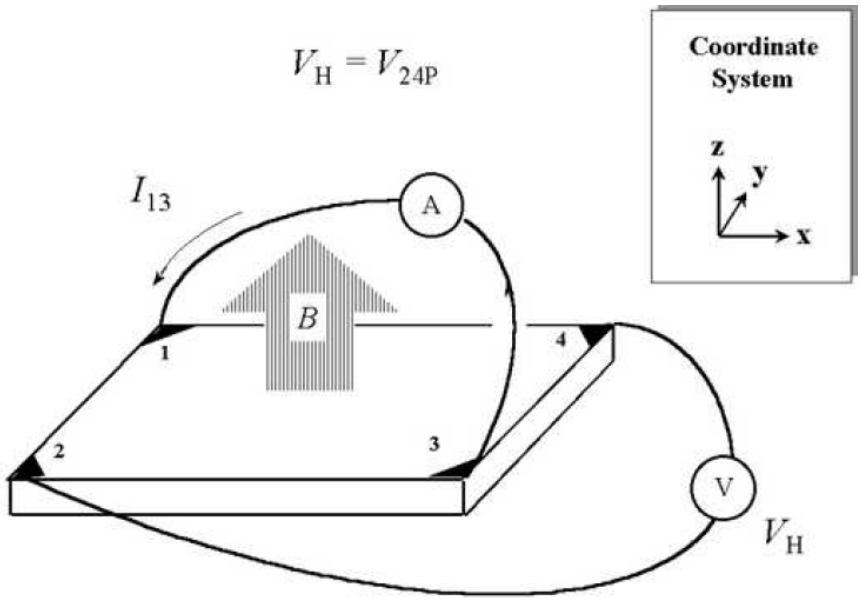

Figure A.7 Hall-effect measurement schematic (NIST, 2010).

A.7 Scanning Electron Microscope

The scanning electron microscope (SEM) is an instrument that produces a largely magnified image by using electrons to form an image. It utilizes a focused high-energy electron beam to hit the samples in a vacuum condition and generate a variety of signals at the surface of samples. The signals that derive from electron-sample interactions provide information about the sample including external morphology, chemical composition, and crystalline structure and orientation [7].

A scanning electron microscope normally consists of electron gun, electron lenses, sample stage, detectors and display. A typical structure is shown in Figure A.8 [8]. An electron gun at the top of the microscope is to produce electron beams. The electron beam follows a vertical path through the microscope, travels through electromagnetic fields and lenses, and finally focuses the beam down toward the sample. Once the beam hits the sample, signals such as secondary electrons and back scattered electrons are ejected from the sample and collected by detectors. Normally, secondary electrons are used to generate the morphology images of the sample surface and back scattered electrons is used to detect the chemical composition.

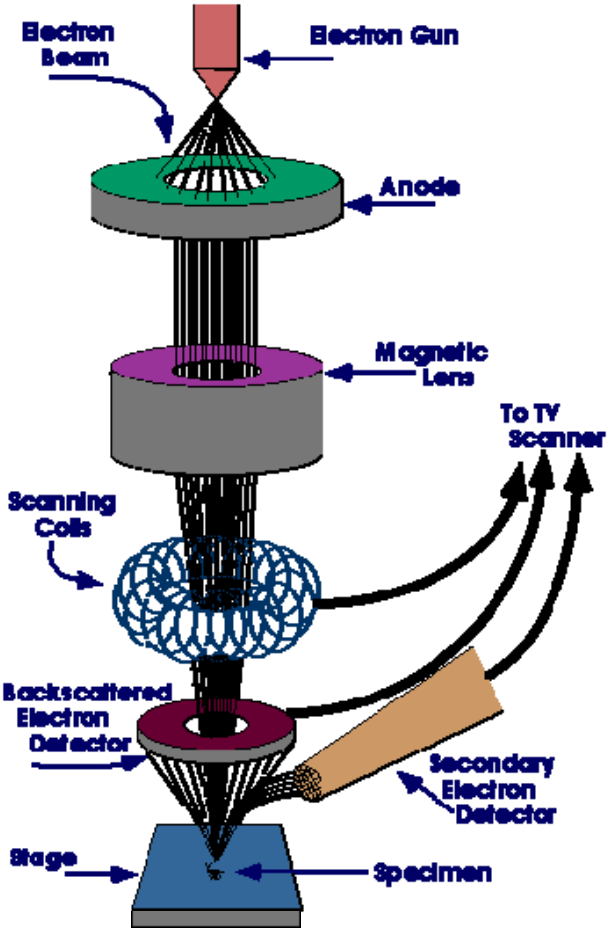

Figure A.8 Schematic of a SEM structure.

A.8 Atomic Force Microscopy

The Atomic Force Microscopy (AFM) is a very high resolution type of scanning probe microscopy, providing a 3D profile of the sample surface with a resolution on the order of nanometer by measuring forces between a sharp probe and sample surface at a very short distance (Figure A.9) [9].

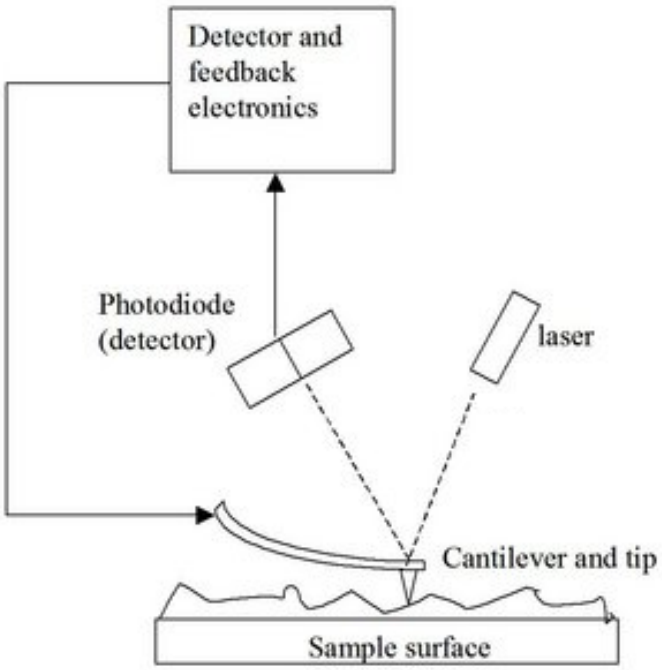

Figure A.9 Block diagram of AFM.

During the AFM imaging process, the sample surface is scanned by a nanometer radius tip mounted on the end of a flexible cantilever. The cantilever performs like a spring. Therefore, the amount of force is dependent on the spring constant of the cantilever and the distance between the probe and the sample surface, which is described by Hooke's Law:

$$F=-k\cdot x \tag{6.7}$$

F is force, k is spring constant, and x is cantilever deflection.

When the AFM probe gently touches the sample surface, the cantilever bends and reflects the laser beam into the photodiode detector. The small forces between the probe

and the surface are monitored and finally form the image of the surface.

The AFM can be simply categorized into three modes based on the mature of the probe motion: contact mode, non-contact mode, and tapping mode. In this work, a Bruker Dimension Icon AFM was used at Peak Force tapping mode.

A.9 Profilometry

An Ambios Technology XP2 surface profilometer was used to determine the thickness of thin films. During the process of sputtering film, a mask made by Al foil is used to cover part of the substrate. Hence, there will be step between the film region and clean quartz region when sputtering is done. The profilometer measures the step height which is then equal to the film thickness. The sputtering rate is the thickness divided by the sputtering time.

Reference

[1] Angus Rockett, The materials science of semiconductors, 1st edition; Springer, US, 2007, pp 505-572.

[2] Ewen Smith and Geoffrey Dent, Modern Raman spectroscopy – a practical approach, John Wiley & Sons Ltd, England, 2005, pp 91-93.

[3] Hiroyuki Fujiwara, Spectroscopic ellipsometry principles and applications, John Wiley & Sons Ltd, Japan, 2007, pp 1-48.

[4] M. Ali Omar, Elementary solid state physics: principles and applications, 4th edition, Addison-Wesley, 1994, pp 34-53.

[5] Shimadzu, Measurements of band gap in compound semiconductors, No. A428.

[6] W. Robert Thurber, Hall effect measurements, The National Institute of Standards and Technology (NIST): http://www.nist.gov/pml/div683/hall.cfm

[7] Ludwig Reimer, Scanning electron microscopy: physics of image formation and microanalysis, Springer; 1998, pp 1-56

[8] https://www.purdue.edu/ehps/rem/rs/sem.htm

[9] Robert A. Wilson and Heather A. Bullen , Basic theory atomic force microscopy: http://asdlib.org/onlineArticles/ecourseware/Bullen/SPMModule_BasicTheoryAFM.pdf